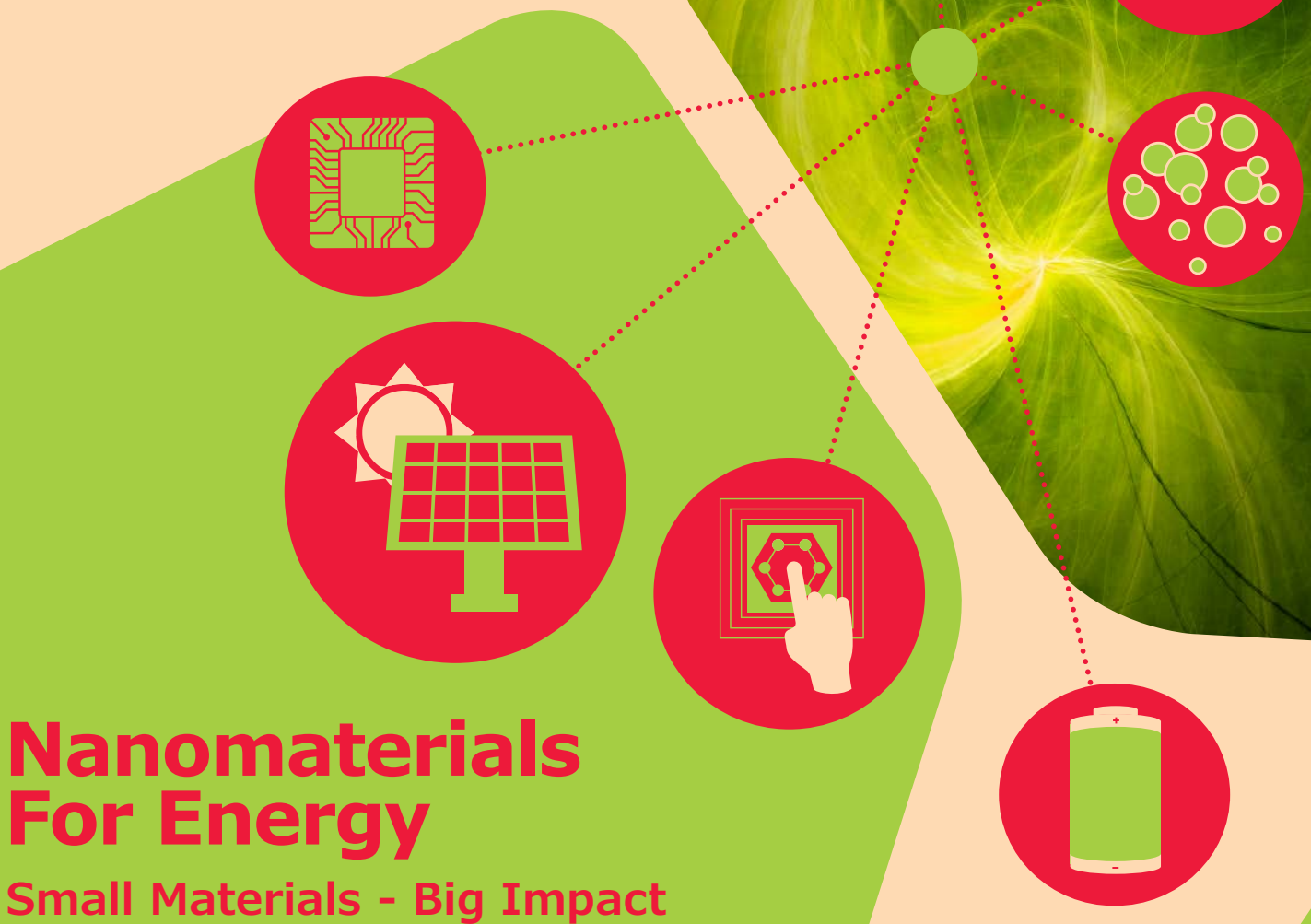


MERCK

Material Matters™

VOLUME 13 • NUMBER 1



Nanomaterials For Energy

Small Materials - Big Impact

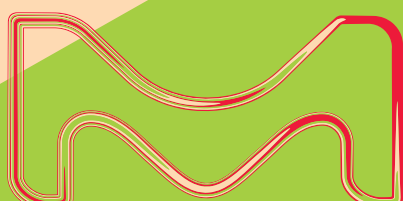
Recent Advances in Scalable Synthesis and Processing of TWO-DIMENSIONAL MATERIALS

Ultra-High Efficiency PEROVSKITE-PEROVSKITE TANDEM SOLAR CELLS

SYNTHESIS OF HALIDE PEROVSKITE QUANTUM DOTS for Display Applications

IONIC LIQUIDS BASED ELECTROLYTES for Rechargeable Batteries

The life science business of Merck operates as MilliporeSigma in the U.S. and Canada.



Introduction

**Niraj Singh**

Product Manager,
Energy Materials

Welcome to the first issue of Material Matters for 2018. In this issue we focus on the rapidly developing field of Nanomaterials for Energy.

Nanomaterials are defined as materials that have at least one dimension that is less than 100 nm. The last decade has brought significant development in the synthesis and fabrication of nanomaterials. This rapid progress suggests that nanomaterials will continue to contribute solutions to a number of today's biggest scientific challenges in the biomedical, electronics, and energy fields.

The ever-increasing global demand for energy has put tremendous pressure on conventional fossil fuel based resources. Over the past decade it has become apparent that alternative energy based on solar, wind and hydrogen will need to significantly contribute to meeting future demands. The use of nanomaterials to

harvest, store and conserve energy has recently attracted significant attention. Nanomaterials with engineered morphologies exhibit unique properties with potentially useful applications in solar cells, fuel cells, supercapacitors, sensors, light-emitting diodes and displays. It should also be emphasized that even though nanomaterials hold enormous potential to improve performance and lower costs in various devices, the full realization of such benefits has yet to be achieved in many cases. In order to realize the full potential of the nanomaterial revolution, a better understanding of the fundamental processes associated with energy conversion and storage, electron transport processes, as well as solutions to more practical challenges such as device integration and cost-effective large-scale production is still needed. In this edition of Material Matters both the fundamental and practical challenges involved in the synthesis and application of nanomaterials are addressed.

In the first article Profs. Mark Hersam (Northwestern University, USA) and Deep Jariwala (University of Pennsylvania, USA) present the advancements made both in the solution phase as well as the chemical vapor deposition synthesis methods of non-graphene based 2D materials. The article also highlights the potential applications of these materials.

Drs. Zhen Li and Kai Zhu (National Renewable Energy Laboratory, USA), in the second article, review the progress on perovskite-perovskite tandem solar cells. The importance of the bandgap engineering of the perovskite absorbers in the tandem structures has been highlighted in the article.

In third article Prof. Haizheng Zhong (Beijing Institute of Technology, China) highlights perovskite quantum dots (QDs). The article provides an overview of various techniques used for perovskite QDs synthesis. The properties of perovskite QDs for display applications are also discussed.

Prof. Hongjie Dai (Stanford University, USA), in the final article, provides a brief review of the ionic liquid electrolytes used in the development of new rechargeable batteries. Specifically, the performance of aluminum-based, lithium-based and dual-graphite batteries with ionic liquid electrolytes has been reviewed. The authors discuss in particular, the potential for ionic liquids as an electrolyte for low-cost batteries.

Each article in this publication is accompanied by a list of Sigma-Aldrich materials available from MilliporeSigma/Merck. For additional product information, visit us at **SigmaAldrich.com/matsci**. Please bother us with your new product suggestions, as well as thoughts and comments for *Material Matters*™ at **matsci@sial.com**.

Merck KGaA
Frankfurter Strasse 250
64293 Darmstadt, Germany
Phone +49 6151 72 0

To Place Orders / Customer Service
Contact your local office or visit
SigmaAldrich.com/order

Technical Service
Contact your local office or visit
SigmaAldrich.com/techinfo

General Correspondence
Materials Science
materialsscience@sial.com

Subscriptions
Request your FREE subscription to *Material Matters*™ at SigmaAldrich.com/mm

The entire *Material Matters*™ archive is available at SigmaAldrich.com/mm

Material Matters™(ISSN 1933-9631) is a publication of Merck KGaA.

Copyright (c) 2018 Merck KGaA, Darmstadt, Germany and/or its affiliates. All rights reserved. Merck, the vibrant M, and Material Matters are trademarks of Merck KGaA, Darmstadt, Germany or its affiliates. All other trademarks are the property of their respective owners. Detailed information on trademarks is available via publicly accessible resources. More information on our branded products and services on MerckMillipore.com

About the Cover

Advancements in alternative energy harvesting and storage, along with enhancements in energy efficiency are critical for meeting future energy demands as well as for reducing our carbon footprint. These could be achieved through material innovation and nanomaterials offer immense potential in this regard. The current cover emphasizes this fact and highlights conceptual images of nanomaterials and their connections to various energy related technologies.

Your Material Matters



Bryce P. Nelson

Bryce P. Nelson, Ph.D.
Materials Science Initiative Lead

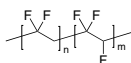
We welcome fresh product ideas. Do you have a material or compound you wish to see featured in our Materials Science line? If it is needed to accelerate your research, it matters. Send your suggestion to matsci@sial.com for consideration.

Dr. Albert van Breemen of Holst Centre (The Netherlands) recommended the addition of Solvène® P(VDF-TrFE) copolymers (Cat. Nos. **900895**, **900903**, **900905**, **900906**) to our catalog for use in solution processable electroactive material applications such as printed memory, sensors, actuators, loudspeakers, acoustic transducers, and energy harvesting devices.

P(VDF-TrFE) has several advantageous properties including a large remnant polarization, excellent polarization stability, low leakage for high resistivity and switching times as short as 1 microsecond. Furthermore, it is intrinsically bistable, i.e. it does not require a voltage to keep its polarization state. It can be processed from solution at low temperatures, opening the possibility for the use of a wide range of plastic substrates instead of glass. These properties make it ideally suited for next-generation organic electronics applications that require reprogrammable, non-volatile memories.

References

- (1) Naber, R.C.G.; Blom, P.W.M.; Marsman, A.W.; de Leeuw, D.M. *Appl. Phys. Lett.* **2004**, *85*, 2032.
- (2) van Breemen, A. J. J. M.; van der Putten, J. B. P. H.; Cai, R.; Reimann, K.; Marsman, A. W.; Willard, N.; de Leeuw, D. M.; Gelinck, G. H. *Appl. Phys. Lett.* **2011**, *98*, 183302.
- (3) Gelinck, G.; van Breemen, A. J. J. M.; Cobb, B. *Appl. Phys. Lett.* **2015**, *106*, 1.
- (4) Cai, R.; Kassa, H. G.; Marrani, A.; van Breeme, A. J. J. M.; Gelinck, G. H.; Nysten, B.; Hu, Z.; Jonas, A. M., *Appl. Phys. Lett.* **2014**, *105*, 113113.
- (5) van Breemen, A. J. J. M.; van der Steen, J.-L.; van Heck, G.; Wang, R.; Khikhlovskiy, V.; Kemerink, M.; Gelinck, G. H. *Appl. Phys. Express* **2014**, *7*, 031602.
- (6) Nougaret, L.; Kassa, H. G.; Cai, R.; Patois, T.; Nysten, B.; van Breemen, A. J. J. M.; Gelinck, G. H.; de Leeuw, D. M.; Marrani, A.; Hu, Z.; Jonas, A. M. *ACS Nano* **2014**, *8*, 3498.
- (7) Takahashi, S. *Ultrasonics* **2012**, *52*, 422.
- (8) Jel, S.-S.; Sharma, T.; Leel, Y.; Gill, B.; Zhani, J. X. *MEMS* **2011**, *644*.
- (9) Cheng, Z.-Y.; Bharti, V.; Xu, T.-B.; Xu, H.; Mai, T.; Zhang, Q.M. *Sens. Actuator, A* **2001**, *90*, 138.



Name	Description	Cat. No.
Solvène®200/P200	Curie peak: $131 \pm 3^\circ\text{C}$ MFI (melt flow index): 20-30	900895-10G
Solvène®200/P400	Curie peak: $131 \pm 3^\circ\text{C}$ MFI (melt flow index): 0.2-1.5	900903-10G
Solvène®250/P300	Curie Peak: $114 \pm 3^\circ\text{C}$ MFI (melt flow index): 2-8	900905-10G
Solvène®300/P300	Curie peak: $103 \pm 3^\circ\text{C}$ MFI (melt flow index): 2-8	900906-10G

Table of Contents

Articles

Recent Advances in Scalable Synthesis and Processing of Two-Dimensional Materials	3
Ultra-High Efficiency Perovskite-Perovskite Tandem Solar Cells	13
Synthesis of Halide Perovskite Quantum Dots for Display Applications	24
Ionic Liquids Based Electrolytes for Rechargeable Batteries	31

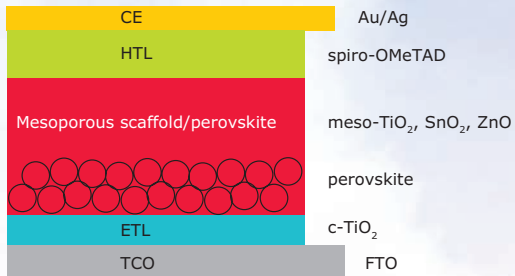
Featured Products

Inorganic 2D materials <i>A selection of powders, dispersions and crystals</i>	10
Graphene and Graphene Oxide <i>A selection of graphene powders, dispersions, inks, films, nanoplatelets, papers, and nanoribbons</i>	11
Precursors for Organometallic Perovskites <i>A list of high purity perovskite precursors for photovoltaics</i>	19
Titania Nanomaterials for Support <i>A selection of titania based nanomaterials for photovoltaics</i>	21
Hole Transport Materials (HTM) <i>A selection of HTM materials for use in solar cells</i>	21
Hole Conductor Cobalt Dopants <i>A selection of Co dopant materials</i>	22
Fluorine-Doped Tin Oxide (FTO) Coated Glass <i>A list of FTO glass</i>	23
Cadmium-Free Quantum Dots <i>A selection of PbS, perovskite, graphene and InP/ZnS quantum dots</i>	28
Cadmium-Based Quantum Dot <i>A list of core-type, core-shell type and alloyed quantum dots</i>	28
Electrode Sheets <i>A selection of ready-to-use electrode sheets</i>	36
Electrode Materials <i>A selection of anode and cathode materials</i>	37
Electrolyte Solutions <i>A list of ready-to-use electrolyte solutions</i>	37
Ionic Liquids <i>A selection of high-purity ionic liquids for batteries</i>	37
Electrolyte and Additive Materials <i>A list of high-purity electrolyte materials, high-purity solvents and additives</i>	38

Catch the Sun

Organohalide precursors for perovskites solar cells

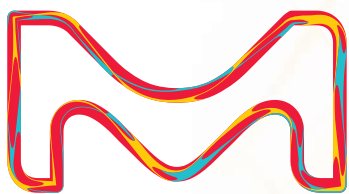
Organohalide-based perovskite materials exhibit high photon conversion efficiency and find applications as photosensitizers in solar cells. However, achieving high efficiency requires optimization of band gap and carrier diffusion length. Use our well characterized precursors to enhance performance of your cell.



Material Highlights

- Wide selection of organohalide precursors for bandgap optimization
- Hole transport materials & hole conductor dopants
- Ready to use titania nanomaterials for photoelectrodes
- Transparent conducting oxides

We are continually expanding our perovskites precursors offering. For a complete list, visit SigmaAldrich.com/perovskites.

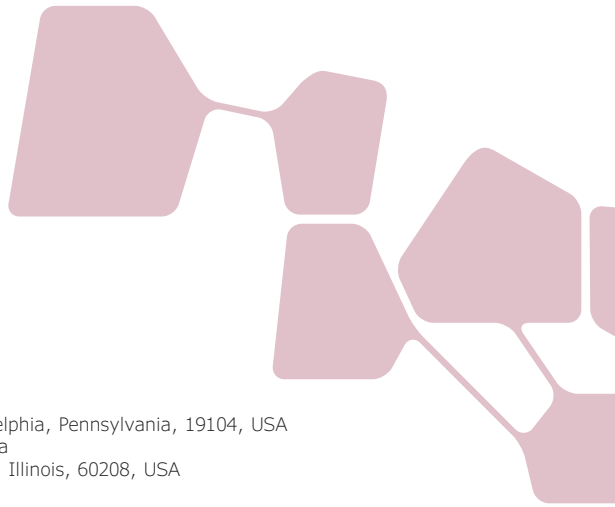


© 2018 Merck KGaA, Darmstadt, Germany and/or its affiliates. All Rights Reserved. Merck and the vibrant M are trademarks of Merck KGaA, Darmstadt, Germany or its affiliates. All other trademarks are the property of their respective owners. Detailed information on trademarks is available via publicly accessible resources.

The life science business of Merck operates as MilliporeSigma in the U.S. and Canada.

Sigma-Aldrich®
Lab & Production Materials

Recent Advances in Scalable Synthesis and Processing of Two-Dimensional Materials



Deep Jariwala,^{1*} Jian Zhu,² Jung-Woo Seo,³ and Mark C. Hersam^{3*}

¹Department of Electrical and Systems Engineering, University of Pennsylvania, Philadelphia, Pennsylvania, 19104, USA

²School of Materials Science and Engineering, Nankai University, Tianjin, 300350, China

³Department of Materials Science and Engineering, Northwestern University, Evanston, Illinois, 60208, USA

*Email: dmj@seas.upenn.edu, m-hersam@northwestern.edu

Introduction

The isolation of two-dimensional (2D) crystals from layered van der Waals bonded materials has brought about transformational progress in materials research for electronic, photonic, and energy device applications.^{1–5} These applications require large area and high volumes of active component materials to enable manufacturing and operation at practical scales. In particular, traditional energy generation, transport, and storage devices require large quantities of 2D materials, whether it is the conductive electrode layer material such as graphene or semiconducting absorber or catalyst layer materials such as transition metal dichalcogenides (TMDCs). While most early device demonstrations have used mechanically exfoliated samples, several advances have since been made on room-temperature solution-phase processing^{6–8} and high-temperature chemical vapor deposition^{9–13} for the synthesis and processing of 2D materials. While much of the early effort in this regard was applied to graphene, more recent large-scale synthesis and processing developments have focused on a wider set of 2D materials in addition to achieving precise control over their structure and properties. In this article, we provide a brief review detailing the most recent advances in synthesis and processing of 2D materials using solution phase and chemical vapor deposition methods, with particular emphasis on semiconductor materials beyond graphene.

Room-Temperature Solution-Phase Methods

Scalable production of 2D materials can be achieved by solution-based exfoliation methods.^{7,14–17} The relatively weak van der Waals interactions between layers in 2D crystals allow the peeling-off of nanomaterials consisting of monolayers or several layers through a consistent external energy input. One of the typical methods is ultrasonication in

appropriate liquids, including organic solvents or surfactant-based aqueous solutions. Exfoliated nanosheets, typically a few hundred nanometers in size, are stabilized in solution through the adsorption of molecules on the surfaces to avoid re-aggregation. A variety of 2D semiconducting nanomaterials, such as MoS₂, MoSe₂, WS₂, and SnS₂, have been produced in this way with proper choice of solvents (Figure 1A).¹⁸ This liquid exfoliation method can achieve defect-free nanocrystals, as evidenced by TEM images (Figures 1B and 1C).¹⁹ In order to increase the exfoliation efficiency, ionic species or small molecules have been intercalated between layers to allow subsequent exfoliation into monolayer nanosheets.^{20,21} However, this interaction can lead to irreversible phase changes, resulting in exfoliated materials with different electronic properties. In particular, 2H-MoS₂ intercalated with lithium ions converts into the metallic 1T-MoS₂ phase.²² Extensive thermal annealing cannot completely restore this metallic phase back to the pristine semiconducting structure, limiting its use as a semiconducting component in electronics. In addition to sonication, it is possible to achieve further larger-scale production of 2D materials through shear exfoliation (Figures 1D and 1E).^{23,24} The high-shear mixing of 2D crystals in suitable stabilizing liquids enables exfoliation of 2D materials in large volumes. Such scalable methods facilitate commercial production of 2D material dispersions.^{25–29} Using a similar strategy, chemically reactive 2D materials, such as black phosphorous (BP, Cat. No. 808970), have been exfoliated in anhydrous organic solvents in inert environments to avoid oxidation (Figure 1F and 1G).³⁰ The production of BP nanomaterials can also be achieved in deoxygenated water with the assistance of suitable surfactants.³¹

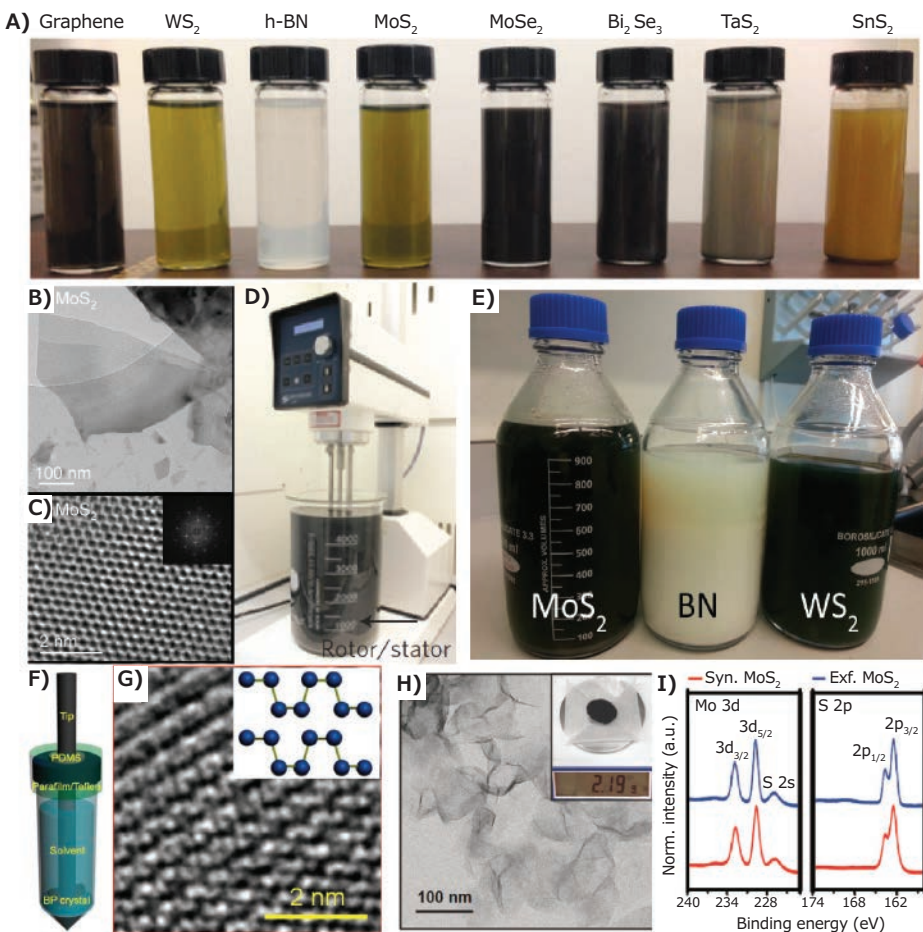


Figure 1. Solution-based processing of 2D semiconductors. A) Stable dispersions of various 2D materials obtained from liquid exfoliation.¹⁸ B) TEM image showing an exfoliated MoS₂ nanosheet.¹⁹ C) High-resolution TEM image of exfoliated MoS₂.¹⁹ D) Setup of large-scale shear exfoliation of 2D materials.²⁴ E) Shear-exfoliated dispersions of 2D materials.²³ F) Setup of a sealed container to minimize exposure to ambient air during tip ultrasonication.³⁰ G) High-resolution TEM image of an exfoliated black phosphorous nanosheet.³⁰ H) TEM image showing synthesized MoS₂ nanosheets. The inset shows the amount of MoS₂ produced by large-scale synthesis.³⁵ I) Comparison of XPS peaks of synthesized and exfoliated MoS₂ nanosheets.³⁵ Reprinted with permission: A, E, F, G copyright 2015 American Chemical Society; B, C copyright 2011 American Association for the Advancement of Science; D copyright 2015 MacMillan Publishers Ltd.; H, I copyright 2016 Wiley VCH.

In addition to the top-down exfoliation of 2D materials, it is possible to construct these nanomaterials using bottom-up solution-based synthesis.^{15,32} This colloidal growth of 2D nanocrystals may enable their scalable production for various applications. However, the anisotropy of 2D materials requires special control, such as ligands or defect engineering, during the growth process to induce 2D shapes.^{32,33} Various 2D semiconductor materials, such as MoS₂, MoSe₂, Bi₂Se₃, and InSe, have been produced synthetically.^{15,34} For example, bilayer MoS₂ nanosheets have been produced at the gram-scale using the thermal injection method from the precursors of MoCl₅, CS₂, and tetradecylphosphonic acid (**Cat. No. 736414**) dissolved in oleylamine.³⁵ The resulting MoS₂ nanosheets have similar structural and chemical properties to samples generated via exfoliation (**Figure 1H and 1I**), allowing the development of wafer-scale applications such as flexible nonvolatile memory devices.³⁵

Since most exfoliation methods lack perfect control over nanosheet size, significant research efforts have been devoted to the development of separation and purification methods.^{8,36,37}

In particular, the thickness-dependent electronic and optical properties of TMDCs and BP provide significant motivation for subsequent purification following exfoliation. Two essential attributes for purification methods are: (1) scalability in order to produce sufficient quantities for applications; (2) ability to maintain the pristine electronic properties of the original 2D semiconductor materials. Towards these ends, sequential centrifugation has emerged as a general method for separating 2D semiconductor materials by their area and thickness (**Figure 2A**).^{30,31,38} In contrast to techniques involving ultracentrifugation,⁷ sequential centrifugation offers greater scalability with processing volumes that range from few tens of milliliters to tens of liters. In addition, the use of centrifugation with low g-force requirement allows for compatibility with organic solvents, which is advantageous for tuning the rheology while maximizing the solid content of purified dispersions. These attributes enable application of enriched 2D materials, namely TMDCs and BP, with multiple film fabrication methods such as vacuum filtration, drop casting, and printing.

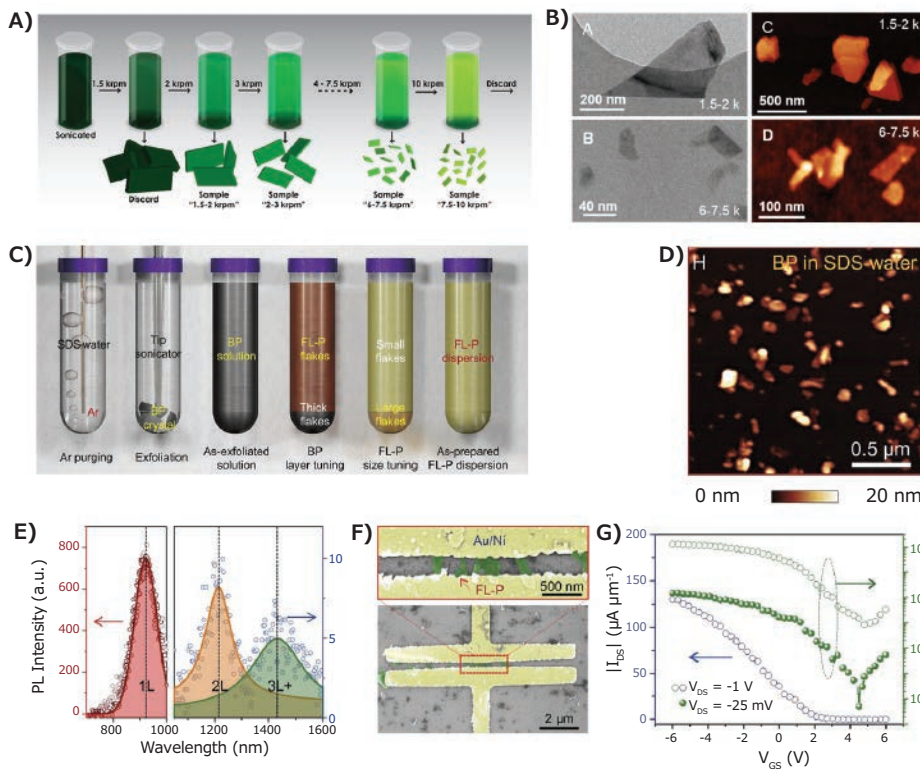


Figure 2. Scalable solution-phase purification of 2D semiconductor materials by sequential centrifugation. **A)** Schematic view of a general preparation method for dispersions of 2D materials with distinct distributions of area and thickness using sequential centrifugation steps.³⁸ **B)** TEM and AFM images of representative WS_x flakes that have been enriched towards achieving large size (1.5-2 kilo rotations per minute) versus low thickness (6-7.5 kilo rotations per minute).³⁸ **C)** Schematic view of a sequential centrifugation process for air-sensitive BP flakes.³¹ **D)** AFM image of as-prepared few-layer phosphorene (FL-P).³¹ **E)** Photoluminescence from the FL-P dispersion that shows the characteristic behavior of pristine BP flakes.³¹ **F)** SEM image of a FL-P FET. **G)** Transfer curve from a FL-P FET.³¹ Reprinted with permission: A-B copyright 2016 American Chemical Society; C-G copyright 2016 National Academy of Sciences, U.S.A.

Essentially, the purification process includes multiple centrifugation steps with varying sedimentation force applied to the suspended flakes. Once a dispersion is centrifuged minimally to sediment the large, unexfoliated aggregates, the supernatant is subjected to increasing centrifugal conditions and collected at different intervals. This step-wise approach enables the isolation of populations with different distribution of area and thickness, as demonstrated in **Figure 2B**. For instance, large and thick flakes are well-suited for applications where a percolating composite structure is needed, whereas a sample with the greatest distribution of thin flakes with reasonable lateral size enables transistor devices. Most recently, sequential centrifugation has been utilized to prepare purified dispersions of BP flakes (**Figure 2C**).^{30,31} Due to the high sensitivity of BP towards chemical degradation in air, exfoliation and centrifugation are performed with minimal ambient exposure. With these precautions, sequential centrifugation allows the preparation of few-layer phosphorene (FL-P) with average thickness of 4.5 nm (**Figure 2D**).³⁰ Most importantly, the pristine optical and electronic properties of BP are preserved through the preparation process, as demonstrated in **Figure 2E-G**.³⁰ Thickness-dependent photoluminescence of BP was observed from the enriched dispersions, and field-effect transistors fabricated with FL-P showed comparable I_{ON}/I_{OFF} value to the devices based on micromechanically exfoliated BP flakes, thus showing that this approach produces electronic-grade 2D semiconductor materials.

High-Temperature Chemical Vapor Deposition

While solution-phase synthesis and processing have scalability advantages, these methods do not produce materials that can be assembled into continuous monolayer thin films.⁷ Instead, thin films assembled from solution-processed material have a percolating network of flakes with van der Waals electronic contacts that limit charge transport. For high-performance optical and electronic devices, superior crystalline quality is often required. In contrast to solution-phase approaches, high-temperature synthesis and deposition allows the growth of large crystals with high electronic quality in the resulting films. The elevated temperature of the growth permits thermal diffusion and kinetics necessary for crystallization with minimal defects. Chemical vapor deposition (CVD) is one such technique that has been widely used for synthesizing a range of 2D materials.^{9,10,13,39} CVD relies on the introduction of precursor vapors in the hot-zone of a reactor where the deposition substrate is placed. The precursors undergo pyrolysis followed by chemical reaction in the gas phase and/or on the substrate to form the resulting film. Over the past decade, numerous results have been published on CVD synthesis of 2D materials ranging from graphene and boron nitride to TMDCs. Most of them have been summarized in comprehensive review articles.^{9,10,13,40} Here, we focus on the latest developments in the synthesis, manipulation, and control over growth of 2D materials. Special emphasis is given to

growth parameters such as substrate, nucleation, and precursor engineering in addition to doping and heterostructure synthesis.

CVD is often classified based on the type of substrates and precursors that are used as well as the growth pressure. For synthesis of 2D materials such as graphene and boron nitride, catalytically active substrates have been the most widely and commonly used strategy. Foils or thin films of transition metals such as copper or nickel have been the most popular catalytic growth substrates for graphene¹³ and h-BN.⁴⁰ For TMDCs, CVD does not necessarily require catalytic activity. Early reports of MoS₂ growth used sulfurization of Mo thin films.⁴¹ Subsequently, high-quality growth was reported by pyrolysis of metal-organic compounds containing both Mo and S such as ammonium

thiomolybdate⁴² (**Cat. No. 323446**) or by sublimation of powder precursors such as MoO₃ and elemental S.⁴³ Numerous reports detailing the growth and characterization of TMDC materials using the above methods have been summarized in recent reviews.^{9,10} A majority of the reported syntheses used amorphous SiO₂ substrates. Due to the weak interaction of the growing 2D layer with the substrate, the individual islands tend to be randomly oriented.^{43,44} However, the use of a single-crystal substrate such as epitaxial graphene on SiC⁴⁵ or (0001) sapphire⁴⁶ (**Cat. No. 634875**) leads to quasi van der Waals epitaxy of the TMDC lattice and helps align the individual islands along the same crystallographic orientation (**Figure 3A**). The aligned islands then merge together to form a macroscopic, continuous monolayer sheet that is single crystalline.⁴⁶

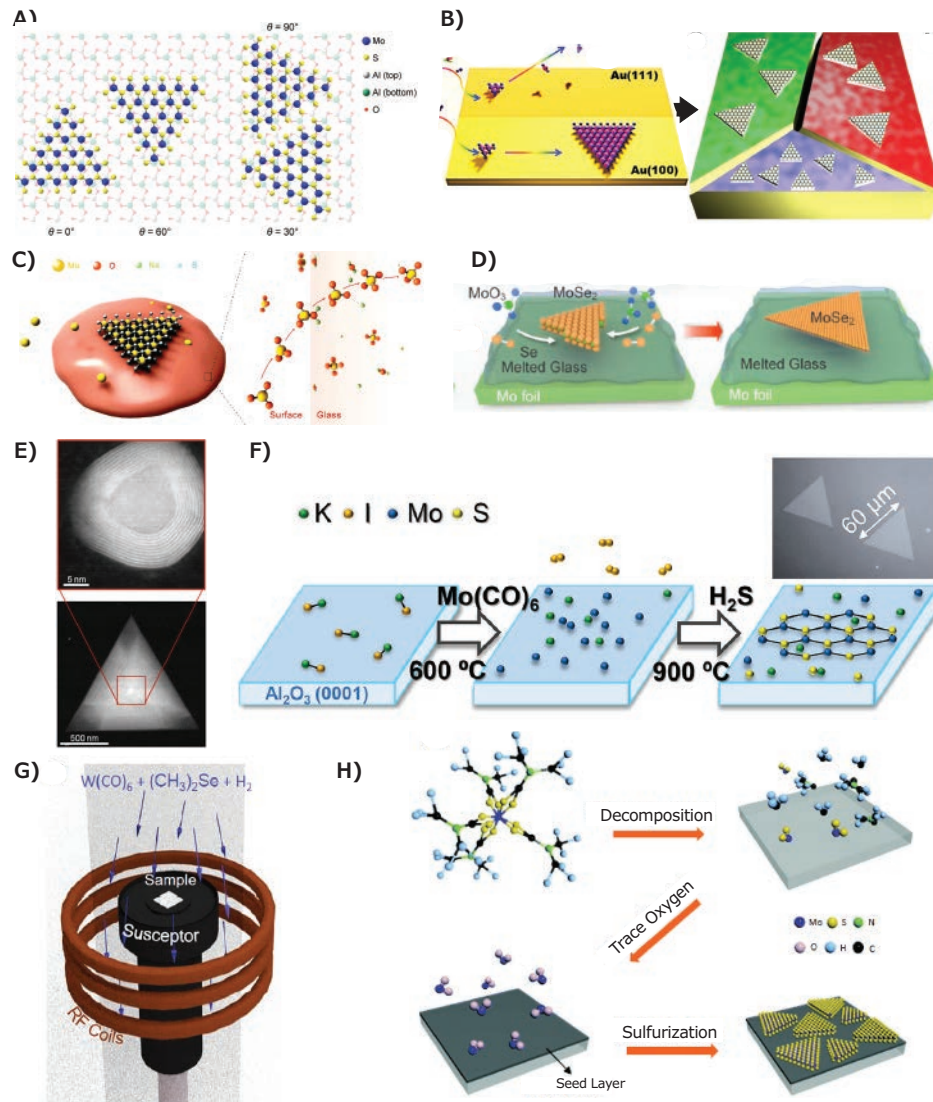


Figure 3. Substrate and nucleation engineering for growth control. **A)** Sapphire substrates control van der Waals epitaxy in a manner that results in crystallographic alignment of all MoS₂ islands, allowing the formation of a single-crystal monolayer.⁴⁶ **B)** Catalytically active substrates such as Au foils allow growth at lower temperatures, and different crystal orientations of the Au support provide different nucleation and growth rates.⁴⁹ **C,D)** Soda lime glass (C) has been used to trap/dissolve small amounts of MoO₃ precursor in the glass substrate which when passed over by S results in the growth of monolayer MoS₂ crystals.⁵⁰ Likewise, molten silica glass (D) presents an atomically smooth surface enhancing diffusion for the growth of millimeter-scale single crystals of MoS₂ and MoSe₂.⁵¹ **E)** Powder precursor growth often results in a TMDC fullerene nucleus encapsulating an oxide crystal that gets consumed and results in lateral 2D growth upon further sulfurization.⁵² **F)** Metal organic chemical vapor deposition (MOCVD) helps overcome the shortcoming of conventional CVD using powder precursors, but also requires nucleation assistance by alkali metals such as K and Na.⁵⁴ **G)** MOCVD has also been demonstrated in a cold-walled vertical reactor using induction heaters to grow WSe₂.⁵⁵ **H)** Careful design of the metal organic precursor can allow incorporation of the metal source and seeding layer in the same molecule to promote uniform nucleation and growth.⁵⁶ Reprinted with permission: A-F copyright 2015, 2016, 2017 American Chemical Society; G copyright 2016 Institute of Physics Publishing; H copyright 2016 The Royal Society of Chemistry.

Likewise, substrates can also influence the growth in terms of nucleation density and rate of growth. For example, Au foils are catalytically active for sulfurization reactions and hence are used to grow large-area, single crystals of TMDCs and polycrystalline films.⁴⁷ The advantage of using catalytic metal substrates is the growth is limited strictly to a monolayer since the catalytic activity is diminished upon completion of monolayer growth.⁴⁸ Furthermore, the crystallographic orientations of the underlying Au foil affect the nucleation and rate of growth. Specifically, the (100) and (110) facets are more favorable for large grain growth (**Figure 3B**) due to differences in binding energy of the precursors to the facets.⁴⁹ In addition to catalytic activity, dissolution of precursors in the substrate can help restrict the thickness of grown films towards the monolayer limit. At high temperatures, molten soda-lime glass dissolves a small amount of MoO₃. The dissolved MoO₃ can then be sulfurized at lower temperatures to grow MoS₂ and WS₂ monolayers (**Figure 3C**).⁵⁰ Substrate smoothness and precursor solubility also play critical roles in nucleation since molten glass/SiO₂ provides a much smoother surface for growth, leading to large single crystals of MoSe₂ with record field-effect mobilities at room temperature (**Figure 3D**).⁵¹

Precise control over nucleation is thus key to the synthesis of high-quality monolayers with minimal line defects such as grain boundaries. This challenge has led to several studies to investigate the fundamental structure and nature of nucleation for TMDC growth. High-resolution electron microscopy has recently revealed that the initial nucleation event resembles a MoO₃ nanoparticle encapsulated by a MoS₂ fullerene (**Figure 3E**).⁵² Upon sulfurization, 2D atomic layer growth occurs depending on the interaction of this fullerene-encapsulated nanoparticle with the underlying substrate. This lends credibility to prior observations of the influence of moisture in the creation of MoO₃ seeds that ultimately promote nucleation of MoS₂. While sublimation of powder precursors provides a viable solution for laboratory-scale experiments, the use of solid powder sources leads to inhomogeneous nucleation and thus uncontrolled thickness of the resulting TMDC. Therefore, recent efforts have focused on metal-organic gas-phase precursors for uniform large-area growth. In particular, metal-organic chemical vapor deposition (MOCVD) allows the growth of monolayer TMDCs over large areas with high quality.⁵³ Molybdenum and tungsten hexacarbonyls are the preferred metal sources while dimethyl and diethyl sulfides and selenides as well as hydrogen sulfide and selenide have been used as the chalcogen precursors.⁵³⁻⁵⁵ However, nucleation of the crystals from the gas phase onto the solid substrate remains a challenge. While highly aromatic perylene-based molecules with a graphite-like core have served as nucleation centers in powder precursor CVD, the MOCVD precursors have also worked well with alkali metal salts.⁵⁴ The early presumption was that alkali metal salts serve as moisture

desiccants. More recently, though, it was discovered that they serve as nucleating agents if the substrate is exposed to alkali metal halides such as KI or NaCl and then to the metal precursor before performing the actual growth (**Figure 3F**).⁵⁴ Control over nucleation has also been achieved in a cold-walled MOCVD setup (**Figure 3G**) where an extra temperature step is added between 550-700 °C below the growth temperature of 900 °C to form small clusters (15-40 nm) of the precursor material that act as the nucleation sites.⁵⁵ Furthermore, with the wide variety of metal-organic compounds available, more complex precursors such as molybdenum dimethyldithiocarbamate (Mo DMDTC) have been used that act as both the source of metal atoms and organic nucleation promoters (**Figure 3H**).⁵⁶

The previous paragraphs discussed recent developments in CVD and MOCVD synthesis of high-quality, pure, stoichiometric TMDC compounds as atomically thin layers. Modern semiconductor technology, however, heavily depends on the ability to manipulate the properties of semiconductor materials and integrate them with other semiconductors, metals, or insulators into heterostructures. In this regard, several attempts have been made to directly synthesize doped or alloyed semiconducting 2D materials and heterostructures. Since previous review articles have commented on doping and heterostructure growth of 2D semiconductors,⁵⁷⁻⁵⁹ here we focus primarily on the most recent developments in substitutional doping and heterostructure growth of 2D semiconductors.

Doping is critical for most semiconductor applications. The ability to tune electron and hole concentrations lies at the heart of semiconductor electronic and optoelectronic devices. A majority of 2D TMDCs naturally occur as n-type doped.^{1,60} In contrast p-type 2D semiconductor materials are relatively rare, aside from ambient-exposed black phosphorus.^{61,62} Therefore, substitutional doping of TMDC lattices is critical to achieve complementary semiconductor technology from purely 2D TMDCs. Recently, such substitutional doping was systematically achieved in WS₂ and MoS₂ through the use of solid-state dopant precursors during growth. For example, the addition of niobium chloride enabled small amounts of Nb to replace W in the WS₂ lattice (**Figure 4A**). The dopant precursor was supplied along with the chalcogen (S) to ensure uniform delivery and doping. Since Nb has one less valence electron (5) than W (6), it is expected to be a p-type dopant for WS₂. Likewise, rhenium (7 valence electrons) instead of 6 for Mo serves as an n-type dopant for MoS₂.⁶³ The doping in TMDCs can be extended further into heavy alloying of atomic components both on the metal as well as the chalcogen side. While ternary alloys have been synthesized and characterized in great detail,^{64,65} only recently quaternary alloys of the Mo-W-S-Se system have been synthesized. High-resolution electron micrographs indicate that Mo dominates the metal sites in the MX₂ configuration, while a hybrid Se-S configuration dominates the chalcogen (X) sites

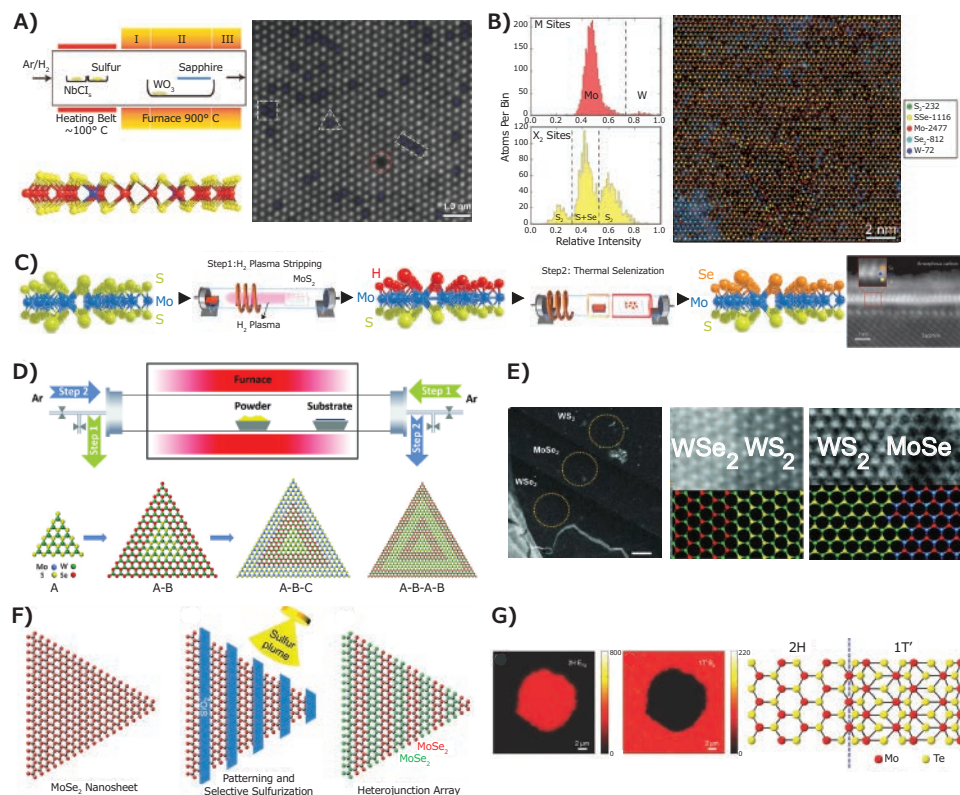


Figure 4. Controlled doping and growth of heterostructures. **A)** Schematic setup for doping a WS_2 monolayer with Nb atoms (left). Atomic-resolution micrograph showing the Nb dopants in blue in addition to other defects such as vacancies (right).⁶³ **B)** Quaternary solid solution of Mo, W, S, and Se atomic layer with the respective distributions of metal and chalcogen atom sites (left). Atomic-resolution micrograph with color coded atoms (right).⁶⁶ **C)** Schematic synthesis procedure for a Janus TMDC monolayer that consists of Se-Mo-S layered sequentially within a single three-atom thick layer.⁶⁸ **D)** Schematic dual-direction carrier gas flow setup for sequentially growing in-plane TMDC multi-heterojunctions and superlattices.⁷³ **E)** Ball and stick atomic structures of multi-heterojunctions and high-resolution electron micrographs of junction interfaces.⁷³ **F)** Schematic of top-down superlattice synthesis using lithographically patterned sulfurization of MoSe_2 .⁷⁴ **G)** Raman maps showing in-plane heterojunctions of the 2H semiconducting and 1T metallic phase of MoTe_2 with corresponding ball and stick schematic.⁷⁶ Reprinted with permission: A, B, G copyright 2016, 2017 Wiley VCH; C, F copyright 2015 MacMillan Publishers Ltd.; D, E copyright 2017 American Association for the Advancement of Science.

followed by Se_2 and a minority of S_2 sites (Figure 4B).⁶⁶ All four elements were found to be in random solid-solution type-distribution with no obvious nanoscopic domain formation.⁶⁶ While solid-solution alloys are useful for obtaining materials with precise and tunable band gaps, an ordered structure often results in intrinsically novel properties. In an MX_2 TMDC layer, such an ordered structure can be visualized by having all top chalcogen atoms being S and all bottom chalcogen atoms being Se to obtain a Janus monolayer semiconductor.^{67,68} Such Janus TMDCs have recently been achieved through a growth method where the top layer of S or Se is etched away by hydrogen plasma to leave a meta-stable hydrogen terminated H-Mo-S or H-Mo-Se monolayer. Subsequently, the introduction of Se or S vapors leads to the formation of ordered Se-Mo-S or vice versa (Figure 4C). The high out-of-plane structural asymmetry results in large second-order susceptibility ratios and an out-of-plane piezoelectric response.⁶⁸

Ordered structures can also be grown in-plane resulting in lateral heterojunctions from two lattice matched 2D materials stitched together in the same plane. Numerous reports of such in-plane

epitaxial heterojunctions exist already.^{69,70} However, little is known about the growth control parameters that lead to in-plane epitaxial growth of heterojunctions. Some observations suggest the cleanliness of the initial seed-island⁷¹ or the presence of alkali metal salt (e.g., NaCl) are important in the lateral nucleation and growth of the next layer from the edge of the seed.⁷² Yet, there remains a need for a systematic synthetic pathway to highly scaled heterojunctions, multi-heterojunctions, and superlattices. Recent work has made progress towards these goals via several different methods. For example, reversing the gas flow during growth provides unique synthetic control (Figure 4D), resulting in epitaxial, defect-free, multi-heterojunction and superlattice interfaces (Figure 4E).⁷³ Another method utilizes top-down lithography for masking and conditions where S replaces Se to create superlattices and heterojunctions of desired dimensions (Figure 4F).⁷⁴ A related strategy etches out the desired pattern using a focused ion beam and then regrows another material in the etched pattern.⁷⁵ Finally, controlled heterostructures between structural and electronic phases (2H semiconducting and 1T metallic) have been achieved in MoTe_2 by controlling the vapor pressure and flux of tellurium (Figure 4G).⁷⁶

Applications, Summary, and Outlook

In summary, recent developments in solution-phase and high-temperature growth and processing of 2D materials have resulted in significant progress towards achieving precise control over the quality, interface, polydispersity, structure, and doping in 2D semiconductors. These improvements are having direct impact on practical applications, even at the technology levels. In particular, the expansion of large-scale solution-phase synthesis of 2D materials has enabled thermoelectric,⁷⁷ photovoltaic,^{78,79} electrochemical,^{80,81} and photocatalytic⁸² applications. For the case of thermoelectrics, 2D TMDCs have much higher thermoelectric power factors⁷⁷ compared to the bulk, and composites of TMDCs and graphene show high Seebeck coefficients.⁸³

For optoelectronics, the absorption cross sections of TMDCs are among the highest reported for semiconductor materials. This superlative optical absorption combined with their self-passivated and atomically thin nature makes them attractive candidates for photovoltaic acceptors in heterojunction solar cells.⁸⁴ Likewise, the high catalytic activity of defect sites allows them to play dual roles of absorbers and catalysts for photocatalytic⁸² and photoelectrochemical reactions. The availability of high-quality monolayer to multilayer thin films with controlled doping and heterostructuring has further presented new opportunities in solid-state devices. Specifically, 2D semiconductors with direct band gaps in the visible portion of the electromagnetic spectrum are facilitating unprecedented performance enhancements in optoelectronic devices such as photovoltaics^{78,79} and light-emitting diodes (LEDs).^{85,86} For thin-film inorganic photovoltaics, atomic-scale thickness enables superior charge collection upon photoexcitation. This attribute combined with light trapping techniques results in photovoltaics with few-nanometer thick absorber layers that are ideal for mobile and space-based solar power. The absence of dangling bonds also minimizes non-radiative recombination in 2D semiconductors, leading to the observation of near-unity photoluminescence quantum yields, with clear implications for high-efficiency light-emitting diodes.⁸⁵ Furthermore, given the covalent and inorganic nature of 2D materials, they possess higher thermal and ambient stability compared to organic emitters.

This review is largely centered on applications of 2D materials in mainstream devices and technologies. Moving forward, one of the key challenges will be to identify device structures and applications where the use of 2D semiconductors has a unique advantage over incumbent materials or technologies. Many of the most promising directions are attempting to exploit the defect-free van der Waals interfaces beyond purely layered 2D materials in mixed-dimensional heterostructure architectures,⁸⁷ where properties can be actively tuned under the application of electric fields and strain. Further improvements in 2D material quality and optimization of buried van der Waals interfaces will help accelerate progress in this regard.

References

- (1) Jariwala, D.; Sangwan, V. K.; Lauhon, L. J.; Marks, T. J.; Hersam, M. C. *ACS Nano* **2014**, *8*, 1102-1120.
- (2) Fiori, G.; Bonaccorso, F.; Iannaccone, G.; Palacios, T.; Neumaier, D.; Seabaugh, A.; et al. *Nat. Nanotechnol.* **2014**, *9*, 768-779.
- (3) Koppens, F. H. L.; Mueller, T.; Avouris, P.; Ferrari, A. C.; Vitiello, M. S.; Polini, M. *Nat. Nanotechnol.* **2015**, *9*, 780-793.
- (4) Bhimanapati, G. R.; Lin, Z.; Meunier, V.; Jung, Y.; Cha, J.; Das, S.; et al. *ACS Nano* **2015**, *9*, 11509-11539.
- (5) Butler, S. Z.; Hollen, S. M.; Cao, L.; Cui, Y.; Gupta, J. A.; Gutiérrez, H. R.; et al. *ACS Nano* **2013**, *7*, 2898-2926.
- (6) Ryder, C. R.; Wood, J. D.; Wells, S. A.; Hersam, M. C. *ACS Nano* **2016**, *10*, 3900-3917.
- (7) Kang, J.; Sangwan, V. K.; Wood, J. D.; Hersam, M. C. *Acc. Chem. Res.* **2017**, *50*, 943-951.
- (8) Kang, J.; Seo, J. W.; Alducin, D.; Ponce, A.; Yacaman, M. J.; Hersam, M. C. *Nat. Commun.* **2014**, *5*, 5478.
- (9) Li, H.; Li, Y.; Aljbar, A.; Shi, Y.; Li, L.-J. *Chem. Rev.* **2017**, DOI: 10.1021/acs.chemrev.7b00212.
- (10) Shi, Y.; Li, H.; Li, L.-J. *Chem. Soc. Rev.* **2015**, *44*, 2744-2756.
- (11) Chhowalla, M.; Shin, H. S.; Eda, G.; Li, L.-J.; Loh, K. P.; Zhang, H. *Nat. Chem.* **2013**, *5*, 263-275.
- (12) Liu, H. F.; Wong, S. L.; Chi, D. Z. *Chem. Vap. Dep.* **2015**, *21*, 241-259.
- (13) Mattevi, C.; Kim, H.; Chhowalla, M. *J. Mat. Chem.* **2011**, *21*, 3324-3334.
- (14) Bonaccorso, F.; Bartolotta, A.; Coleman, J. N.; Backes, C. *Adv. Mater.* **2016**, *28*, 6136-6166.
- (15) Zhu, J.; Hersam, M. C. *Adv. Mater.* **2017**, *29*, 1603895.
- (16) Niu, L.; Coleman, J. N.; Zhang, H.; Shin, H.; Chhowalla, M.; Zheng, Z. *Small* **2016**, *12*, 272-293.
- (17) Nicolosi, V.; Chhowalla, M.; Kanatzidis, M. G.; Strano, M. S.; Coleman, J. N. *Science* **2013**, *340*, 1420.
- (18) Shen, J. F.; He, Y. M.; Wu, J. J.; Gao, C. T.; Keyshar, K.; Zhang, X.; et al. *Nano Lett.* **2015**, *15*, 5449-5454.
- (19) Coleman, J. N.; Lotya, M.; O'Neill, A.; Bergin, S. D.; King, P. J.; Khan, U.; et al. *Science* **2011**, *331*, 568-571.
- (20) Zhang, X.; Xie, Y. *Chem. Soc. Rev.* **2013**, *42*, 8187-8199.
- (21) Wang, Q. H.; Kalantar-Zadeh, K.; Kis, A.; Coleman, J. N.; Strano, M. S. *Nat. Nanotechnol.* **2012**, *7*, 699-712.
- (22) Splendiani, A.; Sun, L.; Zhang, Y. B.; Li, T. S.; Kim, J.; Chim, C. Y.; et al. *Nano Lett.* **2010**, *10*, 1271-1275.
- (23) Varrla, E.; Backes, C.; Paton, K. R.; Harvey, A.; Gholamvand, Z.; McCauley, J.; et al. *Chem. Mater.* **2015**, *27*, 1129-1139.
- (24) Paton, K. R.; Varrla, E.; Backes, C.; Smith, R. J.; Khan, U.; O'Neill, A.; et al. *Nat. Mater.* **2014**, *13*, 624-630.
- (25) Secor, E. B.; Hersam, M. C. *J. Phys. Chem. Lett.* **2015**, *6*, 620-626.
- (26) Hyun, W. J.; Secor, E. B.; Hersam, M. C.; Frisbie, C. D.; Francis, L. F. *Adv. Mater.* **2015**, *27*, 109-115.
- (27) Secor, E. B.; Lim, S.; Zhang, H.; Frisbie, C. D.; Francis, L. F.; Hersam, M. C. *Adv. Mater.* **2014**, *26*, 4533-4538.
- (28) Secor, E. B.; Prabhumiresh, P. L.; Puntambekar, K.; Geier, M. L.; Hersam, M. C. *J. Phys. Chem. Lett.* **2013**, *4*, 1347-1351.
- (29) Secor, E. B.; Gao, T. Z.; Islam, A. E.; Rao, R.; Wallace, S. G.; Zhu, J.; et al. *Chem. Mater.* **2017**, *29*, 2322-2340.
- (30) Kang, J.; Wood, J. D.; Wells, S. A.; Lee, J. H.; Liu, X. L.; Chen, K. S.; et al. *ACS Nano* **2015**, *9*, 3596-3604.
- (31) Kang, J.; Wells, S. A.; Wood, J. D.; Lee, J. H.; Liu, X. L.; Ryder, C. R.; et al. *Proc. Natl. Acad. Sci. U.S.A* **2016**, *113*, 11688-11693.
- (32) Nasilowski, M.; Mahler, B.; Lhuillier, E.; Ithurria, S.; Dubertret, B. *Chem. Rev.* **2016**, *116*, 10934-10982.
- (33) Son, J. S.; Yu, J. H.; Kwon, S. G.; Lee, J.; Joo, J.; Hyeon, T. *Adv. Mater.* **2011**, *23*, 3214-3219.
- (34) Buha, J.; Gaspari, R.; Castillo, A. E. D.; Bonaccorso, F.; Manna, L. *Nano Lett.* **2016**, *16*, 4217-4223.
- (35) Son, D.; Chae, S. I.; Kim, M.; Choi, M. K.; Yang, J.; Park, K.; et al. *Adv. Mater.* **2016**, *28*, 9326-9332.
- (36) Green, A. A.; Hersam, M. C. *Nano Lett.* **2009**, *9*, 4031-4036.
- (37) Zhu, J.; Kang, J.; Kang, J.; Jariwala, D.; Wood, J. D.; Seo, J.-W. T.; et al. *Nano Lett.* **2015**, *15*, 7029-7036.
- (38) Backes, C.; Szydlowska, B. M.; Harvey, A.; Yuan, S. J.; Vega-Mayoral, V.; Davies, B. R.; et al. *ACS Nano* **2016**, *10*, 1589-1601.
- (39) Lin, W.-H.; Brar, V. W.; Jariwala, D.; Sherrrott, M. C.; Tseng, W.-S.; Wu, C.-I.; et al. *Chem. Mater.* **2017**, *29*, 4700-4707.
- (40) Pakdel, A.; Bando, Y.; Golberg, D. *Chem. Soc. Rev.* **2014**, *43*, 934-959.
- (41) Zhan, Y.; Liu, Z.; Najmaei, S.; Ajayan, P. M.; Lou, J. *Small* **2012**, *8*, 966-971.
- (42) Liu, K.-K.; Zhang, W.; Lee, Y.-H.; Lin, Y.-C.; Chang, M.-T.; Su, C.-Y.; et al. *Nano Lett.* **2012**, *12*, 1538-1544.
- (43) Najmaei, S.; Liu, Z.; Zhou, W.; Zou, X.; Shi, G.; Lei, S.; et al. *Nat. Mater.* **2013**, *12*, 754-759.
- (44) Lee, Y.-H.; Zhang, X.-Q.; Zhang, W.; Chang, M.-T.; Lin, C.-T.; Chang, K.-D.; et al. *Adv. Mater.* **2012**, *24*, 2320-2325.

- (45) Liu, X.; Balla, I.; Bergeron, H.; Campbell, G. P.; Bedzyk, M. J.; Hersam, M. C. *ACS Nano* **2016**, *10*, 1067-1075.
- (46) Dumcenco, D.; Ovchinnikov, D.; Marinov, K.; Lazić, P.; Gibertini, M.; Marzari, N.; et al. *ACS Nano* **2015**, *9*, 4611-4620.
- (47) Gao, Y.; Liu, Z.; Sun, D.-M.; Huang, L.; Ma, L.-P.; Yin, L.-C.; et al. *Nat. Commun.* **2015**, *6*, 8569.
- (48) Shi, J.; Ma, D.; Han, G.-F.; Zhang, Y.; Ji, Q.; Gao, T.; et al. *ACS Nano* **2014**, *8*, 10196-10204.
- (49) Shi, J.; Zhang, X.; Ma, D.; Zhu, J.; Zhang, Y.; Guo, Z.; et al. *ACS Nano* **2015**, *9*, 4017-4025.
- (50) Ju, M.; Liang, X.; Liu, J.; Zhou, L.; Liu, Z.; Mendes, R. G.; et al. *Chem. Mater.* **2017**, *29*, 6095-6103.
- (51) Chen, J.; Zhao, X.; Tan, S. J. R.; Xu, H.; Wu, B.; Liu, B.; et al. *J. Am. Chem. Soc.* **2017**, *139*, 1073-1076.
- (52) Cain, J. D.; Shi, F.; Wu, J.; Dravid, V. P. *ACS Nano* **2016**, *10*, 5440-5445.
- (53) Kang, K.; Xie, S.; Huang, L.; Han, Y.; Huang, P. Y.; Mak, K. F.; et al. *Nature* **2015**, *520*, 656-660.
- (54) Kim, H.; Ovchinnikov, D.; Deiana, D.; Unuchek, D.; Kis, A. *Nano Lett.* **2017**, *17*, 5056-5063.
- (55) Eichfeld, S. M.; Colon, V. O.; Nie, Y.; Cho, K.; Robinson, J. A. *2D Mater.* **2016**, *3*, 025015.
- (56) Liu, L.; Qiu, H.; Wang, J.; Xu, G.; Jiao, L. *Nanoscale* **2016**, *8*, 4486-4490.
- (57) Lotsch, B. V. *Ann. Rev. Mater. Res.* **2015**, *45*, 85-109.
- (58) Das, S.; Robinson, J. A.; Dubey, M.; Terrones, H.; Terrones, M. *Ann. Rev. Mater. Res.* **2015**, *45*, 1-27.
- (59) Novoselov, K.; Mishchenko, A.; Carvalho, A.; Neto, A. C. *Science* **2016**, *353*, 461.
- (60) Jariwala, D.; Sangwan, V. K.; Late, D. J.; Johns, J. E.; Dravid, V. P.; Marks, T. J.; et al. *Appl. Phys. Lett.* **2013**, *102*, 173107.
- (61) Whitney, W. S.; Sherrrott, M. C.; Jariwalam D.; Lin, W.-H.; Bechtel, H. A.; Rossman, G. R.; et al. *Nano Lett.* **2017**, *17*, 78-84.
- (62) Wood, J. D.; Wells, S. A.; Jariwala, D.; Chen, K.-S.; Cho, E.; Sangwan, V. K.; et al. *Nano Lett.* **2014**, *14*, 6964-6970.
- (63) Gao, J.; Kim, Y. D.; Liang, L.; Idrobo, J. C.; Chow, P.; Tan, J.; et al. *Adv. Mater.* **2016**, *28*, 9735-9743.
- (64) Chen, Y.; Xi, J.; Dumcenco, D. O.; Liu, Z.; Suenaga, K.; Wang, D.; et al. *ACS Nano* **2013**, *7*, 4610-4616.
- (65) Gong, Y.; Liu, Z.; Lupini, A. R.; Shi, G.; Lin, J.; Najmaei, S.; et al. *Nano Lett.* **2014**, *14*, 442-449.
- (66) Susarla, S.; Kutana, A.; Hachtel, J. A.; Kochat, V.; Apte, A.; Vajtai, R.; et al. *Adv. Mater.* **2017**, *29* (35), 1702457.
- (67) Zhang, J.; Jia, S.; Kholmanov, I.; Dong, L.; Er, D.; Chen, W.; et al. *ACS Nano* **2017**, *11* (8), 8192-8198.
- (68) Lu, A.-Y.; Zhu, H.; Xiao, J.; Chuu, C.-P.; Han, Y.; Chiu, M.-H.; et al. *Nat. Nanotechnol.* **2017**, *12*, 744-749.
- (69) Tsai, M.-L.; Li, M.-Y.; Retamal, J. R. D.; Lam, K.-T.; Lin, Y.-C.; Suenaga, K.; et al. *Adv. Mater.* **2017**, *29* (32), 1701168.
- (70) Li, M.-Y.; Shi, Y.; Cheng, C.-C.; Lu, L.-S.; Lin, Y.-C.; Tang, H.-L.; et al. *Science* **2015**, *349*, 524-528.
- (71) Yoo, Y.; Degregorio, Z. P.; Johns, J. E. *J. Am. Chem. Soc.* **2015**, *137*, 14281-14287.
- (72) Wang, Z.; Xie, Y.; Wang, H.; Wu, R.; Nan, T.; Zhan, Y.; et al. *Nanotechnology* **2017**, *28*, 325602.
- (73) Zhang, Z.; Chen, P.; Duan, X.; Zang, K.; Luo, J.; Duan X. *Science* **2017**, *3*, 6814, DOI: 10.1126/science.aan6814.
- (74) Mahjouri-Samani, M.; Lin, M.-W.; Wang, K.; Lupini, A. R.; Lee, J.; Basile, L.; et al. *Nat. Commun.* **2015**, *6*, 7749.
- (75) Li, H.; Li, P.; Huang, J.-K.; Li, M.-Y.; Yang, C.-W.; Shi, Y.; et al. *ACS Nano* **2016**, *10*, 10516-10523.
- (76) Yoo, Y.; DeGregorio, Z. P.; Su, Y.; Koester, S. J.; Johns, J. E. *Adv. Mater.* **2017**, *29*, 1605461.
- (77) Wickramaratne, D.; Zahid, F.; Lake, R. K. *J. Chem. Phys.* **2014**, *140*, 124710.
- (78) Jariwala, D.; Davoyan, A. R.; Tagliabue, G.; Sherrott, M. C.; Wong, J.; Atwater, H. A. *Nano Lett.* **2016**, *16*, 5482-5487.
- (79) Wong, J.; Jariwala, D.; Tagliabue, G.; Tat, K.; Davoyan, A. R.; Sherrott, M. C.; et al. *ACS Nano* **2017**, *11*, 7230-7240.
- (80) Chen, K.-S.; Xu, R.; Luu, N. S.; Secor, E. B.; Hamamoto, K.; Li, Q.; et al. *Nano Lett.* **2017**, *17*, 2539-2546.
- (81) Chen, K.-S.; Balla, I.; Luu, N. S.; Hersam, M. C. *ACS Ener. Lett.* **2017**, *2* (9), 2026-2034.
- (82) Zong, X.; Yan, H.; Wu, G.; Ma, G.; Wen, F.; Wang, L.; et al. *J. Am. Chem. Soc.* **2008**, *130*, 7176-7177.
- (83) Wang, T.; Liu, C.; Jiang, F.; Xu, Z.; Wang, X.; Li, X.; et al. *Phys. Chem. Chem. Phys.* **2017**, *19*, 17560-17567.
- (84) Jariwala, D.; Howell, S. L.; Chen, K.-S.; Kang, J.; Sangwan, V. K.; Filippone, S. A.; et al. *Nano Lett.* **2016**, *16*, 497-503.
- (85) Amani, M.; Lien, D.-H.; Kiriya, D.; Xiao, J.; Azcatl, A.; Noh, J.; et al. *Science* **2015**, *350*, 1065-1068.
- (86) Withers, F.; Del Pozo-Zamudio, O.; Mishchenko, A.; Rooney, A. P.; Gholinia, A.; Watanabe, K.; et al. *Nat. Mater.* **2015**, *14*, 301-306.
- (87) Jariwala, D.; Marks, T. J.; Hersam, M. C. *Nat. Mater.* **2017**, *16*, 170-181.

Inorganic 2D Materials

Powder and Dispersions

For a complete list of available materials, visit SigmaAldrich.com/nano.

Name	Form	Description	Cat. No.
Boron nitride	dispersion	0.1-0.5 mg/mL in H ₂ O, nanoplatelet	900710-10ML
	dispersion	20 mg/mL in H ₂ O, nanoplatelet	900417-50ML
	powder	lateral dimensions <1 micron, nanoplatelet	900405-500MG
	powder	lateral dimensions <5 μ, nanoplatelet	900408-1G
Molybdenum disulfide	dispersion	0.1-0.5 mg/mL in H ₂ O	900724-10ML

Crystals for Exfoliation

For a complete list of available materials, visit SigmaAldrich.com/chalcogenides.

Typical size: some variation in dimensions may occur with different batches.

Name	Composition	Dimension (L × W × H)	Purity (%)	Cat. No.
Molybdenum diselenide	MoSe ₂	0.5 cm × 0.5 cm × 0.1-0.15 mm	99.995	808660-1EA
Molybdenum disulfide	MoS ₂	0.5 cm × 0.5 cm × 0.1-0.15 mm	99.995	808652-1EA
Molybdenum telluride	MoTe ₂	0.5 cm × 0.5 cm × 0.2-0.3 mm	99.995	808814-1EA
Niobium diselenide	NbSe ₂	0.5 cm × 0.5 cm × 0.1-0.15 mm	99.995	808679-1EA
Rhenium disulfide	ReS ₂	0.5 cm × 0.5 cm × 0.1-0.15 mm	99.995	808695-1EA
Tantalum diselenide	TaSe ₂	0.5 cm × 0.5 cm × 0.1-0.15 mm	99.995	808733-1EA
Titanium disulfide	Ti ₂ S	0.5 cm × 0.5 cm × 0.1-0.15 mm	99.995	808717-1EA
Tungsten diselenide	Se ₂ W	0.5 cm × 0.5 cm × 0.1-0.15 mm	99.995	808822-1EA
Tungsten disulfide	W ₂ S	0.5 cm × 0.5 cm × 0.1-0.15 mm	99.995	808806-1EA

Graphene and Graphene Oxide

For a complete list of available materials, visit SigmaAldrich.com/graphene.

Graphene Powder

Name	Description	Cat. No.
Graphene	electrical conductivity >10 ³ S/m silane modified alkylamine functionalized	900561-500MG 900552-250MG 900551-250MG
Boron-doped graphene	Oxygen <7.5%	900526-250MG
Boron/Nitrogen co-doped graphene	Oxygen <7.5%	900535-250MG
Nitrogen-doped graphene	Carbon >80 wt. % Nitrogen >4 wt. % Carbon 85-95% Nitrogen 2.0-4.0% Oxygen <7.5%	900416-500MG 900527-250MG
Nitrogen/Phosphorus co-doped graphene	Carbon 85-95% Nitrogen 2.0-4.0% Oxygen <7.5% Phosphorus 1.0-3.0%	900531-250MG
Nitrogen/Sulfur co-doped graphene	Carbon 85-95% Nitrogen 2.0-4.0% Oxygen <7.5% Sulfur 2.0-4.0%	900530-250MG
Phosphorus-doped graphene	Carbon 85-95% Oxygen <7.5% Phosphorus 1.0-3.0%	900529-250MG
Sulfur-doped graphene	Carbon 85-95% Oxygen <7.5% Sulfur 2.0-4.0%	900528-250MG

Graphene Dispersion and Inks

Name	Form	Description	Cat. No.
Graphene dispersion	0.2 mg/mL in DMF	sheet resistance 2 kΩ/sq	900448-50ML
	1 mg/mL in DMF	sheet resistance 4.8 kΩ/sq	900450-5ML
	10 mg/mL in NMP	1-10 nm thick	803839-5ML
Graphene ink	liquid	with ethyl cellulose in cyclohexanone and terpineol, inkjet printable	793663-5ML
	liquid	with ethyl cellulose in terpineol, gravure printable	796115-10ML
	liquid	with ethyl cellulose in terpineol, screen printable	798983-10ML
Graphene ink in water	solids ~0.1 wt. % in water	inkjet printable	808288-5ML
	solids 7 wt. % in water	flexo/gravure/screen printable	805556-10ML
	solids 10 wt. % in water	screen printable	808261-10ML
Graphene/PEDOT:PSS hybrid ink	dispersion in DMF	1 mg/mL (electrochemically exfoliated graphene)	900442-50ML
3D printing graphene ink	viscous liquid	0.12-0.15 Ω-cm (as 3D-printed fibers, not ink, 200-400 μm diameter)	808156-5ML

Monolayer Graphene Films

Name	Description	Cat. No.
Monolayer graphene film	1 cm x 1 cm on copper foil	773697-4EA
	1 cm x 1 cm on copper foil, with PMMA coating	900443-4EA
	1 in. x 1 in. on copper foil	799009-1EA
	1 in. x 1 in. on copper foil, with PMMA coating	900445-1EA
	4 in. diameter on copper foil	900415-1EA
	1 cm x 1 cm on SiO ₂ /Si substrate	773700-4EA
	1 cm x 1 cm on quartz	773719-4EA
	1 in. x 1 in. on PET film	745863-1EA 745863-5EA
	2 in. x 2 in. on PET film	745871-1EA
	-	798177-1PK

Suspended monolayer graphene on TEM grid substrate (Quantifoil gold)

Graphene Nanoplatelets Powder

Surface Area (m ² /g)	Thickness (nm)	Particle Size (μm)	Cat. No.
surface area 50-80	15 (average)	5	900409-250G
	15 (average)	15	900410-250G
	15 (average)	25	900411-250G
surface area 120-150	6-8 (average)	5	900412-250G
	6-8 (average)	15	900420-250G
	6-8 (average)	25	900413-100G 900413-250G
surface area 300	a few nm	<2	900394-250G
surface area 500	a few nm	<2	900439-250G
surface area 750	a few nm	<2	900407-250G

Graphene Paper

Sheet Size (in.)	Thickness (μm)	Cat. No.
11.5 × 23.5	50	900449-1EA
11.5 × 23.5	120	900451-1EA
11.5 × 23.5	240	900452-1EA

Graphene Nanoribbons

Name	Purity (%)	Dimension (L × W)	BET Surface Area (m ² /g)	Cat. No.
Graphene nanoribbons, alkyl functionalized	≥85 carbon basis, TGA	2-15 μm × 40-250 nm	38	797766-500MG
Graphene nanoribbons	≥90.0 carbon basis, TGA	2-15 μm × 40-250 nm	48-58	797774-500MG

Graphene Oxide

Name	Form	Description	Cat. No.
Graphene oxide	film	4 cm (diameter) × 12-15 μm (thickness), non-conductive	798991-1EA
	powder	15-20 sheets 4-10% edge-oxidized	796034-1G
	powder or flakes	sheets	763713-250MG 763713-1G
	dispersion in H ₂ O	1 mg/mL, 15-20 sheets, 4-10% edge-oxidized	794341-50ML 794341-200ML
	dispersion in H ₂ O	2 mg/mL	763705-25ML 763705-100ML
	dispersion in H ₂ O	4 mg/mL	777676-50ML 777676-200ML
Graphene oxide nanocolloids	dispersion in H ₂ O	2 mg/mL	795534-50ML 795534-200M
Graphene oxide, ammonia functionalized	dispersion in H ₂ O	1 mg/mL	791520-25ML 791520-100ML

Reduced Graphene Oxide

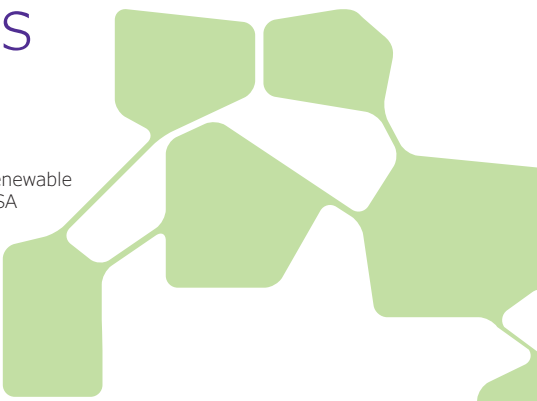
Description	Composition	Conductivity	Cat. No.
chemically reduced	Carbon >95 wt. % Nitrogen >5 wt. %	> 600 S/m	777684-250MG 777684-500MG
chemically reduced by hydrazine	Carbon >75% Nitrogen <5%	7111 S/m (pressed pallet)	805424-500MG 805424-1G
amine functionalized	Carbon >65 wt. % Nitrogen >5 wt. %	-	805432-500MG
octadecylamine functionalized	Carbon >78 wt. % Nitrogen >3 wt. %	6.36 S/m (pressed pellets)	805084-500MG
piperazine functionalized	Carbon >65 wt. % Nitrogen >5 wt. %	70.75 S/m (pressed pellets)	805440-500MG

Ultra-High Efficiency Perovskite-Perovskite Tandem Solar Cells

**Zhen Li and Kai Zhu***

Chemistry and Nanoscience Center, National Renewable Energy Laboratory, Golden, Colorado 80401, USA

*Email: Kai.Zhu@nrel.gov



Introduction

Next generation solar cells have the potential to achieve conversion efficiencies beyond the Shockley-Queisser (S-Q) limit while also significantly lowering production costs. To date, only multi-junction solar cells are able to achieve such high efficiencies. However, the current high-efficiency multi-junction cells require complex III-V-related epitaxial thin films and the use of an expensive single-crystal substrate, preventing low cost production of III-V multi-junction thin-film solar cells. In contrast to III-V films, polycrystalline thin-film solar cell technologies offer much lower production cost, but only moderate efficiencies. Fabricating highly efficient multi-junction polycrystalline thin-film solar cells remains a challenge.

Organic-inorganic halide perovskites have recently emerged as a new class of light absorbers for solar conversion applications. The power conversion efficiency of single-junction perovskite solar cells (PSCs) has already surpassed conventional polycrystalline thin-film solar cell technologies and is projected to compete with single-crystalline solar cells. Remarkably, these high-efficiency perovskite solar cells can be made from polycrystalline materials by either solution processing or vapor phase growth. Along with continued efforts to advance single-junction PSC technology, many research groups are developing perovskite-based tandem devices in order to move beyond the S-Q limit. With recent material innovations in low-bandgap (1.1–1.3 eV) and wide-bandgap (1.7–1.9 eV) perovskite absorbers and the transparent conductive interconnection layers, the use of polycrystalline halide perovskites for both the top and bottom cells in a tandem structure is a promising combination for the development of ultrahigh efficiency dual-junction thin-film tandem solar cells. In principle, such a device structure can be solution processed and promises to achieve efficiencies of >35% at one sun.

Here we review recent progress on perovskite-perovskite tandem solar cell development. In general, tandem solar cells can be constructed in two ways. In one approach, known as the four-terminal or 4-T tandem configuration, two independent solar cells are mechanically stacked one on top of the other. In the second configuration, referred to as two-terminal or 2-T tandem, the top and bottom cells are connected in series on a single substrate

to form a monolithic device. Regardless of the exact tandem structures, bandgap engineering of perovskite absorbers is essential for achieving efficient perovskite tandem devices. In a tandem structure, the wide bandgap cell is on the top to harvest high-energy photons and to allow low-energy photons to pass through for harvesting by the low-bandgap bottom cell. For a 2-T tandem device, assuming infinite absorber thickness for top and bottom sub-cells, the best bandgap combinations are around 1.7 and 1.1 eV for the top and bottom absorbers, respectively; the best efficiency in theory is 38.7%, surpassing the S-Q limit of a single-junction device (33.7%).¹ In actual devices, the thickness of the top cell can be adjusted to allow more photons to reach the bottom cell. Optical thinning can provide more material selection flexibility in tandem solar cells. For 4-T configurations, the current-matching restriction is removed and there is more freedom than in 2-T tandem solar cells to optimize the bandgap combination and gain higher efficiency.

Wide-Bandgap Perovskite Solar Cells

Wide-bandgap (~1.7–1.9 eV) perovskites are desirable for use as top sub-cells in tandem devices. Early stage development efforts centered on Br-I mixing of methylammonium lead halide perovskites (MAPbX_3). Noh et al. first demonstrated mixed-halide PSCs by replacing MAI with MABr in one-step precursor solutions.² By adjusting the Br-I mixing ratio, the bandgap of $\text{MAPbI}_{3-x}\text{Br}_x$ can be tuned from about 1.6 eV to 2.3 eV. Device performance also varies significantly with the Br-I mixing ratio. The open-circuit voltage (V_{oc}) and fill factor (FF) both increase with moderate Br ratios ($x < 0.2$), and the V_{oc} decreases abruptly with a Br ratio higher than 0.2. The use of Br is also found to strongly increase perovskite stability against humidity.

Other studies also demonstrated the ability to tune the bandgap with bromine, but did not focus on the optimization of bandgap for tandem applications. Zhao et al. first studied the optimization of mixed-halide PSCs targeted for tandem solar cells.³ They reported a general additive-assisted one-step solution growth to prepare MAPbI_2Br ($E_g = 1.8$ eV) thin films from a precursor containing the mixture of PbI_2 , MABr and MACl. The addition of MACl additive eliminates the formation

of dendrite structures, and results in compact and uniform thin films of MAPbI_2Br nanosheets. Planar PSCs with MAPbI_2Br nanosheets achieved a power conversion efficiency (PCE) of 10%. Bi et al. used solvent-assisted thermal annealing (often referred to as solvent annealing) to grow $\text{MAPbI}_{2.4}\text{Br}_{0.6}$ perovskite thin films with an increased grain size.⁴ A small amount of DMF vapor used during thermal annealing increased the average grain size from about 300 nm to 1000 nm, resulting in a $\text{MAPbI}_{2.4}\text{Br}_{0.6}$ based wide bandgap device with a PCE of 13.0%.

Shortly after the successful demonstration of wide-bandgap $\text{MAPb}(\text{I}_{1-x}\text{Br}_x)_3$ PSCs, Hoke et al. discovered the light-induced phase segregation phenomenon in I-Br mixed perovskites. It was found that once the Br ratio exceeds a threshold ($\sim 20\%$), I^- and Br^- ions start to segregate under light excitation, separated I and Br rich phases form. The phase segregation is recoverable after keeping the perovskite in the dark for a period of time. The light-induced low-bandgap phase acts as the carrier trapping defects and causing potential loss. The lower V_{OC} is normally a limiting factor to achieving higher efficiency in wide-bandgap PSCs. Interestingly, the A-site alloying can affect the phase stability of Br-I mixed wide bandgap perovskites (Figure 1). For example, McMeekin and Snaith et al. reported better phase stability of $\text{FA}_{0.83}\text{Cs}_{0.17}\text{Pb}(\text{I}_{0.6}\text{Br}_{0.4})_3$.⁵ Doping FA^+ with a suitable amount of Cs^+ reduces the Goldschmidt tolerance factor in the alloy materials and stabilizes the perovskite cubic

structures. The FA-Cs alloys also have a lower tendency for halide segregation under illumination; $\text{FA}_{0.83}\text{Cs}_{0.17}\text{Pb}(\text{I}_{0.6}\text{Br}_{0.4})_3$ PSCs with bandgaps of ~ 1.74 eV achieved a high V_{OC} of 1.2 V and PCE over 17%. Rehman et al. further characterized the phase stability of the mixed-cation, mixed-halide $\text{Cs}_y\text{FA}_{1-y}\text{Pb}(\text{I}_{0.6}\text{Br}_{0.4})_3$ perovskite materials⁶ and found a strong correlation between phase stability and crystallinity of the materials. X-ray diffraction showed minimal full width at half maximum (FWHM) of the perovskite peak with 20% Cs^+ ($y = 0.2$). Photoluminescence (PL) peak position of perovskite with 20% Cs^+ remained constant after continuous illumination for 30 minutes. The samples with lower (5%) or higher (60%) Cs^+ showed significant red-shifts in the PL spectra, indicating the formation of I-rich phase in the perovskites. In addition to better phase stability, samples with 20% Cs^+ also showed the highest mobility and longest PL lifetime within the studied composition range ($0 < y < 0.8$). Using a similar perovskite composition, Yu et al. fabricated 1.75 eV wide bandgap PSC with PCE of 17.7%. $\text{Pb}(\text{SCN})_2$ additive and solvent annealing were used to improve the grain size and crystallinity of the perovskite absorber, thus enabling high efficiency.⁷ Lin and Huang et al. adapted a triple A cation composition $(\text{FA}_{0.83}\text{MA}_{0.17})_{0.95}\text{Cs}_{0.05}\text{Pb}(\text{I}_{0.6}\text{Br}_{0.4})_3$ and fabricated p-i-n structure wide bandgap PSCs with PCE of 18.5%.⁸ The solar cell performance parameters and PCEs of several of, both mixed cation and anion, wide-bandgap PSCs are summarized in Table 1.

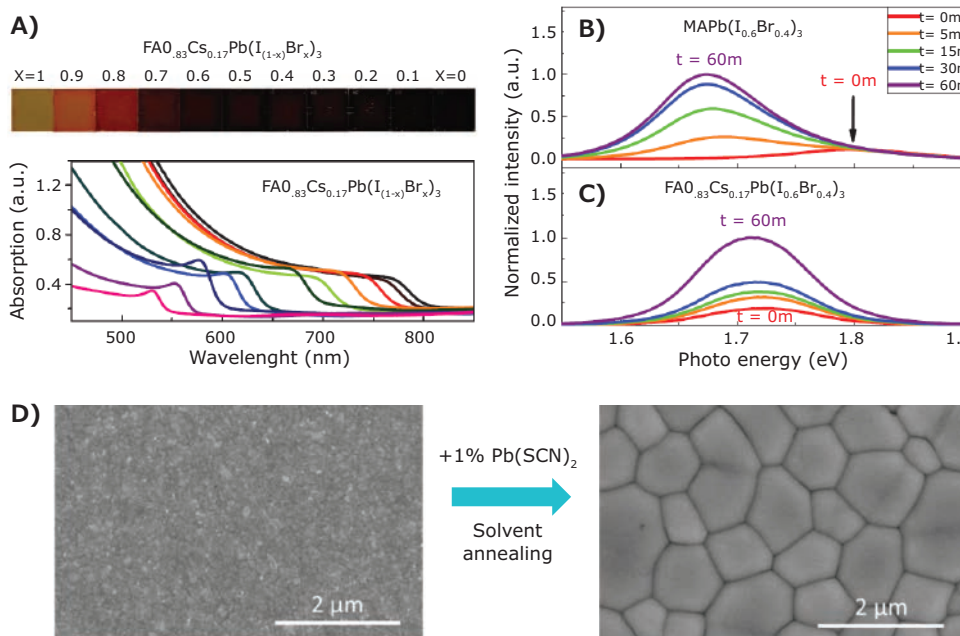


Figure 1. Wide bandgap perovskite materials. A) Optical images and UV-Vis spectra of $\text{FA}_{0.83}\text{Cs}_{0.17}\text{Pb}(\text{I}_{(1-x)}\text{Br}_x)_3$ mixed halide perovskite with different Br ratios. B) PL downshifting from $\text{MAPb}(\text{I}_{0.6}\text{Br}_{0.4})_3$ indicating I-rich phase formation after light soaking. C) Stable PL emission from phase stabilized $\text{FA}_{0.83}\text{Cs}_{0.17}\text{Pb}(\text{I}_{0.6}\text{Br}_{0.4})_3$. D) Morphology evolution of $\text{FA}_{0.83}\text{Cs}_{0.17}\text{Pb}(\text{I}_{0.6}\text{Br}_{0.4})_3$ with $\text{Pb}(\text{SCN})_2$ additive and solvent annealing.⁷ Reprinted with permission: A - C copyright 2016 American Association for the Advancement of Science (AAAS); D copyright 2017 American Chemical Society.

Table 1. Solar cell performance parameters and V_{oc} deficits of mixed-halide wide-bandgap PSCs.

Composition of Absorbers	Estimated Bandgap (eV)	V_{oc} (V)	J_{sc} (mA/cm ²)	FF	PCE (%) ^a	V_{oc} Deficit (V)	References
MAPb(I _{0.71} Br _{0.29}) ₃	1.71	0.95	14.2	0.69	9.29	0.76	2
MAPbI ₂ Br	1.8	1.09	14.8	0.62	10	0.71	3
MAPb(I _{0.8} Br _{0.2}) ₃	1.72	1.02	17.5	0.74	13.1	0.7	4
MAPb(I _{0.7} Br _{0.3}) ₃	1.75	1.01	18.2	0.69	12.3 ^b	0.74	9
MAPbI ₂ Br	1.77	1.08	15.3	0.65	10.1 ^b	0.69	10
FA _{0.83} Cs _{0.17} Pb(I _{0.6} Br _{0.4}) ₃	1.74	1.2	19.4	0.75	16.0 ^b	0.54	5
FA _{0.83} Cs _{0.17} Pb(I _{0.6} Br _{0.4}) ₃	1.75	1.25	18.5	0.79	16.6	0.5	7
(FA _{0.83} MA _{0.17}) _{0.95} Cs _{0.05} Pb(I _{0.6} Br _{0.4}) ₃	1.71	1.2	19.7	0.78	18.2 ^b	0.52	8
MAPb _{0.75} Sn _{0.25} (I _{0.4} Br _{0.6}) ₃	1.73	1.04	15.5	0.78	12.6	0.69	11

a: Stabilized power output (SPO) if available. b: SPO

Low-Bandgap Perovskite Solar Cells

Low-bandgap perovskite absorbers that can harvest photons in the infrared range are essential for constructing efficient perovskite-perovskite tandems. The most efficient way to reduce the bandgap of perovskite materials is by completely or partially replacing Pb²⁺ with Sn²⁺. The major challenge to developing Sn-based perovskites are the high carrier density and short carrier lifetime associated with the rapid oxidation of Sn²⁺ to Sn⁴⁺. Early studies focused on pure Sn (no Pb) based perovskites have fallen short on PCE and stability. Hao et al. used solution-processed lead-free MASnI₃ perovskite as a light harvester in solar cells and attained a PCE of 5.23%.¹² Incorporation of Br leads to an improvement in the PCE to 5.73% using a MASnIBr₂ absorber. Noel et al. showed that the recombination rate in MASnI₃ is extremely fast with a PL lifetime of ~200 ps and a high hole doping density (~10¹⁸ cm⁻³) based on terahertz conductivity measurement.¹³ Significant efforts have been devoted to reducing the carrier density by suppressing the oxidation of Sn²⁺. Kumar et al. discovered that doping with SnF₂ can significantly suppress the formation of Sn⁴⁺ defects in the solution-processed CsSnI₃ thin films.¹⁴ They found that including 20% SnF₂ additive in CsSnI₃ reduces the carrier density and film conductivity by 2 orders of magnitude. The same strategy was applied in FASnI₃-based solar cells with a similar effect.¹⁵ Lee et al. later showed that adding SnF₂ with pyrazine can further improve film quality by removing plate-like SnF₂ segregation, leading to improved device performance.¹⁶

Recently, some of the most significant breakthroughs in low-bandgap perovskites have been reported by groups developing Sn-Pb alloy based absorbers in an inverted device structure

(i.e., p-i-n planar heterojunction structure). Yang et al. demonstrated MA_{0.5}FA_{0.5}Pb_{0.75}Sn_{0.25}I₃ based planar heterojunction solar cells with a bandgap of 1.33 eV and a PCE of 14.19%.¹⁷ Interestingly, these solar cells showed significantly improved stability, retaining 80% of the initial PCE after 12 days of storage in ambient air. Eperon et al. fabricated FA_{0.75}Cs_{0.25}Sn_{0.5}Pb_{0.5}I₃ PSCs with a more suitable bandgap (1.2 eV) for tandem applications.¹⁸ The best solar cell yielded a PCE of 14.1%. Liao et al. also fabricated 1.2 eV PSCs with composition of (FASnI₃)_{0.6}(MAPbI₃)_{0.4} (**Figure 2**).¹⁹ The solar cell showed an average PCE of 14.39% with a stabilized PCE of 14.8%. These authors further found the grain size of the perovskite thin film can be increased with the film thickness, improving the efficiency to 17.6% with a thicker perovskite layer (17.01% with certification).²⁰ Perovskite absorbers with large grains and better crystallinity yielded a longer carrier lifetime and provided better cell performance. The solar cell performance parameters and PCEs of several, of, both mixed cation and anion, low-bandgap PSCs are summarized in **Table 2**. It is worth noting that several factors contributed concurrently to the rapid and exciting progress on the low-bandgap perovskite development: (1) The Sn-Pb alloys have lower bandgap and absorb in a wider range of the spectrum compared to pure Sn based perovskites; this is caused by the large bowing effect in bandgap composition correlations.²¹⁻²² (2) The oxidation tendency of Sn²⁺ is suppressed with alloying Pb²⁺ cations. (3) An inverted planar heterojunction structure does not need an oxidation process for the HTM, which alleviates the unnecessary reaction between oxidative HTM dopants and Sn²⁺ cations.

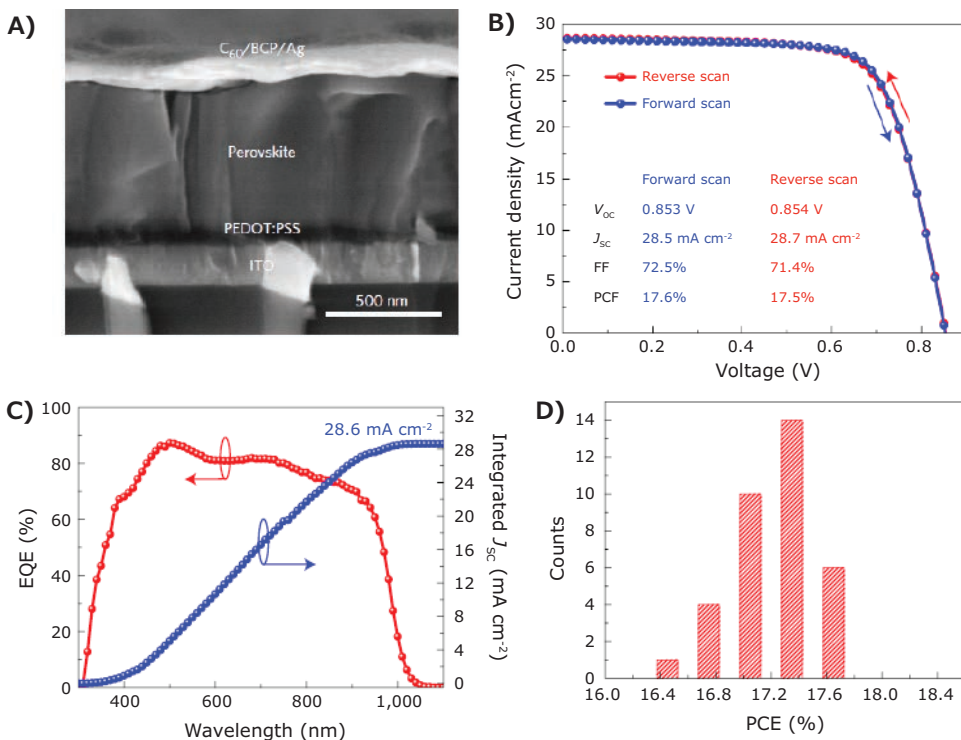


Figure 2. (FASnI₃)_{0.6}(MAPbI₃)_{0.4} low bandgap solar cell. **A)** Cross section SEM of the solar cell device; **B)** J-V curves under one sun illumination; **C)** EQE and integrated JSC; **D)** Histograms of the PCEs from 35 solar cell devices.²⁰ Reprinted with permission, copyright 2017 Macmillan Publishers Limited.

Table 2. Solar cell performance parameters of low-bandgap PSCs.

Composition of Absorbers	Estimated Bandgap (eV)	V _{oc} (V)	J _{sc} (mA/cm ²)	FF	PCE (%)	References
MASnI ₃	1.3	0.68	16.3	0.48	5.23	12
CsSnI ₃	1.3	0.24	22.7	0.37	2.02	14
FASnI ₃	1.41	0.24	24.4	0.36	2.1	15
FASnI ₃	1.41	0.32	23.7	0.63	4.8	16
MAPb _{0.5} Sn _{0.5} I ₃	1.18	0.32	19.9	0.37	2.37	23
MAPb _{0.75} Sn _{0.25} I ₃	1.35	0.82	22.4	0.78	14.3	17
FA _{0.75} Cs _{0.25} Sn _{0.5} Pb _{0.5} I ₃	1.2	0.74	26.7	0.71	14.1	18
(FASnI ₃) _{0.6} (MAPbI ₃) _{0.4}	1.2	0.8	26.9	0.71	15.1	19
(FASnI ₃) _{0.6} (MAPbI ₃) _{0.4}	1.25	0.85	28.7	0.71	17.5	20

Perovskite-Perovskite Tandem Solar Cells

The success of tuning the bandgap of perovskite materials over a wide range of the solar spectrum has enabled the development of perovskite-perovskite tandem solar cells. The tandem concept is not only attractive for obtaining ultra-high efficiency as with all other tandem cell configurations, it also can significantly reduce the fabrication cost of tandem solar cells because both sub-cells can be fabricated with solution processes. To date, all perovskite based tandem solar cells have been demonstrated with both 2-T and 4-T configurations from

either solution processing or vapor phase deposition (Figure 3). Using a non-ideal combination of perovskite absorbers, Li et al. demonstrated a 4-T perovskite-perovskite tandem solar cell with 2.3 eV MAPbBr₃/carbon nanotubes top cell and 1.55 eV MAPbI₃ bottom cell.²⁴ The total efficiency of this tandem device was only 9.5%, which is lower than the bottom MAPbI₃ cell alone. Later in the same year, Heo et al. fabricated a series-connected 2-T MAPbBr₃-MAPbI₃ tandem solar cell using a lamination process.²⁵ In order to laminate the top and bottom perovskite solar cells together, a thick (~2 mm) hole transporting material (e.g., PTAA or P3HT) was used. Although the device showed a promising high V_{oc} of 2.25 V, the poor FF (~0.56) and inappropriate light

absorption limits the tandem PCE to about 10.4%. The poor FF suggested the lamination process did not form a conformal and continuous contact between the top and bottom sub-cells. With the recent success fabricating stable Sn-Pb based low-bandgap perovskites, Yang et al. demonstrated an all-perovskite 4-T tandem solar cell with a total PCE of 19.08%. In this study, the top cell is unfortunately based on a 1.55 eV MAPbI_3 absorber, which significantly overlaps in light absorption with the 1.33 eV bottom cell.¹⁷

To fully realize the potential of perovskite-perovskite based tandem solar cells, the bandgaps of the top and bottom sub-cells should be paired properly. Toward this end, Eperon et al. achieved a breakthrough on perovskite-perovskite tandem devices using ideally matched bandgaps.¹⁸ In this study, a top cell with a bandgap of ~1.8 eV was fabricated using $\text{FA}_{0.83}\text{Cs}_{0.17}\text{Pb}(\text{I}_{0.5}\text{Br}_{0.5})_3$. The mixing of FA and Cs dramatically improved the stability of perovskites even with the high Br ratio as previously discussed. The bottom cell used a new composition based on Sn-Pb alloyed perovskite with a low bandgap of about 1.2 eV. One challenge to fabricating perovskite-on-perovskite tandem devices is avoiding damage to the bottom perovskite cell during deposition of the top perovskite cell. In an ideal situation, the solvent used to deposit the top cell stack should be orthogonal to the bottom cell stack. However,

this is impossible at the moment since the standard perovskite compositions can only be dissolved in a few common solvents with sufficient solubility. To address this issue, the authors demonstrated that coating a 200 nm indium tin oxide (ITO) layer on top of the 1.8 eV bottom perovskite cell can effectively protect the underlying bottom cell from solvent damage. This compact ITO layer also serves as an effective recombination layer to electronically connect the top and bottom sub-cells. The 2-T tandem device with the ITO recombination layer achieved a remarkable stabilized PCE of 17.0% with a V_{oc} of 1.66 V and J_{sc} of 14.5 mA/cm². They further optimized the bandgap of the top cell to construct a 4-T tandem cell by coupling a 1.6 eV $\text{FA}_{0.83}\text{Cs}_{0.17}\text{Pb}(\text{I}_{0.83}\text{Br}_{0.17})_3$ top cell with the 1.2 eV bottom cell with an total power conversion efficiency of 20.3%.

Another way to avoid damaging the bottom perovskite cell during tandem cell fabrication is to use vapor phase deposition to grow the top perovskite sub-cell. In a recent study, Forgács et al. presented efficient monolithic tandem solar cells based on two perovskite absorbers with different and complementary bandgaps: a wide bandgap perovskite with ~2 eV $\text{Cs}_{0.15}\text{FA}_{0.85}\text{Pb}(\text{I}_{0.3}\text{Br}_{0.7})_3$ for the front sub-cell and standard ~1.6 eV MAPbI_3 for the rear sub-cell.²⁶ To build this device stack, the wide bandgap perovskite layer is first deposited by solution processing and all the remaining materials needed for

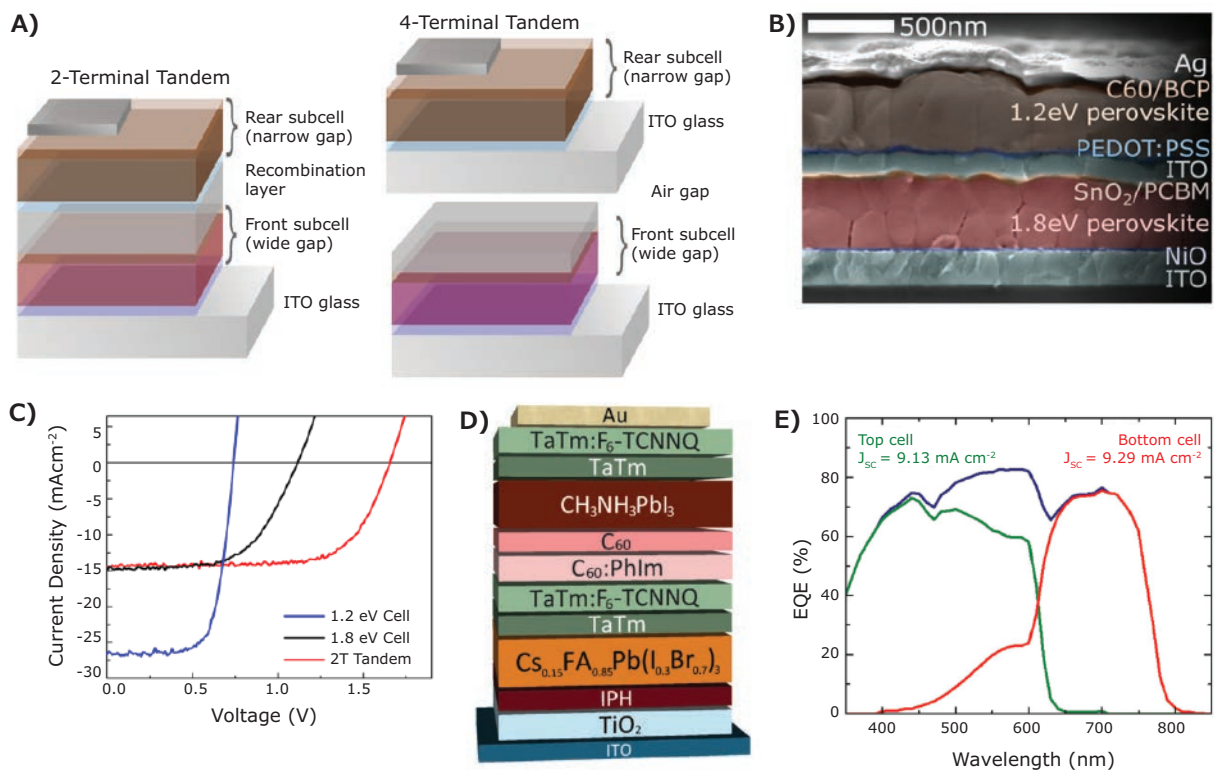


Figure 3. Perovskite-perovskite tandem solar cells. **A)** Schematics of 2-T and 4-T tandem solar cells. **B)** Cross-section SEM of a 2-T perovskite-perovskite tandem device. **C)** J-V curves of 2-T tandem cell.¹⁸ **D)** Schematics of a 2-T perovskite-perovskite tandem cell fabricated with vapor phase deposition. **E)** External quantum efficiency (EQE) of the top, bottom, and tandem cells.²⁶ Reprinted with permission: A – C copyright 2016 AAAS; D – E copyright 2017 Wiley-VCH.

the tandem devices are deposited using thermal evaporation. Instead of using a transparent conducting oxide (TCO) based transparent interconnection scheme, a p-n junction based on doped organic semiconductors consisting of p-doped TaTm:F₆-TCNNQ (40 nm)/n-doped C₆₀:PhIm (40 nm) is used as an effective recombination layer to connect the two perovskite sub-cells. Despite the non-ideal bandgaps in the tandem device a record efficiency of 18% was achieved for a monolithic 2-T tandem cell. The photovoltaic performance of all-perovskite tandem solar cells with different configurations are summarized in **Table 3**.

At present, the record efficiency of perovskite-perovskite 4-T tandem solar cell is 21.2% with a stabilized efficiency of 21.0% as demonstrated by Zhao et al.²⁰ However, the wide bandgap PSC only used a ~1.6 eV $\text{FA}_{0.3}\text{MA}_{0.7}\text{PbI}_3$ perovskite absorber. As a result, the wide gap cell only contributed about 3% efficiency to the tandem device. In this tandem configuration, the top cell has a regular n-i-p configuration of FTO/SnO₂/C₆₀-SAM/FA_{0.3}MA_{0.7}PbI₃/Spiro-MeTAD/MoO_x(10 nm)/Au(8.5 nm)/MoO_x(10 nm). The first 10 nm MoO_x layer acts as both hole buffer layer and wetting layer for Au deposition. A MoO_x wetting layer changes the growth mechanism and allows the deposition of ultrathin Au of 8.5 nm without the formation of isolated islands. The second MoO_x layer is employed to form a dielectric-metal-dielectric stack to tune the light dispersion characteristics of the semi-transparent electrode, enhancing the total transparency of the top cell. It is worth noting the PCE of the best 4-T tandem cell is still partially

limited by the performance of the top cell as the bandgap of perovskite absorber is not wide enough to optimally match with the bottom cell. Further PCE improvement is expected when efficient top cells with wider bandgaps (\sim 1.7-1.9 eV) and better transparent conducting electrodes are developed.

Conclusions and Outlook

In summary, organic-inorganic halide perovskites have shown great potential for ultrahigh efficiency tandem thin-film solar cells. Several breakthroughs have been made recently on single-junction solar cells based on low-bandgap as well as wide-bandgap perovskite absorbers. These advancements along with the successful demonstration of transparent top contact and interconnection layers have enabled demonstration of 18% 2-T and 21% 4-T perovskite-perovskite tandem cells. These efficiencies were obtained despite non-ideal combinations of bandgaps of the two perovskite sub-cells. Although these studies present encouraging results indicating the perovskite-perovskite tandem approach is viable, they further identify the areas of research for further enhancing the performance of perovskite solar cells with a tandem configuration.

Further studies and advances should be continuously made in the development of low-bandgap (~1.1–1.3 eV) and wide-bandgap (~1.7–1.9 eV) as well as the interconnection layer to electronically and optically couple the top and bottom perovskite sub-cells as follows: (1) For low-bandgap perovskites, research should be focused on increasing carrier lifetime and reducing defect densities for Sn-Pb based perovskites. The EQE in the

Table 3. Photovoltaic performance of all-pervoskite tandem solar cells with different sub-cell configurations

near-IR wavelength range (about 700 to 900 nm and beyond) is currently not ideal. Increasing charge transport length without significant recombination loss is expected to increase EQE in the long wavelength. Reducing charge recombination (at interface, bulk, and/or grain boundary) can compensate to some degree for the loss of photocurrent when monolithically stacking two subcells. Moreover, reducing perovskite process temperature can help avoid degradation of the underlying sub-cells. (2) For wide-bandgap perovskites, the development of ~1.7 eV bandgap materials has been quite successful in recent years. Thus, more effort should be directed toward a bandgap range of about 1.8–1.9 eV to allow more flexibility to pair top and bottom subcells. The voltage loss relative to the bandgap is still quite large for wide-bandgap PSCs; significant effort is required to reduce the V_{OC} deficit to improve the power output of tandem devices. (3) An effective interconnection layer is a transparent electrode with both good transparency (>90 transmission) and electrical conductivity (10–100 Ω/sq). Energy-level matching, robust adhesion and good chemical stability are key considerations of the transparent electrodes. In addition, this multifunction layer also needs to be robust enough to avoid damaging the underlying perovskite cell during deposition of the top perovskite cell stack. With advances in these areas, it is expected that perovskite-based tandem solar cells will be realized in the near future with efficiencies approaching or exceeding the S-Q limit.

Acknowledgements

We acknowledge the support by the hybrid perovskite solar cell program of the National Center for Photovoltaics funded by the U.S. Department of Energy, Office of Energy Efficiency and Renewable Energy, Solar Energy Technologies Office. The work at the National Renewable Energy Laboratory is supported by the U.S. Department of Energy under Contract No. DE-AC36-08-GO28308.

References

- (1) Kurtz, S. R.; Faine, P.; Olson, J. M. *J. Appl. Phys.* **1990**, *68* (4), 1890-1895.
- (2) Noh, J. H.; Im, S. H.; Heo, J. H.; Mandal, T. N.; Seok, S. I. *Nano Lett.* **2013**, *13* (4), 1764-1769.
- (3) Zhao, Y.; Zhu, K. *J. Am. Chem. Soc.* **2014**, *136* (35), 12241-12244.
- (4) Bi, C.; Yuan, Y.; Fang, Y.; Huang, J. *Adv. Energy Mater.* **2015**, *5* (6), 1401616.
- (5) McMeekin, D. P.; Sadoughi, G.; Rehman, W.; Eperon, G. E.; Saliba, M.; Snaith, H. J.; et al. *Science* **2016**, *351* (6269), 151-155.
- (6) Rehman, W.; McMeekin, D. P.; Patel, J. B.; Milot, R. L.; Johnston, M. B.; Snaith, H. J.; Herz, L. M. *Energy Environ. Sci.* **2017**, *10*, 361-369.
- (7) Yu, Y.; Wang, C.; Grice, C. R.; Shrestha, N.; Zhao, D.; Liao, W.; et al. *ACS Energy Lett.* **2017**, *2* (5), 1177-1182.
- (8) Lin, Y.; Chen, B.; Zhao, F.; Zheng, X.; Deng, Y.; Shao, Y.; Fang, Y.; Bai, Y.; Wang, C.; Huang, J. *Adv. Mater.* **2017**, *29* (26), 1700607.
- (9) Zhu, W.; Bao, C.; Li, F.; Zhou, X.; Yang, J.; Yu, T.; Zou, Z. *Chem. Commun.* **2016**, *52* (2), 304-307.
- (10) Zhou, Y.; Yang, M.; Game, O. S.; Wu, W.; Kwun, J.; Strauss, M. A.; Yan, Y.; Huang, J.; Zhu, K.; Padture, N. P. *ACS Appl. Mater. Interfaces* **2016**, *8* (3), 2232-2237.
- (11) Yang, Z.; Rajagopal, A.; Jo, S. B.; Chueh, C. C.; Williams, S.; Huang, C. C.; Katahara, J. K.; Hillhouse, H. W.; Jen, A. K. *Nano Lett.* **2016**, *16* (12), 7739-7747.
- (12) Hao, F.; Stoumpos, C. C.; Cao, D. H.; Chang, R. P. H.; Kanatzidis, M. G. *Nat. Photon.* **2014**, *8* (6), 489-494.
- (13) Noel, N. K.; Stranks, S. D.; Abate, A.; Wehrenfennig, C.; Guarnera, S.; Snaith, H. J.; et al. *Energy Environ. Sci.* **2014**, *7* (9), 3061-3068.
- (14) Kumar, M. H.; Dharani, S.; Leong, W. L.; Graetzel, M.; Mhaisalkar, S. G.; Mathews, N.; et al. *Adv. Mater.* **2014**, *26* (41), 7122-7127.
- (15) Koh, T. M.; Krishnamoorthy, T.; Yantara, N.; Shi, C.; Leong, W. L.; Boix, P. P.; Grimsdale, A. C.; Mhaisalkar, S. G.; Mathews, N. *J. Mater. Chem. A* **2015**, *3* (29), 14996-15000.
- (16) Lee, S. J.; Shin, S. S.; Kim, Y. C.; Kim, D.; Ahn, T. K.; Noh, J. H.; Seo, J.; Seok, S. I. *J. Am. Chem. Soc.* **2016**, *138* (12), 3974-3977.
- (17) Yang, Z.; Rajagopal, A.; Chueh, C. C.; Jo, S. B.; Liu, B.; Zhao, T.; Jen, A. K. *Adv. Mater.* **2016**, *28* (40), 8990-8997.
- (18) Eperon, G. E.; Leijtens, T.; Bush, K. A.; Prasanna, R.; Green, T.; Snaith, H. J.; et al. *Science* **2016**, *354* (6314):861-865.
- (19) Liao, W.; Zhao, D.; Yu, Y.; Shrestha, N.; Ghimire, K.; Grice, C. R.; et al. *Nat. Energy* **2016**, *1* (38), 12360-12363.
- (20) Zhao, D.; Yu, Y.; Wang, C.; Liao, W.; Shrestha, N.; Grice, C. R.; et al. *Nat. Energy* **2017**, *2*, 17018.
- (21) Umari, P.; Mosconi, E.; De Angelis, F. *Sci. Rep.* **2014**, *4*, 4467.
- (22) Hao, F.; Stoumpos, C. C.; Chang, R. P.; Kanatzidis, M. G. *J. Am. Chem. Soc.* **2014**, *136* (22), 8094-12369.
- (23) Ogomi, Y.; Morita, A.; Tsukamoto, S.; Saitho, T.; Fujikawa, N.; Shen, Q.; Toyoda, T.; Yoshino, K.; Pandey, S. S.; Ma, T.; Hayase, S. *J. Phys. Chem. Lett.* **2014**, *5* (6), 1004-1011.
- (24) Li, Z.; Boix, P. P.; Xing, G.; Fu, K.; Kulkarni, S. A.; Batabyal, S. K.; Xu, W.; Cao, A.; Sun, T. C.; Mathews, N.; Wong, L. H. *Nanoscale* **2016**, *8* (12), 6352-6360.
- (25) Heo, J. H.; Im, S. H. *Adv. Mater.* **2016**, *28* (25), 5121-5125.
- (26) Forgács, D.; Gil-Escríg, L.; Pérez-Del-Rey, D.; Momblona, C.; Werner, J.; Niesen, B.; Ballif, C.; Sessolo, M.; Bolink, H. J. *Adv. Energy Mater.* **2017**, *7* (8), 1602121.
- (27) Rajagopal, A.; Yang, Z.; Jo, S. B.; Braly, I. L.; Liang, P.-W.; Hillhouse, H. W.; Jen, A. K. Y. *Adv. Mater.* **2017**, *29* (34), 1702140.

Precursors for Organometallic Perovskites

For a complete list of available materials, visit SigmaAldrich.com/perovskites.

Organohalide Materials

Name	Composition	Form	Purity (%)	Cat. No.
Acetamidinium iodide	$\text{C}_2\text{H}_7\text{IN}_2$	powder	98	805971-5G 805971-25G
Benzylammonium bromide	$\text{C}_6\text{H}_{10}\text{BrN}$	powder or crystals	≥98	900885-5G 900885-25G
Benzylammonium iodide	$\text{C}_6\text{H}_{10}\text{IN}$	powder	98	806196-5G 806196-25G
n-Butylammonium bromide	$\text{C}_4\text{H}_{12}\text{BrN}$	powder	≥98	900817-10G 900817-25G
t-Butylammonium bromide	$\text{C}_4\text{H}_{12}\text{BrN}$	powder	≥98	900827-10G 900827-25G

Name	Composition	Form	Purity (%)	Cat. No.
<i>i</i> -Butylammonium bromide	C ₄ H ₁₂ BrN	powder	≥98	900869-10G 900869-25G
<i>n</i> -Butylammonium iodide	C ₄ H ₁₂ IN	powder	98	805874-5G 805874-25G
<i>t</i> -Butylammonium iodide	C ₄ H ₁₂ IN	powder	98	806102-5G 806102-25G
<i>i</i> -Butylammonium iodide	C ₄ H ₁₂ IN	powder	98	805866-5G 805866-25G
Diethylammonium bromide	C ₄ H ₁₁ N · HBr	powder	≥98	900840-10G 900840-25G
Diethylammonium iodide	C ₄ H ₁₂ IN	powder	98	806188-5G 806188-25G
Dimethylammonium bromide	C ₂ H ₈ BrN	powder	≥98	900872-25G 900872-10G
Dimethylammonium iodide	C ₂ H ₈ IN	powder	98	805831-5G 805831-25G
Ethane-1,2-diammonium bromide	C ₂ H ₁₀ Br ₂ N ₂	powder	≥98	900833-5G 900833-25G
Ethane-1,2-diammonium iodide	C ₂ H ₈ N ₂ · 2HI	powder	≥98	900852-5G 900852-25G
Formamidinium bromide	CH ₅ BrN ₂	powder	≥98	900835-25G 900835-5G
	CH ₅ BrN ₂	crystals	≥99	901437-10G
Formamidinium iodide	CH ₅ IN ₂	powder	≥99	901436-10G
	CH ₅ IN ₂	powder	≥98, H-NMR	806048-5G 806048-25G
Guanidinium bromide	CH ₆ BrN ₃	powder	≥98	900839-10G 900839-25G
	CH ₆ BrN ₃	powder	≥99	901452-10G
Guanidinium iodide	CH ₆ IN ₃	powder	≥99	806056-5G 806056-25G
	CH ₆ IN ₃	powder	≥99	901450-10G
Imidazolium bromide	C ₃ H ₄ N ₂ · HBr	powder	≥98	900821-5G 900821-25G
Imidazolium iodide	C ₃ H ₅ IN ₂	powder	98	805963-5G 805963-25G
Methylammonium bromide	CH ₃ BrN	powder	98	806498-25G
	CH ₃ BrN	powder	≥99	901435-10G
	CH ₃ NH ₂ · HBr	powder	98	793507-5G
Methylammonium bromide solution	CH ₃ NH ₂ · HBr	0.18 M in 2-propanol	-	808407-50ML
Methylammonium chlorodiodoplumbate(II) precursor solution	CH ₃ NClI ₂ Pb	liquid	-	809039-25G
Methylammonium iodide	CH ₃ NH ₂ · HI	powder	98	793493-5G
	CH ₃ NH ₂ · HI	powder	-	806390-25G
	CH ₃ IN	crystals	≥99	901434-10G
Methylammonium triiodoplumbate(II) precursor solution	[CH ₃ NH ₃] ⁺ [PbI ₃] ⁻	40 wt. % in DMF	-	793833-5ML
Phenethylammonium bromide	C ₈ H ₁₂ BrN	crystals	≥98	900829-10G 900829-25G
Phenethylammonium iodide	C ₈ H ₁₂ IN	powder	98	805904-25G
Phenylammonium bromide	C ₆ H ₈ BrN	powder or crystals	≥98	900828-10G 900828-25G
Phenylammonium iodide	C ₆ H ₈ IN	powder	≥98, H-NMR	805912-5G 805912-25G
Propane-1,3-diammonium bromide	C ₃ H ₁₂ Br ₂ N ₂	powder	≥98	900834-5G 900834-25G
Propane-1,3-diammonium iodide	C ₃ H ₁₂ I ₂ N ₂	powder	≥98	900832-5G 900832-25G
<i>n</i> -Propylammonium bromide	C ₃ H ₁₀ BrN	flakes	≥98	900819-10G 900819-25G
<i>i</i> -Propylammonium bromide	C ₃ H ₁₀ BrN	crystals	≥98	900816-25G 900816-10G
<i>n</i> -Propylammonium iodide	C ₃ H ₁₀ IN	powder	-	805858-5G 805858-25G
<i>i</i> -Propylammonium iodide	C ₃ H ₁₀ IN	powder	98	805882-5G 805882-25G

Lead Halides

Name	Composition	Form	Purity (%)	Cat. No.
Lead(II) bromide	PbBr ₂	powder	99.999 trace metals basis	398853-5G
	PbBr ₂	powder	≥98	211141-100G 211141-500G
Lead(II) chloride	PbCl ₂	beads	99.999	449865-5G
	PbCl ₂	powder and chunks	99.999 trace metals basis	203572-10G 203572-50G
	PbCl ₂	powder	98	268690-5G 268690-250G 268690-1KG
Lead(II) iodide	PbI ₂	beads	99.999 trace metals basis	554359-5G
	PbI ₂	solid	99.999 trace metals basis	203602-50G
	PbI ₂	powder	99	211168-50G
Lead(II) iodide solution	PbI ₂	0.55 M in DMF	-	795550-10ML

Titania Nanomaterials for SupportFor a complete list of available materials, visit SigmaAldrich.com/titaniasupport.

Name	Description	Purity (%)	Form	Cat. No.
Titanium	particle size <100 nm	98.5 trace metals basis	dispersion nanoparticles	513415-5G
Titanium dioxide	particle size 18 - 20 nm (BET) spec. surface area 60-70 m ² /g (BET)	>95 (anatase(XRD))	paste (nanocrystalline colloid)	798525-25G
	particle size 18 - 20 nm (BET) spec. surface area 75-90 m ² /g (BET)	-	paste (nanocrystalline colloid)	798509-25G
	particle size 22 nm & >150 nm (BET), spec. surface area 50-60 m ² /g (BET)	-	paste (nanocrystalline colloid)	798517-25G
	particle size 22 - 25 nm (BET) spec. surface area 65-75 m ² /g (BET)	>95 (anatase (XRD))	paste (nanocrystalline colloid)	798495-25G
	average diameter 25 nm	-	nanotubes powder	799289-500MG
Titanium(IV) oxide	primary particle size 21 nm (TEM), surface area 35-65 m ² /g (BET)	≥99.5 trace metals basis	nanopowder	718467-100G
Titanium(IV) oxide, anatase	particle size <25 nm, spec. surface area 45-55 m ² /g	99.7 trace metals basis	nanopowder	637254-50G 637254-100G 637254-500G
Titanium(IV) oxide, rutile	particle size <100 nm, spec. surface area 50 m ² /g	99.5 trace metals basis	nanopowder	637262-25G 637262-100G
Titanium(IV) oxide, mixture of rutile and anatase	particle size <100 nm (BET) particle size <50 nm (XRD)	99.5 trace metals basis	nanopowder	634662-25G 634662-100G
	particle size <250 nm (DLS), BET surf. area 50 m ² /g (BET surface area of starting nanopowder)	99.9 trace metals basis	nanoparticle paste	700355-25G
	particle size <150 nm (volume distribution, DLS)	99.5 trace metals basis	dispersion nanoparticles	700347-25G 700347-100G
	particle size <100 nm	99.9 trace metals basis	dispersion nanoparticles	700339-100G

Hole Transport Materials (HTM)For a complete list of available materials, visit SigmaAldrich.com/htm.

Name	Structure	Purity (%)/Molecular Weight	Cat. No.
Spiro-MeOTAD		99, HPLC	792071-1G 792071-5G
PTAA		average M _n 7,000-10,000 (GPC)	702471-100MG 702471-1G

Name	Structure	Purity (%) / Molecular Weight	Cat. No.
Poly(3-hexylthiophene-2,5-diyl)		average M _w 20,000-45,000	900563-5G 900563-1G
		average M _w 50,000-75,000	900550-1G 900550-5G
		average M _w 85,000-100,000	900549-1G
		average M _w 50,000-100,000	445703-1G

Hole Conductor Cobalt Dopants

For a complete list of available materials, visit SigmaAldrich.com/hccobalt.

Name	Structure	Purity (%)	Cat. No.
FK 102 Co(II) PF ₆ salt		98	805238-5G
FK 102 Co(II) TFSI salt		98	805246-5G
FK 102 Co(III) PF ₆ salt		>98	805254-5G
FK 102 Co(III) TFSI salt		98	805203-5G
FK 209 Co(II) PF ₆ salt		98	805378-5G
FK 209 Co(II) TFSI salt		98	805386-5G
FK 209 Co(III) PF ₆ salt		98	805408-5G

Name	Structure	Purity (%)	Cat. No.
FK 209 Co(III) TFSI salt		98	805394-5G
FK 269 Co(II) PF ₆ salt		98	805548-5G
FK 269 Co(II) TFSI salt		98	805815-5G
FK 269 Co(III) PF ₆ salt		98	805521-5G
FK 269 Co(III) TFSI salt		98	805807-5G

Fluorine-Doped Tin Oxide (FTO) Coated Glass

For a complete list of available materials, visit SigmaAldrich.com/fto.

Surface Resistivity (Ω/sq)	Haze (%)	Transmittance (% visible)	L × W × D (mm)	Cat. No.
~7	5	80-82	50 × 50 × 2.2	735140-5EA
			100 × 100 × 2.3	735159-5EA
			300 × 300 × 2	735167-1EA
~8	12	80-81.5	50 × 50 × 3	735175-5EA
			100 × 100 × 3	735183-5EA
			300 × 300 × 3.2	735191-1EA
~10	1	83	50 × 50 × 3	735205-5EA
			100 × 100 × 3	735213-5EA
			300 × 300 × 3	735221-1EA
~13	≤ 0.74	82-84.5	50 × 50 × 2.2	735248-5EA
			100 × 100 × 2.2	735256-5EA
			300 × 300 × 2.3	735264-1EA

Synthesis of Halide Perovskite Quantum Dots for Display Applications



Qingchao Zhou, Feng Zhang, and Haizheng Zhong*

School of Materials Science & Engineering, Beijing Institute of Technology, Beijing, 100081, China

*Email: hzzhong@bit.edu.cn

Introduction

Colloidal quantum dots (QDs) are solution-processable luminescent materials that can produce high-quality color in light emitting diodes (LEDs). These LEDs are essential components of advanced solid-state lighting and flat panel displays.¹ After more than 30 years of development, CdSe and InP based QDs are now emerging as “upstarts” in commercial liquid crystal display (LCD) TVs from TCL (XESS X1) and Samsung (SUHD), as well as prototype EL display demos from BOE (SID 2017). However, large-scale commercialization is still limited by high cost and limited reliability. This performance gap has helped to generate intense interest in finding new approaches. QD-LEDs are based on either a down conversion photoluminescence (PL) mechanism or on an electricity-light conversion electroluminescence (EL) mechanism.^{2,3} QDs (or nanocrystals) comprised of halide perovskites (ABX_3 , where A = Cs⁺ or CH₃NH₃⁺ (methyl ammonium; MA) or CH₂(NH₂)₂⁺ (formamidinium; FA) and X = Br, Cl or I) QDs or nanocrystals show outstanding characteristics including superior PL properties, low fabrication cost, and enhanced color performance.⁴⁻⁶ These features make them promising candidates as light emitters for display technology.⁷⁻¹⁰

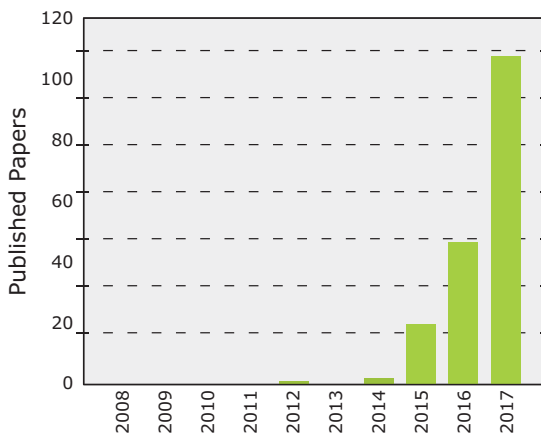


Figure 1. Publications with respect to perovskite QDs. Compiled using Web of Science database and title = (perovskite quantum dots) or title = (perovskite nanocrystal).

As illustrated in **Figure 1**, the development of perovskite QDs dates back to the discovery of enhanced PL emissions in nano-sized perovskite embedded in meso-Al₂O₃ in 2012.¹¹ Publications on this topic have shown exponential growth after highly luminescent colloidal perovskite QDs were first reported in 2015.^{9,10,12} In the past three years, significant progress has been made in the fabrication of perovskite QDs as new strategies have been developed to fabricate high-quality materials, enabling rapid light emitting device development. Even when compared to well-developed CdSe and InP QDs, prototype color conversion LEDs based on perovskite QDs show superior color performance and improved luminous efficiency (120% NTSC, 109 lm/W), enabling enhanced LCD panels (**Figure 2A**).¹³ Meanwhile, the performance of perovskite QD-based EL devices now approaches that of other conventional QDs, even showing promise for use in flexible displays (**Figure 2B**).¹⁴ The controllable fabrication of high quality perovskite QDs is a prerequisite for application exploration. In this mini-review, we will highlight some of the most highly-developed synthetic techniques for perovskite QDs, as well as provide a brief summary of the recent progress toward display applications.

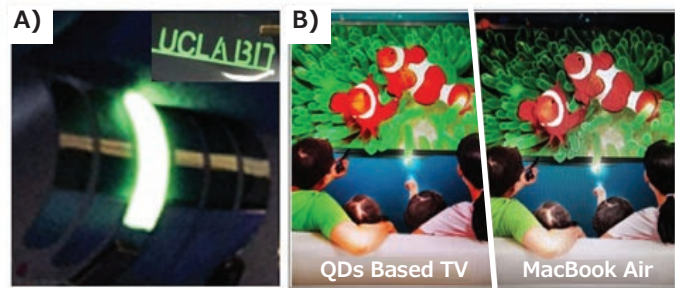


Figure 2. **A)** Images of the flexible perovskite QD-based LEDs and devices tailored with abbreviations of “UCLA & BIT.” **B)** Comparison of perovskite QDs enhanced LCD screen (left) and MacBook LCD screen (right).

Hot Injection Method

The hot injection technique was the first method introduced for the colloidal synthesis of CdSe QDs, and it has since been widely applied to a variety of colloidal nanoparticles.^{15,16} By adapting this technique, colloidal perovskite nanocrystals can be fabricated in a supersaturated solution through fast injection of the precursors at an elevated temperature.^{9,17-19} In 2014, Schmidt et al. first reported the preparation of colloidal $\text{CH}_3\text{NH}_3\text{PbBr}_3$ nanoparticles by mixing $\text{CH}_3(\text{CH}_2)_{17}\text{NH}_3\text{Br}/\text{CH}_3\text{NH}_3\text{Br}$ with PbBr_2 at 80 °C.¹² However, the resulting $\text{CH}_3\text{NH}_3\text{PbBr}_3$ nanoparticles exhibited only moderate PL quantum yield (PLQY) of ~20% and showed poor dispersity in colloidal solution. After optimization, however, the authors were able to achieve a significantly higher PLQY of 87%.²⁰ Soon thereafter, Kovalenko et al. adapted the hot-injection technique to fabricate all inorganic CsPbX_3 QDs with an even higher PLQY of ~90%.⁹ To accomplish this the authors used a PbX_2 type material such as PbI_2 , PbBr_2 , PbCl_2 or a mixture thereof, together with oleylamine (OLA) and oleic acid (OA, **Cat. No. O1008**), dissolved in 1-octadecene (ODE, **Cat. No. 74740**). An injection of Cs-oleate precursor at an elevated temperature of 140–200 °C initiated the nucleation and growth of highly luminescent colloidal CsPbX_3 QDs with tunable emission spectra and PLQYs up to 90% (**Figure 3B**). However, CsPbX_3 QDs synthesized by the hot injection method exhibited poor colloidal stability and rapidly precipitated from the crude solution. To solve this, Yassitepe et al. developed an improved amine-free strategy using OA as the surface ligand, obtaining enhanced colloidal stability and enhanced performance in EL devices.²¹ Protesescu et al. fabricated $\text{CH}_2(\text{NH}_2)_2^+$ doped CsPbI_3 QDs by injecting a mixed precursor of $\text{CH}_2(\text{NH}_2)_2^+$ oleate and Cs-oleate.²² Other groups, including Rogach et al. explored other inorganic ligands, reporting the surface protection of CsPbX_3 (X = Br or I) with a polyhedral oligomeric silsesquioxane.²³

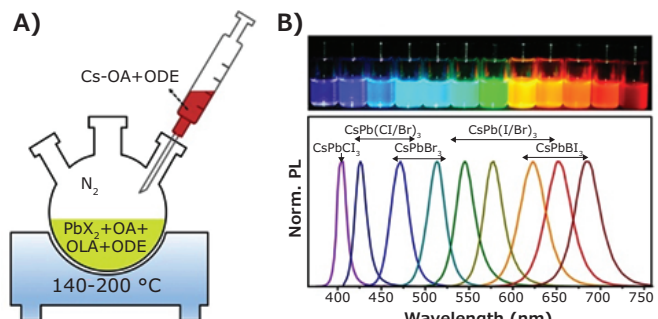


Figure 3. A) A schematic diagram of hot injection synthesis of perovskite QDs/NCs. B) Perovskite QDs/NCs in toluene under UV lamp ($\lambda = 365$ nm) and corresponding PL spectra.⁹ Reproduced with permission: copyright 2015 American Chemical Society.

From a small-scale materials synthesis perspective, the hot injection method is an effective method to fabricate inorganic halide CsPbX_3 QDs, as well as their corresponding one-dimensional nanowires.²⁴ Large-scale synthesis, however, is still limited by the requirement of several complicated processes, such as protection of reaction under inert conditions and the limitation arising from the localized injection of precursor.

Ligand Assisted Reprecipitation (LARP)

Reprecipitation through solvent mixing is a simple way to prepare organic nanoparticles or polymer dots simultaneously.²⁵⁻²⁷ Hybrid perovskites are soluble in many polar solvents, but are insoluble in non-polar ones. Based on the miscible pair of toluene and *N,N*-dimethylformamide (DMF, **Cat. Nos. D158550, 900638, etc.**), our group demonstrated ligand-assisted reprecipitation synthesis (LARP) to fabricate perovskite QDs via solvent mixing with the assistance of long chain organic ligands.¹⁰ **Figure 4A** schematically illustrates the LARP technique. In a typical synthesis of $\text{CH}_3\text{NH}_3\text{PbX}_3$ QDs, the precursor solution (PbX_2 , $\text{CH}_3\text{NH}_3\text{Br}$, n-octylamine, and OA) was dropped into toluene. The change in solubility subsequently induces the formation of highly luminescent colloidal QDs. The investigation of solvent-precursor interactions helped provide insight on the influence of solvents on the formation process and obtained stable iodide-based $\text{CH}_3\text{NH}_3\text{PbI}_3$ quantum dots, as well as morphology-controlled perovskite nanocrystals.^{28,29}

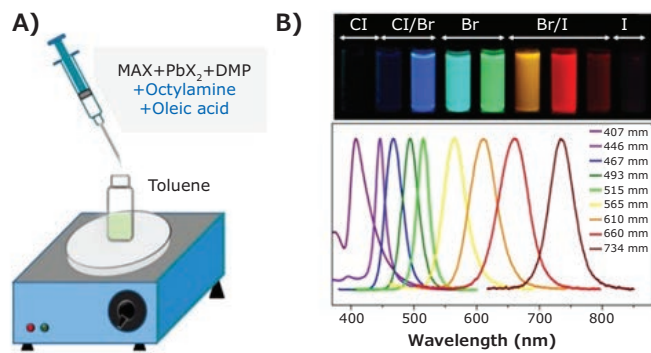


Figure 4. A) A schematic diagram of the ligand-assisted reprecipitation technique (LARP) for perovskite QDs/NCs. B) Perovskite QDs/NCs in toluene under UV lamp ($\lambda = 365$ nm) and corresponding PL spectra.¹⁰ Reproduced with permission: copyright 2015 American Chemical Society.

The LARP technique is both simple and versatile for the synthesis of halide perovskite QDs and other nanostructures. For example, Xiong et al. used it to synthesize amorphous perovskite QDs and achieved bright EL devices.³⁰ Jie et al. developed a simple dip-coating method to effectively fabricate large-area and uniformly dense films for multicolor EL devices.³¹ Other groups have adopted the LARP strategy for the synthesis of other perovskite QDs, including CsPbX_3 QDs, $\text{CH}_2(\text{NH}_2)_2\text{PbX}_3$ and $(\text{CH}_3\text{NH}_3)_3\text{Bi}_2\text{X}_9$ QDs.³²⁻³⁴ However, LARP still has some shortcomings as a synthetic route for device applications, such as low yields of $\text{CH}_3\text{NH}_3\text{PbX}_3$ QDs, and the difficulty of cleaning and purifying the synthesized colloidal solutions, which greatly hinders the application of perovskite QDs to EL devices.

Based on the immiscible solvents hexane and DMF, our group has further developed the emulsion synthesis method to obtain purified $\text{CH}_3\text{NH}_3\text{PbX}_3$ QDs for use in EL device applications.³⁵ Very recently, Sun et al. reported using thermally-induced crosslinking or radical-induced polymerization to address the stability issue and produce more efficient EL devices.³⁶ Further, many groups are working toward the application of down conversion white

LEDs for LCD backlights by capping and sealing perovskites QDs during or after their formation. The inclusion of insulating barrier coatings such as SiO_2 or POSS also has potential to overcome stability issues.^{23,37,38}

Mechanochemical Methods

Both the hot injection technique and LARP synthesis utilize organic solvents and surface ligands, and both require difficult isolation and purification steps. Solid-state mechanochemistry avoids the use of organic solvents, and has the potential to achieve scalable production.^{39,40} This strategy is depicted in **Figure 5**, where metal salts of AX and PbX_2 are used as the immediate raw materials, producing reaction products in a single step after simple milling/grinding at ambient temperature.⁴¹ Highly luminescent QDs can then be obtained by further grinding/milling and surface treatment of the perovskite product with appropriate ligands such as OLA.

Mechanical mixing, especially high-speed milling, induces heat and supplies reaction energy. Sonication is also effective at breaking bulk perovskite powder into nanoparticles.⁴²



Figure 5. A schematic diagram of mechanochemical method (milling/grinding/sonication) for perovskite nanocrystals.

In situ Formation Strategy

For device applications, fabricated QDs must be processed into composite or thin films. However, forming composite films with homogenous distribution or uniform films on proper interfacial layers remains a significant technical challenge. Because perovskites can be processed at room temperature, there are many ways to simplify the process for display applications using an *in situ* formation strategy. For example, Dirin et al. investigated the growth of perovskite nanocrystals in mesoporous silica (meso- SiO_2) matrixes,⁴³ and showed that it can serve as a facile, complementary, and ligand-free preparation route for outstanding perovskite-based composites with broadly tunable emission from the green to near-infrared. In this method, shown in **Figure 6**, highly concentrated solutions of the precursor salts, AX and PbX_2 , were inserted into the pores (width 2.5–50 nm) of various commercially available mesoporous silica templates, followed by the removal of excess solution, and then by drying induced the spatial crystallization of perovskite nanocrystals.

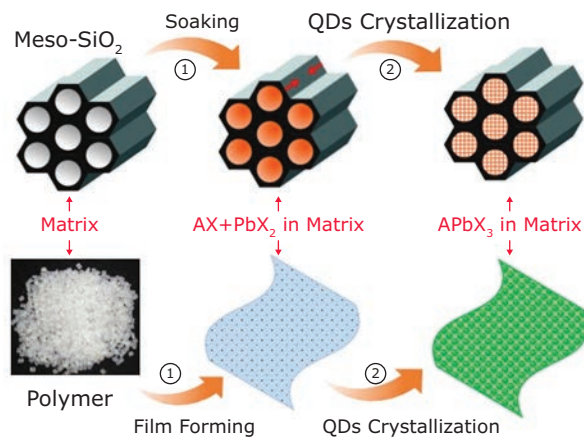


Figure 6. A schematic diagram of *in situ* formation strategy for perovskite QDs/NCs within inorganic and polymer matrices.

The use of mesoporous silica templates allows for the inexpensive and scalable preparation of lead halide perovskite composites. However, the inorganic matrix serves as a hard template and therefore, similar to the traditional rare-earth phosphors, the as-fabricated perovskite based composites require further encapsulation. The hard template does not offer good protection against aggregation, and it has been reported that significant decomposition occurs during the annealing of perovskite NCs in porous TiO_2 at 85 °C, even in an inert atmosphere.

Regarding LCD backlight applications, a more appealing approach is the *in situ* fabrication of perovskite QD based composite films (PQDCF). The polymer matrix tends to form a coherent barrier layer around the perovskite QDs/NCs, protecting them from water, oxygen, and heat of the surrounding environment. Using this method, our group has demonstrated the *in situ* fabrication of $\text{CH}_3\text{NH}_3\text{PbX}_3$ QDs embedded in polyvinylidene fluoride (PVDF) composite films by separating the crystallization processes of PVDF and $\text{CH}_3\text{NH}_3\text{PbX}_3$ QDs through controlled evaporation of DMF.¹³ As illustrated in **Figure 6**, a typical fabrication of $\text{CH}_3\text{NH}_3\text{PbBr}_3$ based PQDCF involved two main stages. In stage I, a mixture of MABr , PbBr_2 and PVDF was dissolved in DMF, and then a uniform precursor film was obtained through solvent evaporation. In stage II, the colorless precursor films were moved out to remove the residual DMF, gradually resulting in green emissive PQDCF. Brightly-luminescent and color-tunable PQDCF with emissions ranging from 440 nm to 730 nm could be similarly obtained by varying the compositions of halides. These PQDCFs show enhanced PL properties with high PLQYs up to 90% ($\pm 5\%$), and improved stability against both moisture and UV radiation, making them useful for on-surface LCD backlight applications. A prototype LED device showed excellent merits in both color quality and luminous efficiency, optimal for display backlights. Soon after, Wang et al. reported a swelling-deswelling microencapsulation strategy that achieved well-dispersed, intimately passivated perovskite QDs inside polymer matrixes that had high photoluminescence efficiency, color purity and ultrahigh stability against both heat and water.⁴⁴

Among these several methods, the *in situ* formation strategy is currently the most promising method for achieving practical display applications, due to its simplified, low-cost, and large-scale processing, as well as the enhanced photoluminescence and stability of the product.

Device Perspective

By adapting the synthetic strategies as previously described, perovskite QDs with superior PL properties have been successfully fabricated and explored for use in display applications. Although studies on perovskite QDs are still in their infancy, tremendous progress has been made toward overcoming the material challenges and technical problems of conventional QDs. By adapting the available techniques from well-developed CdSe QDs, the fundamental framework for implementation in display system appears to be well-established. **Figure 7** describes the important features of CdSe, InP, and perovskite QDs. For LCD backlighting, perovskite QDs are advantageous in brightness and color gamut, but suffer from stability issues. Because of their easy scale-up and simple processing, mechanosynthesis and *in situ* formation are preferred for the fabrication of perovskite-based phosphors for LCD backlights. Building on these advances, the continuous work on material stability and device optimization has already generated the first TV demonstration at CES 2018 by TCL (International Consumer Electronics Show), which is expected to be commercialized in the coming year.

Apart from display applications, the perovskite QDs have also been investigated for solar cell applications. Recent work shows that under operation, perovskite solar cells using these materials retained 90% (97% after dark recovery) of their initial performance after 500 hours of continuous room temperature operation at their maximum power point under 1-sun illumination, a very promising development.⁴⁵

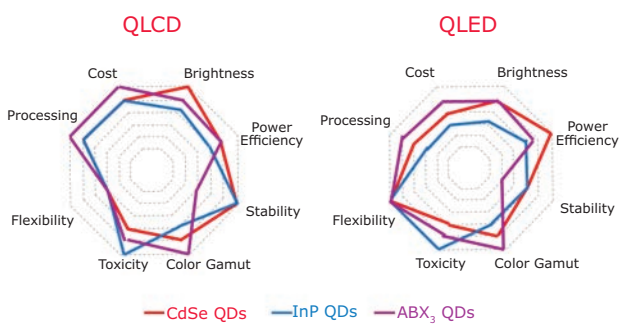


Figure 7. A comparison of the important features of different QDs for display applications.

Although the stability of perovskite QDs is still under debate, there is no doubt that perovskite QDs are highly promising candidates for EL devices. Currently, the device performance of perovskite QD-based EL devices (QLED) still lag behind well-developed CdSe QDs. Solution processing methods such as hot injection and LARP are expected to fabricate purified QDs that

can be used in flexible printing QLED displays. We are looking forward to continued improvements in device performance, as well as growing applications for perovskite QDs in other display technologies such as light emitting cells and laser displays.

References

- (1) Shirasaki, Y.; Supran, G. J.; Bawendi, M. G. et al. *Nat. Photonics* **2013**, 7, 13–23.
- (2) Dai, X.; Deng, Y.; Peng, X. et al. *Adv. Mater.* **2017**, 29, 1607022.
- (3) Jang, E.; Jun, S.; Jang, H. et al. *Adv. Mater.* **2010**, 22, 3076–3080.
- (4) Bai, Z.; Zhong, H. *Sci. Bullet.* **2015**, 60, 1622–1624.
- (5) Yang, G. L.; Zhong, H. Z. *Chin. Chem. Lett.* **2016**, 27, 1124–1130.
- (6) Huang, H.; Polavarapu, L.; Sicert, J. A. et al. *NPG Asia Mater.* **2016**, 8, e328.
- (7) Cho, H.; Jeong, S.; Park, M. et al. *Science* **2015**, 350, 1222–1225.
- (8) Stranks, S. D.; Snaith, H. J. *Nat. Nanotechnol.* **2015**, 10, 391–402.
- (9) Protesescu, L.; Yakunin, S.; Bodnarchuk, M. I. et al. *Nano Lett.* **2015**, 15, 3692–3696.
- (10) Zhang, F.; Zhong, H. Z.; Chen, C. et al. *ACS Nano* **2015**, 9, 4533–4542.
- (11) Kojima, A.; Ikegami, M.; Teshima, K. et al. *Chem. Lett.* **2012**, 41, 397–399.
- (12) Schmidt, L. C.; Pertegas, A.; Gonzalez-Carrero, S. et al. *J. Am. Chem. Soc.* **2014**, 136, 850–853.
- (13) Zhou, Q.; Bai, Z.; Lu, W. et al. *Adv. Mater.* **2016**, 28, 9163–9168.
- (14) Zhao, F.; Chen, D.; Chang, S.; Huang, H.; Tong, K.; Xiao, C.; Chou, S.; Zhong, H.; Pei, Q. *J. Mater. Chem. C* **2017**, 5, 531–538.
- (15) Murray, C. B.; Norris, D. J.; Bawendi, M. G. *J. Am. Chem. Soc.* **1993**, 115, 8706–8715.
- (16) Zhong, H. Z.; Mirkovic, T.; Scholes, G. D. *Nanocrystal Synthesis In Comprehensive Nanoscience and Technology*; Andrew, D. L.; Scholes, G. D.; Wiedermann, G. P., Eds.; Elsevier: Amsterdam, The Netherlands, **2010**; Vol 5, Chapter 5.06, pp 153–201.
- (17) Pan, A.; He, B.; Fan, X. et al. *ACS Nano* **2016**, 10, 7943.
- (18) Song, J.; Li, J.; Li, X. et al. *Adv. Mater.* **2015**, 27, 7162–7167.
- (19) Hassan, Y.; Song, Y.; Pensack, R. D. et al. *Adv. Mater.* **2016**, 28, 566–573.
- (20) Gonzalez-Carrero, S.; Galian, R. E.; Pérez-Prieto, J. *J. Mater. Chem. A* **2015**, 3, 9187–9193.
- (21) Yassitepe, E.; Yang, Z.; Voznyy, O. et al. *Adv. Funct. Mater.* **2016**, 26, 8757–8763.
- (22) Protesescu, L.; Yakunin, S.; Kumar, S. et al. *ACS Nano* **2017**, 11, 3119–3134.
- (23) Huang, H.; Chen, B.; Wang, Z. et al. *Chem. Sci.* **2016**, 7, 5699–5703.
- (24) Zhang, D.; Eaton, S. W.; Yu, Y. et al. *J. Am. Chem. Soc.* **2015**, 137, 9230–9233.
- (25) Kasai, H.; Nalwa, H. S.; Oikawa, H. et al. *Jpn. J. Appl. Phys.* **1992**, 31, L1132.
- (26) Zhao, Y. S.; Fu, H. B.; Peng, A. D. et al. *Adv. Mater.* **2008**, 20, 2859–2876.
- (27) Niu, Y. W.; Zhang, F.; Bai, Z. L. et al. *Adv. Opt. Mater.* **2014**, 3, 112–119.
- (28) Zhang, F.; Chen, C.; Kershaw, S. V. et al. *Chem. Nano. Mat* **2017**, 3, 303–310.
- (29) Zhang, F.; Huang, S.; Wang, P. et al. *Chem. Mater.* **2017**, 29, 3793–3799.
- (30) Xing, J.; Yan, F.; Zhao, Y. et al. *ACS Nano* **2016**, 10, 6623–6630.
- (31) Deng, W.; Xu, X.; Zhang, X. et al. *Adv. Funct. Mater.* **2016**, 26, 4797–4802.
- (32) Li, X.; Wu, Y.; Zhang, S. et al. *Adv. Funct. Mater.* **2016**, 26, 2435–2445.
- (33) Minh, D. N.; Kim, J.; Hyon, J. et al. *Chem. Mater.* **2017**, 29, 5713–5719.
- (34) Leng, M.; Chen, Z.; Yang, Y. et al. *Angew. Chem. Int. Ed.* **2016**, 55, 15012–15016.
- (35) Huang, H.; Zhao, F.; Liu, L. et al. *ACS Appl. Mater. & Interfaces* **2015**, 7, 28128.
- (36) Sun, H.; Yang, Z.; Wei, M. et al. *Adv. Mater.* **2017**, DOI: 10.1002/adma.201701153.
- (37) Huang, S.; Li, Z.; Kong, L. et al. *J. Am. Chem. Soc.* **2016**, 138, 5749–5752.
- (38) Wang, H. C.; Lin, S. Y.; Tang, A. C. et al. *Angew. Chem. Int. Ed.* **2016**, 55, 7924.
- (39) Prochowicz, D.; Frankevicius, M.; Ciesiak, A. M. et al. *J. Mater. Chem. A* **2015**, 3, 20772–20777.
- (40) Jodlowski, A. D.; Yepez, A.; Luque, R. et al. *Angew. Chem., Int. Ed.* **2016**, 55, 14972–14977.
- (41) Zhu, Z.; Yang, Q.; Gao, L. et al. *J. Phys. Chem. Lett.* **2017**, 8, 1610–1614.
- (42) Hintermayr, V. A.; Richter, A. F.; Ehrat, F. et al. *Adv. Mater.* **2016**, 28 (43), 9478.
- (43) Dirin, D. N.; Protesescu, L.; Trummer, D. et al. *Nano Lett.* **2016**, 16, 5866.
- (44) Wang, Y.; He, J.; Chen, H. et al. *Adv. Mater.* **2016**, 28, 10710–10717.
- (45) Tan, H.; Jain, A.; Voznyy, O.; et al. *Science* **2017**, 355, 722–726.

Cadmium-Free Quantum Dots

For a complete list of available materials, visit SigmaAldrich.com/Cd-freeqd.

PbS

Name	Form	Description	Fluorescence Emission, λ_{em} (nm)	Cat. No.
PbS core-type quantum dots	10 mg/mL in toluene	oleic acid coated	1000	747017-10ML
		oleic acid coated	1200	747025-10ML
		oleic acid coated	1400	747076-10ML
		oleic acid coated	1600	747084-10ML
		oleic acid coated	900	900733-5ML
		oleic acid coated	1100	900735-5ML
		oleic acid coated	1300	900737-5ML
		oleic acid coated	1500	900728-5ML

CsPb(Cl,Br)₃-Based Perovskite Quantum Dots

Name	Form	Description	Fluorescence Emission, λ_{em} (nm)	Cat. No.
Perovskite quantum dots	10 mg/mL in toluene	oleic acid and oleylamine coated	450	900748-5ML
		oleic acid and oleylamine coated	480	900747-5ML
		oleic acid and oleylamine coated	510	900746-5ML

Graphene Quantum Dots

For a complete list of available materials, visit SigmaAldrich.com/carbonqd.

Name	Form	Description	Fluorescence Emission, λ_{em} (nm)	Cat. No.
Graphene quantum dots	powder	blue luminescent topographic height: 1-2.0 nm	450	900726-50MG
	1 mg/mL in H ₂ O, suspension	blue luminescent topographic height: 1-2.0 nm	445	900708-50ML
	1 mg/mL in H ₂ O, suspension	cyan luminescent topographic height: 1-2.0 nm	490	900707-50ML
	1 mg/mL in H ₂ O, suspension	aqua green luminescent topographic height: 1-2.0 nm	520-540	900712-50ML
	powder	aqua green luminescent topographic height: 1-2.0 nm	520-540	900713-50MG

InP/ZnS

Name	Form	Description	Fluorescence Emission, λ_{em} (nm)	Cat. No.
InP/ZnS quantum dots	5 mg/mL in toluene	stabilized with oleylamine ligands	530	776750-5ML
		stabilized with oleylamine ligands	560	776793-5ML
		stabilized with oleylamine ligands	590	776769-5ML
		stabilized with oleylamine ligands	620	776777-5ML
		stabilized with oleylamine ligands	650	776785-5ML

Cadmium-Based Quantum Dots

Core-Type Quantum Dots

For a complete list of available materials, visit SigmaAldrich.com/coretypeqd.

CdTe

Name	Form	Description	Fluorescence Emission, λ_{em} (nm)	Cat. No.
CdTe core-type quantum dots	powder	COOH functionalized	510	777986-10MG 777986-25MG
		COOH functionalized	520	777935-10MG 777935-25MG
		COOH functionalized	570	777943-10MG 777943-25MG
		COOH functionalized	610	777951-10MG 777951-25MG
		COOH functionalized	770	777994-10MG 777994-25MG
		COOH functionalized	710	777978-10MG 777978-25MG

Core-Shell Type Quantum DotsFor a complete list of available materials, visit SigmaAldrich.com/core-shellqd.***CdS/ZnS***

Name	Form	Description	Fluorescence Emission, λ_{em} (nm)	Cat. No.
CdS/ZnS core-shell type quantum dots	4 μ M in PBS, dispersion	amine	400	900290-250UL
		amine	425	900305-250UL
		amine	450	900304-250UL
	1 mg/mL in H ₂ O, dispersion	carboxylic acid	400	900298-1ML
		carboxylic acid	425	900299-1ML
		carboxylic acid	450	900294-1ML
	lyophilized, powder	carboxylic acid	400	900310-1MG
		carboxylic acid	425	900308-1MG
		carboxylic acid	450	900332-1MG
	4 μ M in H ₂ O, dispersion	PDDA coated	400	900306-250UL
		PDDA coated	425	900307-250UL
		PDDA coated	450	900309-250UL
		PEG	400	900303-250UL
		PEG	425	900302-250UL
		PEG	450	900301-250UL
	5 mg/mL in toluene, dispersion	oleic acid	400	900286-1ML
		oleic acid	425	900333-1ML
		oleic acid	450	900334-1ML
	powder	oleic acid	400	900280-10MG
		oleic acid	425	900283-10MG
		oleic acid	450	900282-10MG

CdSe/ZnS

Name	Form	Description	Fluorescence Emission, λ_{em} (nm)	Cat. No.
CdSe/CdS core-shell type quantum rods	5 mg/mL in hexane, dispersion	carboxylic acid	530	900511-1ML
		carboxylic acid	560	900512-1ML
		carboxylic acid	590	900515-1ML
		carboxylic acid	620	900514-1ML
CdSe/ZnS core-shell type quantum dots	solid	stabilized with octadecylamine ligands	520	748021-10MG 748021-25MG
		stabilized with octadecylamine ligands	540	748056-10MG 748056-25MG
		stabilized with octadecylamine ligands	560	748080-10MG 748080-25MG
		stabilized with octadecylamine ligands	580	748129-10MG 748129-25MG
		stabilized with octadecylamine ligands	600	748099-10MG 748099-25MG
		stabilized with octadecylamine ligands	620	790192-10MG 790192-25MG
		stabilized with octadecylamine ligands	630	790206-10MG 790206-25MG

Alloyed Quantum Dots

For a complete list of available materials, visit SigmaAldrich.com/alloyedqd.

Name	Form	Description	Fluorescence Emission, λ_{em} (nm)	Cat. No.
CdSeS/ZnS alloyed quantum dots	1 mg/mL in toluene	oleic acid	450	753742-5ML 753742-25ML
		oleic acid	490	753750-5ML 753750-25ML
		oleic acid	525	753769-5ML 753769-25ML
		oleic acid	540	753777-5ML 753777-25ML
		oleic acid	575	753785-5ML 753785-25ML
		oleic acid	630	753793-5ML 753793-25ML
		oleic acid	665	753807-5ML 753807-25ML
	1 mg/mL in H ₂ O	COOH functionalized	490	754226-1ML 754226-5ML
		COOH functionalized	525	753831-1ML 753831-5ML
		COOH functionalized	540	753866-1ML 753866-5ML
		COOH functionalized	575	753874-1ML 753874-5ML
		COOH functionalized	630	753882-1ML 753882-5ML
		COOH functionalized	665	753890-1ML 753890-5ML
CdSeS/ZnS alloyed quantum dots kit	5 × 1 mg/mL in toluene	oleic acid	490-665	753823-1KT
	5 × 1 mg/mL in H ₂ O	COOH functionalized	490-665	753904-1KT

Product Highlight

Bright & Cadmium-free

Quantum dots exhibit excellent photoluminescence and electroluminescence properties such as narrow emission bandwidth and high brightness.

Choose cadmium-free quantum dots for applications where toxicity is a concern.

Cd-free Quantum Dots find applications in:

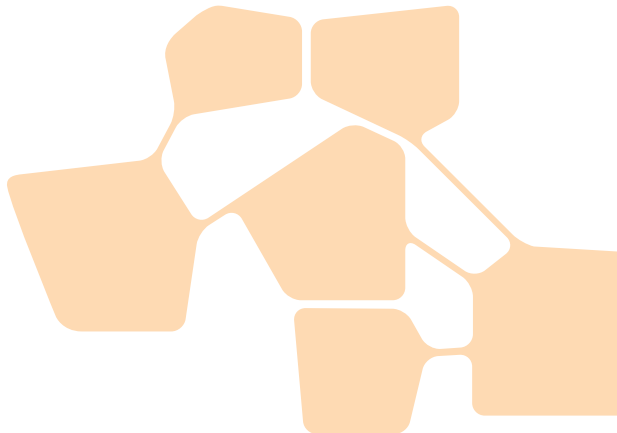
- LEDs • Photovoltaics • Displays • Transistors • Solid-state lighting



Product Name	Product Description	Fluorescence Emission (λ_{em})	Product No.
CsPb(Cl,Br) ₃ -based perovskite quantum dots	10 mg/mL in toluene, oleic acid and oleylamine coated	450 nm	900748
	10 mg/mL in toluene, oleic acid and oleylamine coated	480 nm	900747
	10 mg/mL in toluene, oleic acid and oleylamine coated	510 nm	900746
InP/ZnS Core-Shell Type Quantum Dots	5 mg/mL in toluene, stabilized with oleylamine ligands	550 nm	776750
	5 mg/mL in toluene, stabilized with oleylamine ligands	590 nm	776769
	5 mg/mL in toluene, stabilized with oleylamine ligands	650 nm	776785
PbS Core-Type Quantum Dots	10 mg/mL in toluene, oleic acid coated	900 nm	900733
	10 mg/mL in toluene, oleic acid coated	1100 nm	900735
	10 mg/mL in toluene, oleic acid coated	1300 nm	900737
	10 mg/mL in toluene, oleic acid coated	1500 nm	900728

To find out more, visit SigmaAldrich.com/quantumdots.

Ionic Liquids Based Electrolytes for Rechargeable Batteries



Meng-Chang Lin,^{1,2*} Hui Chen,² and Hongjie Dai^{3*}

¹AB Systems Inc., 2458 Embarcadero Way, Palo Alto, California 94303, USA

²College of Electronic Engineering and Automation, Shandong University of Science and Technology, 266590, Qingdao, China

³Department of Chemistry, Stanford University, Stanford, California 94305, USA

*Email: mc.lin@alcbattery.com; mengchanglin@sdu.edu.cn

Introduction

Room temperature ionic liquids (RTILs) are molten salts with melting points well below 100 °C. Most RTILs are organic salts with a high degree of variability that can be controlled by molecular design. Ionic liquids (ILs) have many useful properties, including low vapor pressure, a broad liquid state temperature window, high chemical and thermal stability, wide electrochemical voltage window, non-flammability, high ionic conductivity, and good solubility in various organic or inorganic materials.¹ The unique properties of ILs make them particularly promising candidates as (1) environmentally benign or “green” alternatives to organic solvents for chemical synthesis, catalysis, separation, and extraction, (2) versatile electrolytes for electrochemistry and photovoltaics, and (3) novel functional materials for lubrication, microfluidics, propellants, and sensors.¹

In recent years, the potential use of ILs as novel electrolytes for various secondary, rechargeable batteries has attracted great interest. ILs have been used to accelerate the development of aluminum-based batteries,^{2–9} decrease the flammability of lithium-based batteries,^{10–13} and increase the cycling stability and Coulombic efficiency of dual-graphite batteries.^{14–16} Aluminum anodes are low-cost, have low-flammability, and possess unique three-electron redox properties. As a result, rechargeable aluminum batteries promise cost-savings and higher safety, which could lead in a new direction for energy storage technology.² ILs are ideal electrolytes for developing Al batteries that avoid the problem of passivating aluminum hydroxide on Al surface in aqueous electrolytes. Several cathode materials including graphite^{2–6} and transition metal oxides^{7–9} have been studied for use in Al batteries in IL electrolytes. On the other hand, lithium-based secondary batteries that consist of graphite

or pure lithium anodes and organic solvent electrolytes have the potential for high operating voltages, high energy density, and good cycling stability, but have the disadvantage of flammable electrolytes that can lead to safety hazards.^{10–13} ILs have also been studied to improve the safety of lithium-ion batteries over the years. Dual-graphite batteries that employ low-cost graphite for both the anode and cathode, and use non-flammable ionic liquid electrolytes could lead to environmental benefits, improved safety, and cost-savings.^{14–16}

Here, we present a short review of ionic liquid electrolytes used in state-of-the-art rechargeable batteries including high performance and low-cost aluminum batteries, non-flammable Li-based batteries, and high-cycling and stable dual-graphite batteries. We also outline the key issues explored so as to identify the future direction of IL development. We further discuss how the versatility of ionic liquid electrolytes can boost the development of rechargeable batteries for energy storage.

Synthesis of Ionic Liquids

ILs are composed of bulky and asymmetrical cations, such as imidazolium, pyrrolidinium, pyridinium, pyrrolidinium, ammonium, and phosphonium, and different inorganic or organic anions, including halides (chloride [Cl⁻], bromide [Br⁻], iodide [I⁻]), acetate [AcO⁻], tetrafluoroborate [BF₄⁻], hexafluorophosphate [PF₆⁻], tetrachloroaluminate [AlCl₄⁻], bis(trifluoromethanesulfonyl) imide [TFSI⁻], ethyl sulfate [EtSO₄⁻], dicyanamide [N(CN)₂⁻], and thiocyanate [SCN⁻].¹ Figure 1 shows the molecular structure of cations and anions of several room temperature ionic liquids commonly used for rechargeable batteries.

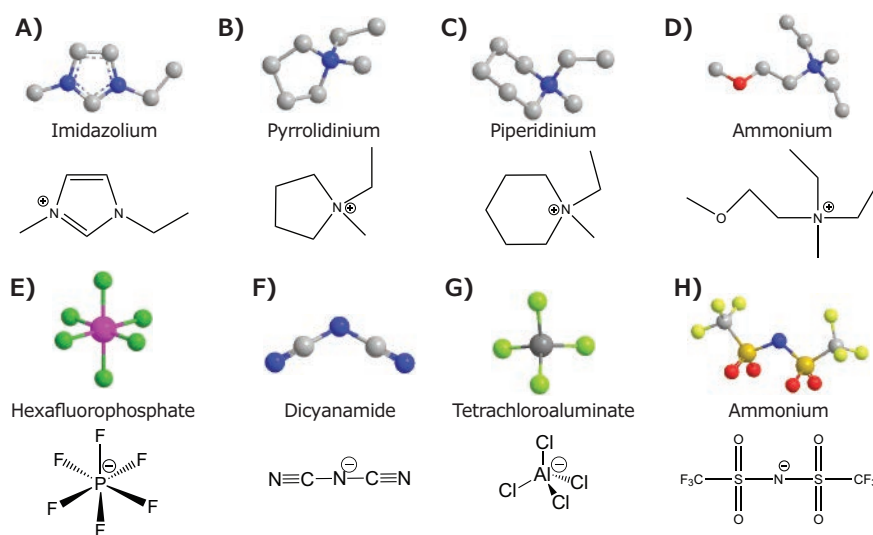


Figure 1. Schematic illustration of the molecular structure of cations and anions from the room temperature ionic liquids commonly used for rechargeable batteries. A) Imidazolium cation, B) Pyrrolidinium cation, C) Piperidinium cation, D) Ammonium cation, E) Hexafluorophosphate anion, F) Dicyanamide anion, G) Tetrachloroaluminate anion, and H) Bis(trifluoromethane)sulfonamide anion.

ILs, in most cases, can be prepared through synthetic processes using either one-step or two-step methods. For example, one can obtain imidazolium halide salt by simple alkylation of 1-methylimidazole (**Cat. No. M50834**) with an alkyl halide (halide anions (X^-): Cl^- , Br^- or I^- , etc.) (see **Figure 2**). The resulting imidazolium halide salts can be directly used as an IL or to produce the imidazolium salt with a desired anion in the subsequent metathesis. First, the imidazolium halide salt is mixed with an $M^+\text{A}^-$ metal salt (M^+ : Ag^+ , Na^+ or K^+ , etc.; A^- : BF_4^- , PF_6^- , TSI^- , etc.). Next, the halide anion is replaced by the desired A^- anion to obtain the imidazolium A^- salt. However, in some cases, high-purity ionic liquids are difficult to obtain through metal salts metathesis, since $M^+\text{X}^-$ (as impurity) is soluble in the ILs. The presence of residual halide contaminations in the ILs can influence the physical properties.¹⁷

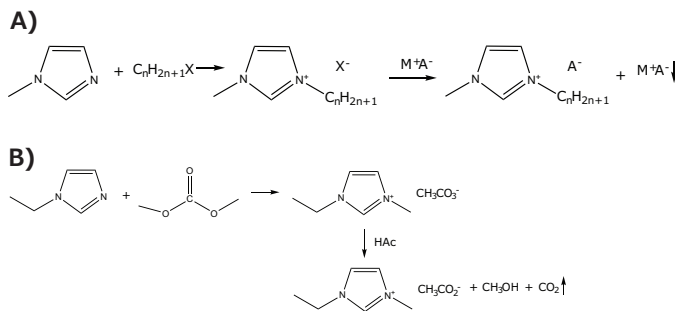


Figure 2. Synthesis of A) imidazolium-based salts by alkylation of 1-methylimidazole with an alkyl halide, and the obtained halide salts are used for metathesis with metal salts to produce the imidazolium salt with a desire anion. B) 1-Ethyl-3-methylimidazolium acetate (**Cat. No. 689483**) employing dimethylcarbonate as alkylating agent, and then by neutralizing the solution with acid. The insoluble by-products can be easily removed through vacuum and heating processes.

Alternatively, high-purity ILs can be obtained through a metal salt-free process.¹⁸ For example, 1-alkane-3-methylimidazolium methyl carbonate salts can be prepared by alkylation of 1-alkaneimidazole with carbonate at 210 °C in a PTFE-coated autoclave for over 2 hours. ILs can be obtained by further neutralizing the solutions with the acid, with by-products of insoluble methanol and gaseous CO_2 . The insoluble by-products are easily removed through vacuum and heating processes.

Aluminum-Based Batteries with Ionic Liquid Electrolyte

Studies²⁻⁹ have shown that imidazolium salts (such as [EMIm]Cl) or amide ligands (such as urea) can be used to form ionic liquid electrolytes or deep eutectic solvent (quasi ionic liquid) electrolytes for rechargeable aluminum batteries. Through mixing with AlCl_3 , these electrolytes contain redox active chloroaluminate anions (such as AlCl_4^- and Al_2Cl_7^-) and $[\text{AlCl}_2\cdot(\text{ligand})_n]^+$ cations.

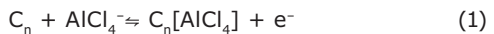
In the late 80s, Gifford et al.² presented an aluminum/chlorine rechargeable cell that employed an Al anode and graphite cathode electrode with an $\text{AlCl}_3/1,2\text{-dimethyl-3-propylimidazolium chloride}$ electrolyte. The graphite cathode electrode played the role of the reversible intercalation electrode for chlorine. The cell possessed an average discharge voltage of 1.7 V and a maximum charge-storage capacity of 35 mAh g⁻¹ relative to the mass of graphite. However, it was observed that almost 85% of capacity decayed after over 100 cycles due to the disintegration of the graphite electrode. In 2015, we unveiled an ultrafast rechargeable aluminum-ion battery with $\text{AlCl}_3/[EMIm]\text{Cl}$ electrolyte.³ The battery exhibited a well-defined discharge voltage plateaus near 2 V, a specific capacity about 70 mAh g⁻¹ and Coulombic

efficiency of almost 98%. A novel three-dimensional graphitic-foam cathode was found that enabled fast anion diffusion and intercalation, allowing a charging time of 1 minute with high current densities of 4,000 mA g⁻¹ (3,000 W kg⁻¹). All these qualities allowed the device to withstand almost 7,500 cycles without any capacity decay (**Figure 3**). Afterwards, we published successive works using natural graphite flakes as the cathode material.^{5,6} The natural graphite flakes⁵ cathode showed superior electrochemical performance in AlCl₃/[EMIm]Cl electrolyte. For example, the cell achieved a specific capacity of 110 mAh g⁻¹ with a Coulombic efficiency of almost 98% at a current density of 99 mA g⁻¹ (0.9 C) and clear discharge voltage plateaus (2.25–2.0 V and 1.9–1.5 V).

We have also developed an Al-ion battery with high Coulombic efficiency (~99.7%) using aluminum as the anode, graphite as the cathode, and a low cost ionic liquid analog electrolyte made from a 1.3:1 molar ratio mixture of AlCl₃ and urea.⁶ The battery displayed a discharge voltage plateaus around 1.9 and 1.5 V (average discharge: 1.73 V) and yielded a specific cathode capacity of ~73 mAh g⁻¹ at a current density of 100 mA g⁻¹ (~1.4 C). It is not difficult to achieve such a high Coulombic efficiency over a range of charge or discharge rates with stability over ~150–200 cycles. However, the challenge is that the

~10-fold higher viscosity and lower ionic conductivity of urea-based electrolytes (such as AlCl₃/urea: 1.3 (in mole ratio) of ~1.23 mS cm⁻¹ at 25 °C than those of AlCl₃/EMImCl), decreases the C-rate capability of the urea based aluminum batteries.

In the Al anode/graphite cathode battery, the simplified Al/graphite cell redox reactions during the charging and discharging process can be written as follows:³



where *n* refers to the molar ratio of carbon atoms to the intercalated anions in the graphite. The balanced AlCl₄⁻ and Al₂Cl₇⁻ concentrations in the electrolyte ensured an optimal charging capacity at the cathode, with abundant AlCl₄⁻ for charging or intercalating into graphite (as shown in **Equation 1**) and sufficient Al₂Cl₇⁻ for charging or electrodepositing Al at the anode (as shown in **Equation 2**). For the urea based electrolyte case, AlCl₄⁻, Al₂Cl₇⁻ anions and [AlCl₂·(urea)*n*]⁺ cations co-exist in the AlCl₃/urea electrolyte. Aluminum deposition might occur through two routes involving the anions (**Equation 2**) and cations (**Equation 3**).⁶

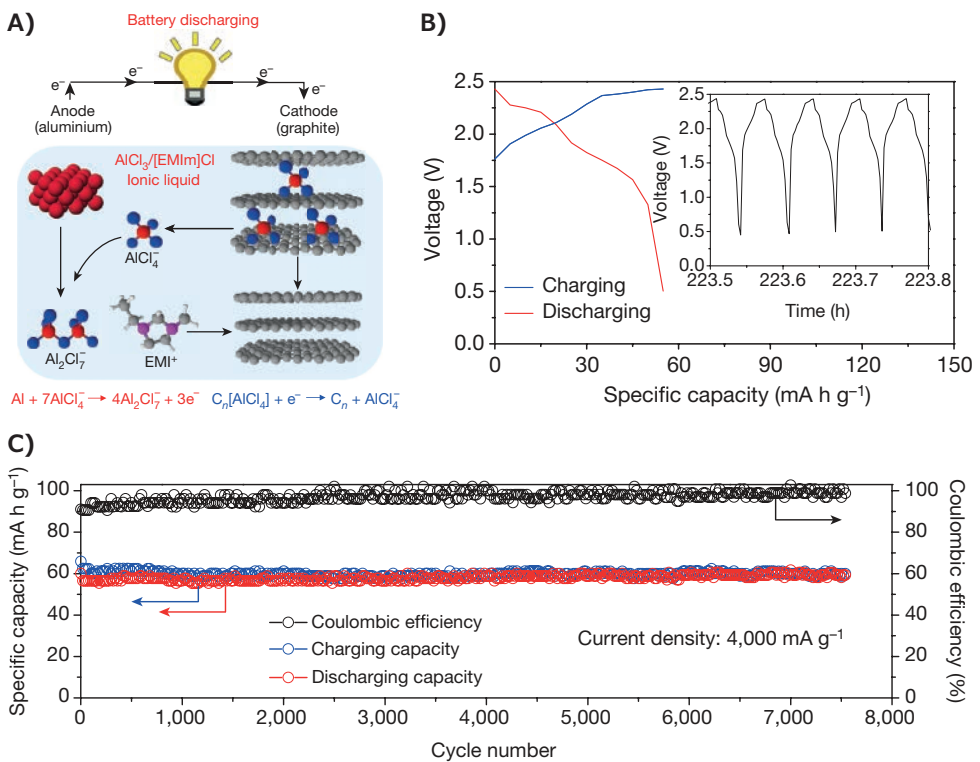
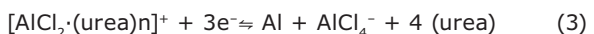


Figure 3. A) Schematic drawing of the Al/graphite cell during discharge, using the optimal composition of the AlCl₃/[EMIm]Cl ionic liquid electrolyte. On the anode side, metallic Al and AlCl₄⁻ were transformed into Al₂Cl₇⁻ during discharging, and the reverse reaction took place during charging. On the cathode side, predominantly AlCl₄⁻ was intercalated and deintercalated between graphite layers during charge and discharge reactions, respectively. B) Galvanostatic charge and discharge curves of an Al/graphitic-foam pouch cell at a current density of 4,000 mA g⁻¹. C) Long-term stability test of an Al/graphitic-foam pouch cell over 7,500 charging and discharging cycles at a current density of 4,000 mA g⁻¹. Reproduced with permission from reference 3, copyright 2015 Nature Publishing Group.

Beside graphite, transition metal oxides⁷⁻⁹ have been suggested as candidate cathode materials for aluminum-ion batteries. The Archer group⁷ at Cornell University employed vanadium pentoxide (V_2O_5) nanowire as the cathode, Al as the anode, and $AlCl_3/[EMIm]Cl$ as the electrolyte. However, subsequent work revealed the V_2O_5 cathode material was electrochemically inactive in the $AlCl_3/[EMIm]Cl$ electrolyte and the stainless steel was acting as the active electrode in the current collector. Thus the mass of the active material was unknown.¹⁹ Despite the argument, the intercalation and deintercalation of Al^{3+} in VO_2 cathode ($AlCl_3/1$ -butyl-3-methylimidazolium chloride electrolyte) and amorphous V_2O_5 cathode ($AlCl_3/dipropylsulfone/toluene$) has been reported by several research groups.⁹ According to Brown et al.,⁸ spinel Mn_2O_4 was also verified to be a feasible cathode for the Al-ion battery in $AlCl_3/[EMIm]Cl$ electrolyte without any other experimental details. As for the transition metal oxide⁷⁻⁹ cathode, researchers have suggested that Al^{3+} accumulated on the cathode during the battery discharging. Then free Al^{3+} migrated into the cathode to form the Al intercalated compounds (as shown in **Equation 4**, using V_2O_5 cathode as an example^{9(b)}).



Lithium-Based Batteries with Ionic Liquid Electrolytes

High thermal stability is expected in a RTIL Li-based battery. Lombardo's group¹⁰ at Università di Roma reported that the addition of *N*-butyl-*N*-methylpyrrolidinium bis(trifluoromethanesulfonyl)imide ($Pyr_{14}TFSI$) to the commercial carbonate-based electrolyte (1M $LiPF_6$ in EC:DMC (LP30)) can reduce the self-extinguished time of the electrolyte mixture to a great extent when exposed to a free flame in a full Li-ion cell (see **Figure 4**). Sakaebi et al.¹¹ pointed out that *N*-methyl-*N*-propylpiperidinium bis(trifluoromethanesulfonyl)imide ($PP_{13}TFSI$) is the most promising candidate for Li battery electrolyte. The $Li/LiCoO_2$ cell in this electrolyte showed excellent performance, with stable capacity of $LiCoO_2$ and good Coulombic efficiency (>97% at a rate of C/10) over cycling. The $Li/LiCoO_2$ cell can be opened just after the final charge in air and no ignition was observed while fire contacted the cell.¹¹

The cycling stability of Li-based batteries with various ionic liquid electrolytes was also investigated. According to Holzapfel et al.,¹² when $LiCoO_2$ positive electrodes were cycled in a 5%-vinylene-carbonate-added 1 M solution of $LiPF_6$ in 1-Ethyl-3-methylimidazolium-bis(trifluoromethylsulfonyl)imide (EMI-TFSI, **Cat. No. 11291**) good charge capacity retention of more than 300 cycles was observed when $Li_4Ti_5O_{12}$ was used as the negative electrode. However, the stability of neat EMI-based electrolyte against reduction seems insufficient in the lithium battery system (i.e., Li metal as negative electrode). Elia et al.¹³ showed an advanced long-life lithium-ion battery by employing a $Pyr_{14}TFSI$ -LiTFSI non-flammable ionic liquid electrolyte, a nanostructured tin-carbon nanocomposite anode, and a layered $LiNi_{1/3}Co_{1/3}Mn_{1/3}O_2$ cathode. The battery was subjected to prolonged cycles at 40 °C, revealing a stable capacity of about 140 mAh g⁻¹ and retention above 99% after over 400 cycles.

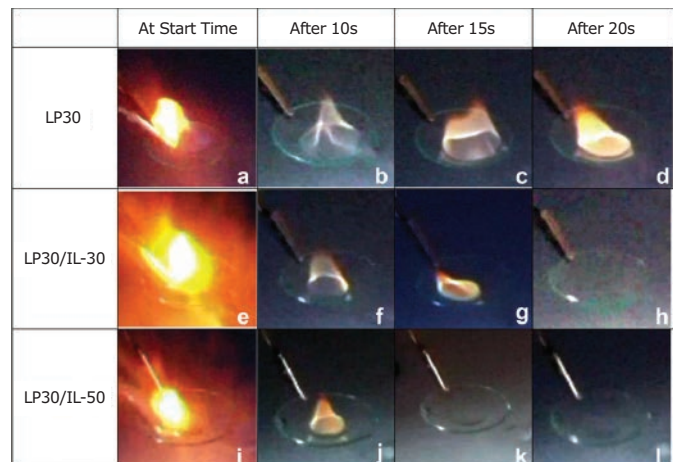


Figure 4. Pictures of the flammability performances of LP30 at A) starting time, B) after 10 s, C) after 15 s, and D) after 20 s, LP30/ $Py_{14}TFSI$ 70/30 wt/wt at E) starting time, F) after 10 s, G) after 15 s, and H) after 20 s, and LP30/ $Py_{14}TFSI$ 50/50 wt/wt at I) starting time, J) after 10 s, K) after 15 s, and L) after 20 s. Reproduced with permission from reference 10, copyright 2012 Elsevier B.V.

Dual-Graphite Batteries with Ionic Liquid Electrolyte

The first dual-graphite battery was suggested by Carlin et al.,¹⁴ using various RTILs, such as 1-ethyl-3-methylimidazolium tetrachloroaluminate ($EMI^+AlCl_4^-$, **Cat. No. 724424**). EMI^+ intercalated into the graphite anode while $AlCl_4^-$ intercalated into the graphite cathode during the charging process. The cell provided a discharge voltage of 3.15 V. However, the reversibility of the intercalation or the deintercalation behavior of this dual-graphite cell was relatively poor, due to the instability of EMI^+ intercalant within graphite.¹⁴ In particular, electrolytes with a high stability vs. oxidation are required for dual-graphite batteries, due to the very high operation potentials of the cathode, which may surpass 5 V vs. Li/Li^+ .¹⁵ Winter's group¹⁵ at the University of Münster demonstrated promising results with high electrochemical performance of a dual-graphite cell using ionic liquid electrolyte mixtures of $Py_{14}TFSI/LiTFSI$ and ethylene sulfite (ES) as an solid electrolyte interface (SEI)-forming additive. The cell exhibited a stable cycling performance after over 500 cycles with a discharge capacity of about 50 mAh g⁻¹ at a cut-off charge voltage of 5.14 V vs. Li/Li^+ (**Figure 5**). In addition, the Coulombic efficiency displayed an average value of 99.8%.

Fan et al.¹⁶ reported an ionic liquid dual-graphite cell with pure 1-butyl-1-methylpiperidinium bis(trifluoromethylsulfonyl)imide ($PP14TFSI$, **Cat. No. 713074**) as the electrolyte, affording a high discharge plateau initiating at 4.4 V, a well-defined capacity of 82 mAh g⁻¹, an ultra-wide charge/discharge potential range of 1.0-5.0 V and a superior stability of ~100% capacity retention for 600 cycles.

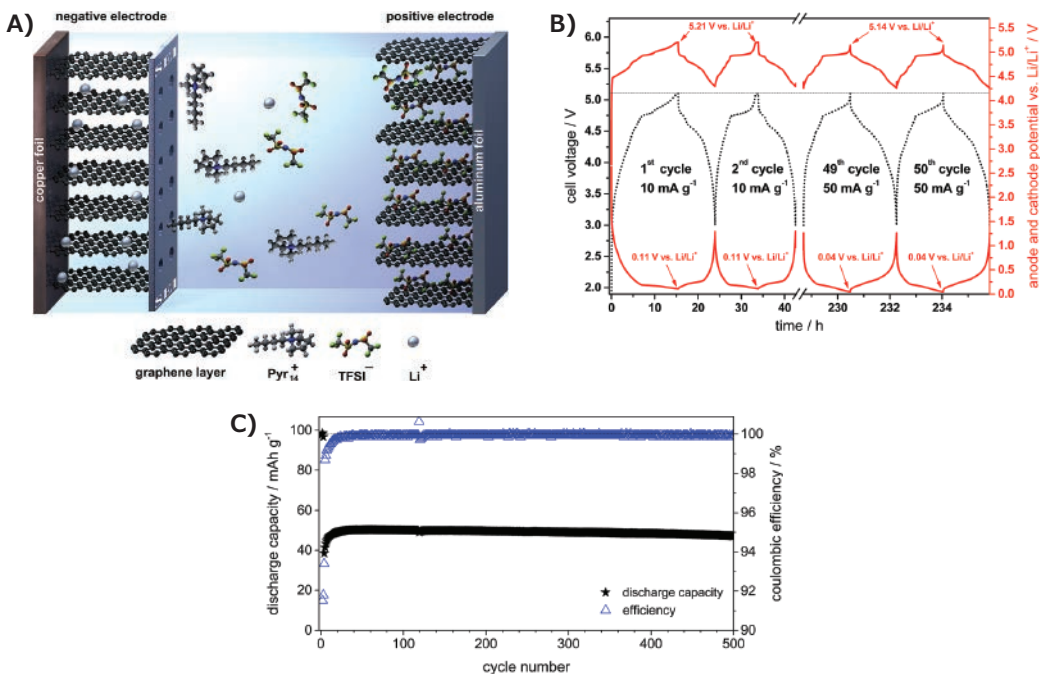


Figure 5. A) Schematic illustration of a dual-graphite cell with an effective SEI layer at the graphite anode during the charge process. The negative graphite electrode is protected from cointercalation reactions of pyrrolidinium cations by the SEI layer; the SEI still allows the transport and intercalation of lithium ions. B) Cell voltage vs. time profile (black, dotted curve) and anode and cathode potential vs. time profiles (red curves) of the CG/KS6L dual-graphite cell during representative cycles of the constant current charge/discharge cycling process. The specific current for cycles 1–3 is 10 mA g⁻¹ and 50 mA g⁻¹ for the following cycles. Cell voltage range: 3.0 V and 5.1 V. C) Discharge capacity curve and Coulombic efficiency curve of the constant current charge/discharge cycling performance of the CG/KS6L dual-graphite cell. Cell voltage range: 3.0 V and 5.1 V; specific current for charge and discharge: 10 mA g⁻¹ (for cycles 1–3) and 500 mA g⁻¹ (for cycles 4–500). Reproduced with permission from reference 15, copyright 2014 The Royal Society of Chemistry.

Dual-graphite batteries with the ionic liquid electrolyte did not show any flammability and can afford high discharge voltages (3.0–5.0 V), which has attracted the attention of researchers. The ionic liquid electrolyte not only acts as a charge carrier but also as a source for intercalation guests for the graphite anode and graphite cathode. The proposed electrochemical intercalation processes can be written as follows:



where the cation could be EMI⁺, Li⁺ or Na⁺ and anion could be AlCl₄⁻, BF₄⁻, TFSI⁻ or PF₆⁻.^{14–16}

Perspective

By using an AlCl₃/EMImCl ionic liquid electrolyte, aluminum batteries with a graphite cathode display excellent cycling stability and C-rate capability. In addition to AlCl₃/EMImCl, inexpensive AlCl₃/urea can be used as an electrolyte in aluminum batteries, which could greatly decrease their cost. However, the high viscosity of the urea-based electrolytes currently limits their C-rate capability and specific capacity in aluminum batteries.

Although EMIm-based IL electrolytes exhibit high conductivity as well as low viscosity among the ILs in lithium batteries, the insufficient cycling stability limits their utility using pure lithium

as the negative electrode. Pyrrolidinium salts have also been mixed with the conventional alkylcarbonate-based electrolyte so as to improve the flame resistance of Li-based batteries. On the other hand, Li-based batteries using neat piperidinium-based ionic liquid electrolytes do show low-flammability and good cycling stability using a pure Li anode. To compete with the commercial lithium-ion battery, long-term cycling stability (such as 80% capacity retention after 2000 cycles) will be the main hurdle for lithium batteries with ionic liquid electrolytes.

Noticeably, dual-graphite batteries with high conductivity EMIm-based IL electrolytes displayed high self-discharge, leading to low Coulombic efficiency. Mixtures of pyrrolidinium and TFSI salts were used as electrolytes for dual-graphite batteries in order to increase the cycling stability as well as the Coulombic efficiency. However, low C-rate capability is still the main challenge for dual-graphite batteries with IL based electrolytes.

Ionic liquids show a broad electrochemical stability window of up to 5 V with no observed flammability even in direct contact with fire and relative high conductivity. This makes them promising electrolytes for high performance/low-cost aluminum batteries, non-flammable Li-based batteries, and for providing high cycling stability in dual-graphite batteries. Together these achievements suggest a bright commercial future for IL electrolytes in advanced batteries for energy storage.

Acknowledgement

M.-C. L. acknowledges support from the Taishan Scholar Project of Shandong Province of China (No.tsqn20161025).

References

- (1) Ohno, H. *Electrochemical Aspects of Ionic Liquids*; 2005, DOI:10.1002/0471762512.ch6.
- (2) Gifford, P. R.; Palmisano, J. B. *ChemInform* **1988**, *19* (25), 650-654.
- (3) Lin, M.-C.; Gong, M.; Lu, B.; Wu, Y.; Wang, D.-Y.; Guan, M.; Angell, M.; Chen, C.; Yang, J.; Hwang, B.-J.; Dai, H. *Nature* **2015**, *520* (7547), 324-328.
- (4) Wu, Y.; Gong, M.; Lin, M. C.; Yuan, C.; Angell, M.; Huang, L.; Wang, D. Y.; Zhang, X.; Yang, J.; Hwang, B. J.; Dai, H. *Adv. Mater.* **2016**, *28* (41), 9218-9222.
- (5) Wang, D.-Y.; Wei, C.-Y.; Lin, M.-C.; Pan, C.-J.; Chou, H.-L.; Dai, H.; et al. *Nat. Commun.* **2017**, *8*, 14283.
- (6) Angell, M.; Pan, C.-J.; Rong, Y.; Yuan, C.; Lin, M.-C.; Hwang, B.-J.; Dai, H. *Proc. Natl. Acad. Sci.* **2017**, *114* (5), 834-839.
- (7) Jayaprakash, N.; Das, S. K.; Archer, L. *Chem. Commun.* **2011**, *47* (47), 12610-12612.
- (8) Brown, G. M.; Paranthaman, M. P.; Dai, S.; Dudney, N. J.; Manthiram, A.; McIntrye, T. J.; Sun, X. G. (2012), U.S. Patent No. 20,120,082,904.
- (9) (a) Wang, H.; Gu, S.; Bai, Y.; Chen, S.; Zhu, N.; Wu, C.; Wu, F.; Palomares, V.; Serras, P.; Villaluenga, I.; Hueso, K.; Carretero-Gonzalez J. *J. Matter. Chem. A* **2015**, *3* (45), 22677-22686. (b) Chiku, M.; Takeda, H.; Matsumura, S.; Higuchi, E.; Inoue, H. *ACS Appl. Mater. Interfaces* **2015**, *7* (44), 24385-24389.
- (10) Lombardo, L.; Brutti, S.; Navarra, M. A.; Panero, S.; Reale, P. *J. Power Sources* **2013**, *227*, 8-14.
- (11) Sakaebe, H.; Matsumoto, H. *Electrochim. Commun.* **2003**, *5* (7), 594-598.
- (12) Holzapfel, M.; Jost, C.; Prodi-Schwab, A.; Krumeich, F.; Würsig, A.; Buqa, H.; Novák, P. *Carbon* **2005**, *43* (7), 1488-1498.
- (13) Elia, G.A.; Ulissi, U.; Mueller, F.; Reiter, J.; Tsiorvas, N.; Sun, Y. K.; Scrosati, B.; Passerini, S.; Hassoun, J. *Chem. Eur. J.* **2016**, *22*, 6808-6814.
- (14) Carlin, R. T.; De Long, H. C.; Fuller, J.; Trulove, P. C. *Electrochim. Soc.* **1994**, *141* (7), L73-L76.
- (15) Rothermel, S.; Meister, P.; Schmuelling, G.; Fromm, O.; Meyer, H.-W.; Nowak, S.; Winter, M.; Placke, T. *Energy Environ. Sci.* **2014**, *7*, 3412-3423.
- (16) Fan, J.; Zhang, Z.; Liu, Y.; Wang, A.; Li, L.; Yuan, W. *Chem. Commun.* **2017**, *53* (51), 6891-6894.
- (17) (a) Wilkes, J. S.; Zaworotko, M. *J. Chem. Soc., Chem. Commun.* **1992**, 965-967. (b) Larsen, A. S.; Holbrey, J. D.; Tham, F. S.; Reed, C. A. *J. Am. Chem. Soc.* **2000**, *122* (30), 7264-7272.
- (18) Yoneda, Y.; Ebner, G.; Takano, T.; Nakatsubo, F.; Potthast, A.; Rosenau, T. *J. Label. Comprpd. Radiopharm.* **2009**, *52* (6), 223-226.
- (19) Reed, L. D.; Menke, E. J. *Electrochim. Soc.* **2013**, *160* (6), A915-A917.

Electrode Sheets

For a complete list of available materials, visit SigmaAldrich.com/lib.

Name	Composition	Purity (%)	Nominal Voltage (V)	Capacity (minimum)	Capacity (nominal)	Cat. No.
Lithium manganese nickel oxide, LMNO	$\text{Li}_2\text{Mn}_3\text{NiO}_8$	≥98	4.7 (Li/Li ⁺)	115 mAh/g	125 mAh/g	765198-1EA
Lithium manganese oxide, LMO	LiMn_2O_4	≥98	4.7 (Li/Li ⁺)	110 mAh/g	120 mAh/g	765201-1EA
Lithium nickel cobalt aluminium oxide, NCA	$\text{LiNi}_{0.8}\text{Co}_{0.15}\text{Al}_{0.05}\text{O}_2$	≥98	3.7 (Li/Li ⁺)	150 mAh/g	180 mAh/g	765171-1EA
Lithium nickel manganese cobalt oxide, NMC	$\text{LiNi}_{0.33}\text{Mn}_{0.33}\text{Co}_{0.33}\text{O}_2$	-	3.5 (Li/Li ⁺)	210 mAh/g	-	765163-1EA
Lithium titanate, LTO	$\text{Li}_4\text{Ti}_5\text{O}_{12}$	≥98	1.5 (Li/Li ⁺)	160 mAh/g	150 mAh/g	765155-1EA

Cathode Materials

For a complete list of available materials, visit SigmaAldrich.com/lib.

Name	Composition	Purity (%)	Size	Cat. No.
Cobalt monoantimonide	CoSb	99.9 trace metals basis	-80 mesh	746320-5G
Lithium cobalt(III) oxide	LiCoO_2	powder, 99.8 trace metals basis	-	442704-100G-A
Lithium cobalt phosphate, LCP	LiCoPO_4	powder, ≥99 (trace metals analysis)	-	725145-25G
Lithium iron(III) oxide	LiFeO_2	powder, 95	particle size <1 µm	442712-100G-A
Lithium iron(II) phosphate, LFP	LiFePO_4	powder, >97 (XRF)	particle size <5 µm (BET)	759546-5G
Lithium manganese dioxide	LiMnO_2	powder, >99 trace metals basis	particle size <1 µm	725137-25G
Lithium manganese nickel oxide, LMNO	$\text{Li}_2\text{Mn}_3\text{NiO}_8$	powder, >99	particle size <0.5 µm (BET)	725110-25G
Lithium manganese oxide, LMO	LiMn_2O_4	powder, >99	particle size <0.5 µm (BET)	725129-25G
Lithium molybdate	Li_2MoO_4	powder or crystals, 99.9 trace metals basis	-	400904-250G
Lithium manganese(III,IV) oxide, LMO	LiMn_2O_4	-	particle size <5 µm	482277-25G
Lithium nickel cobalt aluminium oxide, NCA	$\text{LiNi}_{0.8}\text{Co}_{0.15}\text{Al}_{0.05}\text{O}_2$	powder, >98	particle size <0.5 µm	760994-10G
Lithium nickel cobalt oxide, LNCO	$\text{LiNi}_{0.8}\text{Co}_{0.2}\text{O}_2$	powder, >98	particle size <0.5 µm	760986-10G
Lithium nickel dioxide, LNO	LiNiO_2	powder, ≥98 trace metals basis	particle size <3 µm (BET)	757365-10G
Lithium nickel manganese cobalt oxide, NMC	$\text{LiNi}_{0.33}\text{Mn}_{0.33}\text{Co}_{0.33}\text{O}_2$	powder, >98	particle size <0.5 µm	761001-10G

Anode Materials

For a complete list of available materials, visit SigmaAldrich.com/lib.

Name	Purity (%)	Description	Form	Cat. No.
Lithium	99, metals basis	particle size 4-10 mesh	granular	444456-10G 444456-50G
	99.9 trace metals basis	thickness × W 1.5 × 100 mm	ribbon	266000-25G 266000-100G
	99.9 trace metals basis	thickness × W 0.75 × 45 mm	ribbon	265993-25G 265993-100G
	99.9 trace metals basis	thickness × W 0.75 × 19 mm	ribbon	320080-25G 320080-100G
	99.9 trace metals basis	thickness × W 0.38 × 23 mm	ribbon	265985-25G 265985-100G
	≥98	diam. 3.2 mm	wire	278327-25G 278327-100G
Lithium-aluminum alloy	-	-	powder	426490-25G
Lithium titanate, LTO	-	-80 mesh	powder	400939-100G
Lithium titanate, spinel, LTO nanopowder	>99	particle size <200 nm (BET)	nano powder	702277-25G
Tin(IV) oxide	-	avg. part. size ≤100 nm	nano powder	549657-5G 549657-25G

Electrolyte Solutions

For a complete list of available materials, visit SigmaAldrich.com/lib.

Battery Grade: H₂O <15 ppm; HF <500 ppm; APHA <50

Name	Specifications	Cat. No.
1.0 M LiPF ₆ in EC/DMC=50/50 (v/v)	in ethylene carbonate and dimethyl carbonate	746711-100ML 746711-500ML
1.0 M LiPF ₆ in EC/EMC=50/50 (v/v)	in ethylene carbonate and ethyl methyl carbonate	746738-100ML 746738-500ML
1.0 M LiPF ₆ in EC/DEC=50/50 (v/v)	in ethylene carbonate and diethyl carbonate	746746-100ML
1.0 M LiPF ₆ in DMC	in dimethyl carbonate	746754-100ML
1.0 M LiPF ₆ in EMC	in ethyl methyl carbonate	746762-100ML
1.0 M LiPF ₆ in DEC	in diethyl carbonate	746770-100ML
1.0 M LiPF ₆ in PC	in propylene carbonate	746789-100ML 746789-500ML
2.0 M LiPF ₆ EC/DEC=50/50(v/v)	in ethylene carbonate and diethyl carbonate	809349-100ML
2.0 M LiPF ₆ in EC/DMC=50/50(v/v)	in ethylene carbonate and dimethyl carbonate	809357-100ML 809357-500ML
2.0 M LiPF ₆ EMC	in ethylmethyl carbonate	809403-100ML 809403-500ML
2.0 M LiPF ₆ DMC	in dimethyl carbonate	809411-100ML 809411-500ML
2.0 M LiPF ₆ PC	in propylene carbonate	809470-100ML 809470-500ML
2.0 M LiPF ₆ EC/EMC=50/50(v/v)	in ethylene carbonate and ethylmethyl carbonate	809365-100ML 809365-500ML
2.0 M LiPF ₆ DEC	in diethyl carbonate	809543-100ML 809543-500ML

Ionic Liquids

For a complete list of available materials, visit SigmaAldrich.com/lib.

Name	Structure	Purity (%)	Cat. No.
1-Butyl-2,3-dimethylimidazolium bis(trifluoromethylsulfonyl)imide		≥99	900804-25G
1-Butyl-3-methylimidazolium bis(trifluoromethylsulfonyl)imide		≥99	900802-25G
1-Butyl-3-methylimidazolium chloride		≥99	900856-25G

Name	Structure	Purity (%)	Cat. No.
1-Butyl-1-methylpiperidinium bis(trifluoromethylsulfonyl)imide		≥99	900807-25G
1-Butyl-1-methylpyrrolidinium bis(trifluoromethylsulfonyl)imide		>99	900873-25G
1-Ethyl-3-methylimidazolium acetate		≥98	900787-25G
1-Ethyl-3-methylimidazolium bis(trifluoromethylsulfonyl)imide		≥99	900801-25G
1-Ethyl-3-methylimidazolium chloride		>99	900771-25G
1-Ethyl-3-methylimidazolium hexafluorophosphate		≥99	900779-25G
1-Ethyl-3-methylimidazolium tetrafluoroborate		≥99	900772-25G
1-Ethyl-1-methylpyrrolidinium bis(trifluoromethylsulfonyl)imide		≥99	900813-25G
1-Ethyl-1-methylpyrrolidinium tetrafluoroborate		>99	900808-25G
1-Methyl-1-propylpiperidinium bis(trifluoromethylsulfonyl)imide		≥99	900806-25G
Tributylmethylammonium bis(trifluoromethylsulfonyl)imide		≥99	900857-25G

Electrolyte Materials

For a complete list of available materials, visit SigmaAldrich.com/lib.

Name	Composition	Purity (%)	Cat. No.
Lithium difluoro(oxalato)borate	$\text{LiBF}_2(\text{C}_2\text{O}_4)$	-	774138-25G
Lithium hexafluoroarsenate(V)	LiAsF_6	98	308315-10G
Lithium phosphate monobasic	LiH_2PO_4	99	442682-500G-A
Lithium hexafluorophosphate	LiPF_6	≥99.99 trace metals basis	450227-5G 450227-25G 450227-250G
Lithium tetrafluoroborate	LiBF_4	99.99 trace metals basis	451622-5G 451622-25G
Lithium trifluoromethanesulfonate	$\text{CF}_3\text{SO}_3\text{Li}$	99.995 trace metals basis	481548-5G 481548-25G
Lithium perchlorate	LiClO_4	99.99 trace metals basis	634565-10G 634565-100G
Lithium bis(oxalato)borate	$\text{LiB}(\text{C}_2\text{O}_4)_2$	-	757136-25G

Solvents and Additives

For a complete list of available materials, visit SigmaAldrich.com/lib.

Name	Structure	Purity (%)	Cat. No.
Acetonitrile, electronic grade	CH ₃ CN	99.999 trace metals basis	733466-1L 733466-4L
Adiponitrile, H ₂ O <100 ppm acid <200 ppm	N≡C—CH ₂ —CH ₂ —CH ₂ —CH ₂ —C≡N	>99	900020-25G 900020-500G
Allyl methyl sulfone		96	718203-5G
tert-Amylbenzene		≥99	900001-1EA 900001-25G 900001-500G
Bis(trifluoromethane)sulfonimide		-	449504-10G 449504-50G
1-Butyl-3-methylimidazolium thiocyanate, for energy applications		≥95	724408-5G
1,4-Di- <i>tert</i> -butyl-2,5-bis (2-methoxyethoxy) benzene, anhydrous		99.5	900797-5G 900797-25G
Diethyl carbonate, anhydrous		≥99	517135-100ML 517135-1L
Diethyl carbonate, H ₂ O <10 ppm acid <10 ppm		≥99	900018-25G 900018-500G
Diethyl sulfite		98	774278-25G
Dimethyl carbonate, H ₂ O <10 ppm acid <10 ppm		≥99.9	809942-25G
1,2-Dimethyl-3-propylimidazolium bis(trifluoromethylsulfonyl)imide, for energy applications		99.9 trace metals basis	724416-1G
2,2-Dimethyl-3,6,9,12-tetraoxa-2-silatridecane		≥98	900871-5G 900871-25G
Ethylene carbonate, H ₂ O <10 ppm acid <10 ppm		≥99	809950-25G 809950-500G
Ethylene sulfite		≥99.0	774251-25G
Ethyl methyl carbonate		99	754935-50ML
Ethyl methyl carbonate, H ₂ O <10ppm acid <10 ppm		99.9	809934-25G 809934-500G
1-Ethyl-3-methylimidazolium tetrachloroaluminate, for energy applications		99.9 trace metals basis	724424-5G
Ethyl methyl sulfone, for energy applications		97	709980-5G
Fluoroethylene carbonate		99	757349-25G
3-(Methylsulfonyl)-1-propyne		95	718319-5G
Methyl-trioctylammonium bis(trifluoromethylsulfonyl)imide, for energy applications		99.9 trace metals basis	724432-1G

Name	Structure	Purity (%)	Cat. No.
Phenylcyclohexane, H ₂ O <100 ppm acid < 200 ppm		≥99	810002-25G 810002-500G
1,3-Propanesultone, H ₂ O <100 ppm acid <200 ppm		≥99	809985-25G 809985-500G
Propylene carbonate, H ₂ O <10 ppm acid <10 ppm		≥99	809969-25G 809969-500G
1,2-Propyleneglycol sulfite		≥98	774456-10G
1,3-Propylene sulfite		99	774243-25G
2-Propynyl methanesulfonate, H ₂ O <100 ppm acid <200 ppm		≥99.5	809993-25G 809993-500G
2,2,4,4-Tetramethyl-3,8,11,14,17-pentaoxa-2,4-disilaoctadecane		99	900763-5G 900763-25G
Vinylene carbonate		99	757144-25G
Vinylene carbonate, H ₂ O <100 ppm acid <200 ppm		99.5	809977-25G 809977-500G

subscribe today

Don't miss another
topically focused technical review.

It's **free** to sign up for a print or digital subscription
of *Material Matters*™.

- Advances in cutting-edge materials
- Technical reviews on emerging technology from leading scientists
- Peer-recommended materials with application notes
- Product and service recommendations

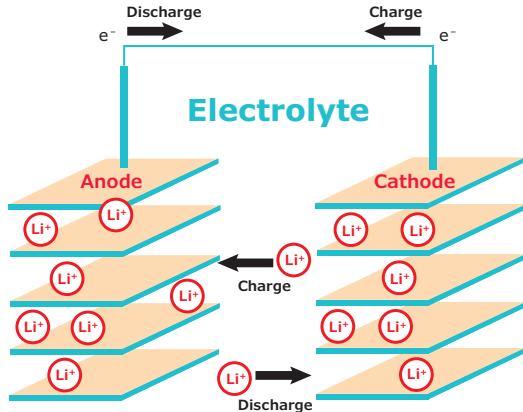


To view the library of past issues
or to subscribe, visit
SigmaAldrich.com/materialmatters.

Product Highlight

Make Your Own Lithium-Ion Batteries

Applications of lithium-ion batteries (LIBs) extend from modern electronics to automobiles. Order ready-to-use electrolyte solutions and electrode sheets in battery grade to fabricate your LIB.



Electrolyte Solutions

$H_2O < 15 \text{ ppm}$, $HF < 50 \text{ ppm}$, $APHA < 50$

Name	Specifications	Cat. No.
2.0 M LiPF6 in EC/DMC=50/50 (v/v)	in ethylene carbonate and dimethyl carbonate	809357
2.0 M LiPF6 in EC/EMC=50/50 (v/v)	in ethylene carbonate and ethyl methyl carbonate	809365
2.0 M LiPF6 in EC/DEC=50/50 (v/v)	in ethylene carbonate and diethyl carbonate	809349
2.0 M LiPF6 in DMC	in dimethyl carbonate	809411
2.0 M LiPF6 in EMC	in ethyl methyl carbonate	809403
2.0 M LiPF6 in DEC	in diethyl carbonate	809543
2.0 M LiPF6 in PC	in propylene carbonate	809470

Electrode Sheets

Aluminum substrate, size 5 in. \times 10 in.

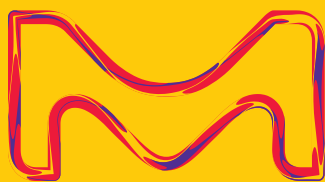
Name	Specifications	Composition	Cat. No.
Lithium nickel manganese cobalt oxide	loading >80%, thickness 25–50 μm	$\text{LiNi}_{0.33}\text{Mn}_{0.33}\text{Co}_{0.33}\text{O}_2$	765163
Lithium nickel cobalt aluminum oxide	loading >80%, thickness 12–25 μm	$\text{LiNi}_{0.8}\text{Co}_{0.15}\text{Al}_{0.05}\text{O}_2$	765171
Lithium manganese nickel oxide	loading >80%, thickness 25–50 μm	$\text{Li}_2\text{Mn}_3\text{NiO}_8$	765198
Lithium manganese oxide	loading >80%, thickness 25–40 μm	LiMn_2O_4	765201
Lithium titanate spinel	loading >80%, thickness 25–50 μm	$\text{Li}_4\text{Ti}_5\text{O}_{12}$	765155

To find out more, visit
SigmaAldrich.com/LIB.

Merck KGaA
Frankfurter Strasse 250
64293 Darmstadt, Germany

Sigma-Aldrich®

Lab Materials & Supplies



THE MASTERS OF MATERIALS

Expertise at the nanoscale

SigmaAldrich.com/nanomaterials

The life science business of Merck operates as
MilliporeSigma in the U.S. and Canada.

Merck and the vibrant M are trademarks of Merck KGaA, Darmstadt, Germany or its affiliates. All other trademarks are the property of their respective owners. Detailed information on trademarks is available via publicly accessible resources.
Copyright © 2018 Merck KGaA, Darmstadt, Germany and/or its affiliates. All Rights Reserved.
Lit. No. MK_BR1533EN 2018 - 08735 04/2018

MERCK

